The definitive publisher version is available online at https://doi.org/10.1016/j.jclepro.2022.130629

Application of electrolytic manganese residues in cement products through pozzolanic activity motivation and calcination

Fan Wang[1], Guangcheng Long[*1], Min Bai[1], Jilin Wang[1], John L. Zhou[12], Xiang Zhou[1]

[1] School of Civil Engineering, Central South University, 68 South Shaoshan Road, Changsha, Hunan 410075, China

[2] Centre for Green Technology, School of Civil and Environmental Engineering, University of Technology Sydney, Sydney, NSW 2007, Australia

Fan Wang, Email: wn2020@csu.edu.cn

(Corresponding author) Guangcheng Long, Email: longguangcheng@csu.edu.cn

Min Bai, Email: minbai2021@163.com

Jilin Wang, Email: 193571717@qq.com

John L. Zhou, Email: junliang.zhou@uts.edu.au

Xiang Zhou, Email: xiangzhou@csu.edu.cn

[*] Corresponding author: longguangcheng@csu.edu.cn (G. Long)

Highlights

- EMR calcined at 800 ℃ has the optimum strength activity index of 84.79 at 28-d.
- Pozzolan activity of EMR is boosted in β-$CaSO_4 \cdot 0.5H_2O$ and weakened in Mn_3O_4 and $MnFe_2O_4$.
- Presence of gypsum in EMR retards the cement hydration and forms ettringite.
- Mn^{2+} and NH_4^+-N below national standards at calcination above 800 °C.

Graphical abstract

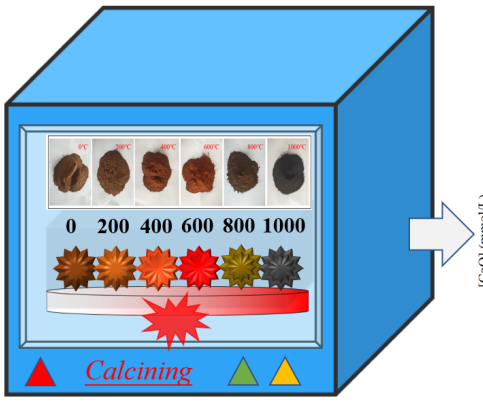

Samples	3 days		28 days		90 days	
	Mn	NH_3-N	Mn	NH_3-N	Mn	NH_3-N
M-CEMR$^{HSI}_{800}$	2.10	1.00	1.10	0.50	1.00	ND
GB5085.3-1996	5.00	25.00	5.00	25.00	5.00	25.00

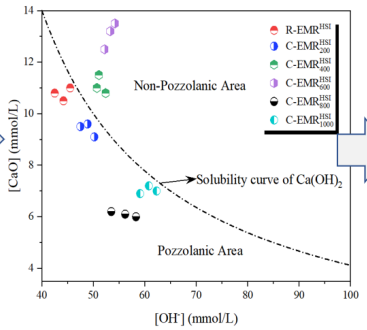

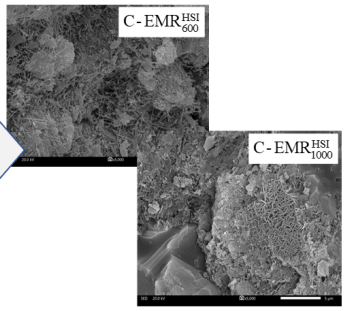

Hazard-free treatment **Pozzolanic activity** **Cement-based utilization**

Abstract

Degradation in grade of manganese ore aggravates the complexity of electrolytic manganese residue (EMR). Calcination is one of the most practical pretreatment methods to improve EMR activity and dispose the hazardous elements. In this paper, the evolution of mineral phase, pozzolanic activity, pore structure and harmful components induced by calcining EMR was investigated. The results show that EMR calcined at 800 ℃ has the strength activity index (SAI) of 84.79 at 28 d, which is attributed to the decomposition of dihydrate gypsum and the formation of activated calcium, silicon and aluminum oxide. The formation of β-type hemihydrate gypsum increases the pozzolan activity, while the latter is limited by the formation of stable Mn-spinel (Mn_3O_4) and Mn-hercynite ($MnFe_2O_4$). In the EMR-doped mortar matrix, the production of a large amount of ettringite due to the existence of gypsum, as well as common C-S-H, portlandite and AFm, which strongly verify the pozzolanic activity of EMR. Leaching results show that Mn^{2+} and NH_4^+-N could not be eliminated completely at low temperature (< 600 ℃), but could be completely stabilized in the alkaline environment provided by the cement. The Mn^{2+} and NH_4^+-N levels in mortar are fully below the regulatory standards when calcinated above 800°C. All heavy metals are fixed in the cement and calcination process, ensuring the cleaner utilization of EMR in building materials.

Keywords: Calcination; Electrolytic manganese residue; Pozzolanic activity; Hazard-free treatment; Mortar stabilization.

1 Introduction

Electrolytic manganese is an essential metallurgical and raw material that is widely used in the production of batteries, steels, alloys, building and other industries (Duan et al., 2010; Duan et al, 2011). China is currently the top producer of electrolytic manganese with an annual production of over 1.5 million tons, accounting for approximately 98% of global output (Xu et al., 2014; Zhou et al., 2014; Shu et al., 2016; Li et al., 2016; Han and Wu, 2019; He et al., 2021a). Electrolytic manganese residue (EMR) is a hazardous solid waste produced as a byproduct after the traditional sulfuric acid leaching of manganese carbonate ore and ammonia neutralization (Wang et al., 2019; Wang et al., 2020; He et al., 2021b).

Currently, fabricating one ton of electrolytic manganese metal could produce about 10-14 tons of EMR (Shu et al., 2016; Wang et al., 2019; Shu et al., 2019a). It is noted that this condition has worsened rapidly due to the continued depletion of global raw ore (Duan et al., 2010; He et al., 2021c). The stacked EMR with a high-water content of 25-35 wt.% and a low-pH range of 5.0-6.5, and the particle size of 20-500 μm, which changes with the disposed time and formation process (Han and Wu, 2019). In addition, EMR contains not only a large number of soluble salts, such as ammonium sulfate and manganese sulfate, but also heavy metal elements including Ni, Co, Cd, Pb, Cu, etc (He et al., 2021c; Shu et al., 2020b; Ma et al., 2020; Wang et al., 2020). The discharged EMR is significantly difficult to be disposed because of its diversity, fineness, and viscosity (Duan et al, 2011; Zhang et al., 2020b; He et al., 2021c). Therefore, electrolytic manganese smelters dispose of their EMR in designated waste landfill sites without any effective pretreatment (Duan et al, 2011; Wang et al., 2020; He et al., 2021c). It is inevitably that a large amount of landfill sites and the surrounding soil and groundwater may be seriously polluted (Han and Wu, 2019). In addition, as the continuous stockpiled EMR is exposed to the open-air environment, inevitably soluble metal sulfate and

ammonium sulfate decomposition occurs, resulting in harmful gases emissions (e.g., SO_2 and NH_3) (Wang et al., 2016; Sun et al., 2020; Li et al., 2016). Therefore, the stored EMR has significantly hindered the development of the manganese industry and posed a serious threat to the ecological environment (He et al., 2021c; Lan et al., 2021a). These environmental problems caused by EMR have currently attracted widespread concern in society, and urgently need solutions.

At present, the existing landfills can dispose of EMR in bulk, but the subsequent secondary pollution does not solve the problem completely (He et al., 2021b). Utilization of water leaching, acid leaching, and bioleaching treatments can effectively extract the valuable substances from EMR, but the disposal of secondary contamination induced by the leachate is still an inevitable hidden trouble (Duan et al., 2010; Bal et al., 2018; Han et al., 2018; Lan et al., 2021b; He et al., 2021c, 2021d). The stabilization/solidification technology can be used to immobilize hazardous components in EMR, and the disposed EMR is directly applied in building materials (Chen et al., 2020; Han et al., 2020; He et al., 2021d; Lan et al., 2021a). The resource utilization of EMR has been realized to a certain extent. However, its application in engineering practice is severely limited by high immobilization charges, uncontrollable hardening efficacy and potential re-leaching risks. However, calcination is widely employed in the solid waste pretreatment procedure as one of the most environmentally friendly disposal methods (Xu et al., 2011; Li et al., 2018; Ma et al., 2020; He et al., 2021d). Calcination has many benefits with respect to other methods, as the hazardous substances in EMR are cleaned during the calcination process. Although the calcination causes energy consumption, a small minority of the heat released by calcination can be used for power generation, while the collected gases are made into chemical reagents or recycled reserves (Shu et al., 2020; Zhang et al., 2020; Zhou, 2021). More importantly, compared with untreated EMR, calcined EMR tends to have high reactivity and is more suitable for the production of building materials, such as bricks, ceramics, lightweight aggregates and

supplemental cementitious materials (Yang et al., 2014; Wu et al., 2016; Wang et al., 2019; Zhang et al., 2019a, 2019b; Xu et al., 2019; Zhang et al., 2020a; Han et al., 2020; Zhou et al., 2021). Meanwhile, the quasi-sulfoaluminate cement with high compressive strength was manufactured by EMR (close to 40%) combined with limestone and kaolinite calcined at 1200°C (Hou et al., 2012). Numerous studies have explored the recycling alternatives of EMR in building materials, especially the potential use as a substitute for cement in mortar and concrete (Hou et al., 2012; Lan et al., 2021d). The high specific surface area and gypsum phase of EMR significantly increase the unit water demand, and gypsum accelerates cement hydration as it promotes ettringite production and provides more nucleation space for precipitation of hydration products (Zhou et al., 2021). It is expected that EMR can replace part of the cement and obtain acceptable mechanical strength and significant economic benefits due to the higher pozzolanic activity (Ma et al., 2020; Zhou et al., 2021). Calcination or incineration temperature has a significant effect on the reactivity of EMR. Recent studies have confirmed that the potential pozzolanic activity of EMR can be activated by thermal treatment, either by incineration alone or in combination with other solid wastes (Wang et al., 2013; Liu et al., 2017; Li et al., 2018; Li et al., 2020; Xie et al., 2021).

Notwithstanding the satisfying results for EMR-combined matrix, more research is needed regarding the effect of heat treatment on the physicochemical properties and pozzolan activity of EMR. Therefore, this paper aims to identify and quantify the changes in the physicochemical properties and pozzolanic activity of EMR disposed by different calcination temperatures. The evolution of physicochemical characteristics and mineral phase of the undisturbed and calcined EMR was characterized. Then, their pozzolan activity was analyzed in terms of the mortar strength activity index, Frattini test and calcium hydroxide consumption. The effects of EMR at different calcination temperatures on cement hydration, product phase formation and the microscopic pore structure of the

cementitious matrix were investigated. The leaching test was used to determine the leaching content of harmful components of EMR and the EMR-blended matrix with different calcination temperatures.

2 Material and methods

2.1 Raw materials

The EMR used was obtained from an electrolytic manganese smelter from Xiangtan Electrochemical Group. It is noted that the raw EMR is yellow mud-like material different from the common black (**Fig.1a**), which is due to the pyrite and soft manganese ore are introduced to two ore one-step process. Prior to test, the in-situ EMR was first dried at 75 ℃ for 72 hours, and then crushed and ground until it passed through a 150 meshes sieve with a specific surface area of 4.01 m^2/g (measured by nitrogen adsorption BET method). The basic physical characteristics of EMR according to ASTM standard are shown in **Table 1**.

The microstructure of EMR was described using scanning electron microscopy (SEM) (**Fig. 1b**). The results showed the grinded EMR particles with different sizes and morphologies, in which the smaller particles tend to cluster around the larger particles. The particle size distribution of EMR was detected with a particle size analyzer, as shown in **Fig. 2**. The chemical compositions of EMR and ordinary Portland cement (OPC) are shown in **Table 2**. As can be seen, the EMR has a large loss on ignition (LOI) of 18.24 % due to its high-water content. In addition to that, the raw EMR has a superior sulfate and iron, so the raw EMR is labeled R-EMR^{HSI}. Besides, the estimated Bogue potential phase composition of tested PC is shown in **Table 3**.

Table 1. Basic physical parameter of EMR

Feature	Water content (%)	Density ($g \cdot cm^{-3}$)	Stacking density ($g \cdot cm^{-3}$)	Mass fraction of water-soluble substance (%)	pH
Value	31.2±2	2.8±0.2	0.9±0.1	15.5±2	6.2±0.2

Table 2. The chemical compositions of EMR and ordinary Portland cement

Sample	SiO_2 (%)	CaO (%)	Fe_2O_3 (%)	Al_2O_3 (%)	MgO (%)	SO_3 (%)	MnO (%)	Cr_2O_3 (%)	LOI (%)
EMR	34.67	5.58	21.21	9.01	0.61	20.53	3.94	0.03	19.6
OPC	20.08	63.41	3.01	5.29	2.06	2.17	N. D	1.62	3.6

Note: N. D stands for not detected.

Table 3. Potential phase composition of tested OPC

Clinker	C_3S	C_2S	C_3A	C_4AF
Mass fraction (%)	54.4	22.6	6.9	10.1

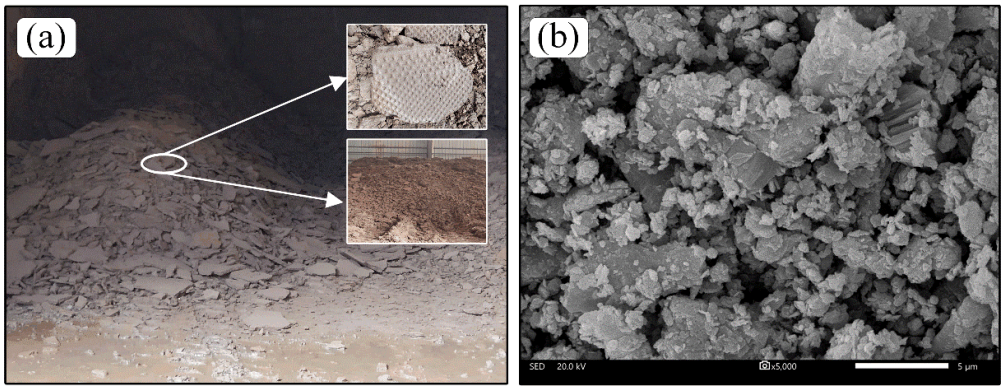

Fig. 1. The R-EMR^{HSI} stockpiles produced by the two ore one-step process (a) the storage field of the R-EMR^{HSI} (b) the microstructure of EMR by SEM.

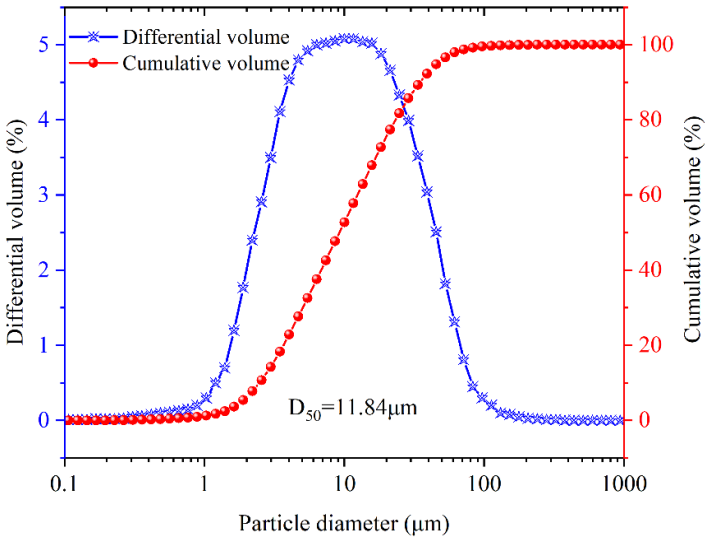

Fig. 2. The specific particle size distribution of R-EMR^{HSI} by BET method.

2.2 Different calcining temperatures

The calcined high-sulfur and iron-based EMR (C-EMR^{HSI}) was prepared at the desired calcining temperature in a muffle furnace. Calcining was conducted with a controlled airflow, where any flue-gas generated was collected and treated by a recovery device (**Fig. S1**). Five calcination temperatures (200 ℃, 400 ℃, 600 ℃, 800 ℃, 1000 ℃) were set and compared with the R-EMR^{HSI} to investigate the evolution of mineral phases and the fluctuation of pozzolanic activity. To promote the high-quality calcination, R-EMR^{HSI} was calcined for lasting 2 hours after increasing the temperature to the setting value at the heating rate of 5 ℃/min. After calcination, the C-EMR^{HSI} was rapidly collected from the muffle furnace, and then promptly cooled in the air. The label "C_{200}-EMR^{HSI}" means that the EMR^{HSI} calcined at 200 ℃ was used to follow-on operational test and evaluation, and so does the other "EMR-temperature" labels.

2.3 Characterization methods

The chemical compositions of R-EMR^{HSI} and C-EMR^{HSI} were determined using the X-ray

fluorescence (XRF, Bruker S4 Pioneer spectrometer). The mineralogical compositions of the R-EMR^{HSI} and C-EMR^{HSI} were identified using an X-ray diffractometer (XRD, Bruker D8 Advance diffractometer) employing Cukα radiation (λ = 0.154 nm, 40 kV, 50 mA) over scanning range 2θ = 5–80° with step width 2°/min^{-1}. The results of mineral phases were quantified by XRD-Rietveld analysis (Crumbie et al., 2006). The transition of mineral phases at various elevated temperatures was characterized by simultaneous thermal analyzer (TG-DTG, 50-1200 ℃, 10 ℃/min). The morphology of R-EMR^{HSI} and C-EMR^{HSI} was observed by a scanning electron microscope (SEM, JSM-6490LV, 20.0 kV with different magnification times). The particle size distribution and the specific surface area of R-EMR^{HSI} and C-EMR^{HSI} were determined by laser particle size scanning analyzer (BT-9300S, Bettersize Instruments Ltd., CN) and the Brunauer-Emmett-Teller (BET)-N_2 adsorption method, respectively. The density and water absorption of R-EMR^{HSI} and C-EMR^{HSI} was determined using a pycnometer with kerosene as a medium and tea-bag method, respectively.

2.4 Evaluation of calcined EMR pozzolanic activity

The pozzolanic activity of C-EMR^{HSI} samples was analyzed by strength activity index (SAI) test, Frattini test and saturated lime (SL) consumption test.

SAI test

The SAI results were used to characterize the pozzolanic activity of supplementary cementitious materials (Liu et al., 2017; Pourkhorshidi et al., 2010; Tironi et al., 2013). The SAI was calculated as the ratio of the compressive strength of the blended mortar to that of the referred ordinary Portland cement at the same curing age, as shown in equation (1). The compressive strength of blended mortar at 3, 14, 28, 60 and 90 days was detected to characterize the pozzolanic activity of C-EMR^{HSI} at different temperatures based on the Chinese standard (GB/T 1596-2017). Compared with ASTM

C618-17A, the pozzolanic activity of C-EMR^{HSI} was amplified by replacing 20% pozzolanic and 80% cement with 30% pozzolanic and 70% cement mixed mortar. The compressive strength of blended cement was evaluated on mortar cubes (4 cm ×4 cm×4 cm) performed with fixed sand/ binder (1:3 by mass ratios) and water/ binder mass ratios (1:2). After the strength test, some fragments on the sample center were collected and then immersed in ethyl alcohol for 48 hours and then dried at 60 ℃ over 12 hours to eliminate the moisture.

$$SAI = \frac{CS_A}{CS_B} \quad (1)$$

where, CS_A is the compressive strength of the tested C-EMR^{HSI} sample (MPa) and CS_B is the compressive strength of the controlled mortar (MPa). In comparison with ASTM C618, the test sample has a positive pozzolanic activity as SAI greater than 0.75 after 7 and 28 days at 20% cement replacement. According to GB 2847-2005, the test specimen possesses a positive pozzolanic activity as the results of SAI greater than 0.65 after 28 days with 30% cement replacement.

Frattini test

Based on EN 196-5, the Frattini test involves chemical titration to determine the concentrations of dissolved [Ca^+] and [OH^-] in a solution with 30% pozzolanic and 70% cement. Thus, 14 g cement and 6 g C-EMR^{HSI} mixed with 100 mL deionized water for preparing test samples. The pozzolanic activity of the tested sample was qualified as the test result was lower than the concentration of $Ca(OH)_2$ in saturation concentration at the same alkalinity. The samples were sealed for 8 days in a cylindrical polyethylene container and then placed in water bath kettle at 40 ℃. The solution was filtered in vacuum and then cooled to ambient temperature upon test ages to detect. The filtrates were titrated with 0.1 mol/L HCl solution with methyl orange indicator and 0.015 mol/L EDTA solution to analyze [OH^-] and [Ca^{2+}], respectively. The comparative analysis was made with the solubility curve of $Ca(OH)_2$ at 40 ℃as the reference. The C-EMR^{HSI} was defined as active pozzolanic material when

$[Ca^{2+}]$ and $[OH^{-}]$ in solution were down the solubility isotherm.

SL consumption test

Considering the Frattini test only qualitatively determined the pozzolanic activity of C-EMR^{HSI}, the SL test was performed to further investigate the reacted yield and rate of C-EMR^{HSI} with $Ca(OH)_2$. Thus, a mixture consisting of C-EMR^{HSI}, $Ca(OH)_2$ and water was fabricated as a certain weight ratio of 1:1:2. Then, the samples were placed in the water bath at 40 ℃until the specified test ages. Samples were then filtered and titrated for $[OH^-]$ and $[Ca^{2+}]$ using the same procedure as the aforementioned Frattini test. Notably, the absolute amount of $Ca(OH)_2$ in the system is settled and the raised temperature guarantee rapid reaction with the pozzolan substance (Hardjito et al., 2012).

2.5 Leaching test

The leaching tests of R-EMR^{HSI} and C-EMR^{HSI} were conducted using the horizontal vibration extraction procedure (HJ/T 300-2007; HJ-557-2010; HJ 908-20). The fragmentized samples (5g each) were placed into a plastic bottle with a solid/ liquid mass ratio of 1:20 (100 mL), respectively. After vibrating for 8 hours at a frequency of $120min^{-1}$ and then sitting for 16 hours, all samples were filtered and stored for inductively coupled plasma optical emission spectrometry (ICP-OES) tests. Atomic absorption spectrophotometry inflame was used for determining the concentration of metal ions (HJ 484-2009). NH_4^+-N was measured via Nessler's reagent spectrophotometry method of HJ 535-2009 (Standards, 2009b) and GB/T 205-2000 (Standards, 2000).

3 Results and discussion

3.1 Physicochemical characteristics and mineral composition of R-EMR^{HSI}

The XRD diagram of dried EMR is given in **Fig. 3**. The mineral composition of dried EMR mainly

includes jarosite, dihydrate gypsum, quartz, kaolinite, hematite, limonite, muscovite, and other sulfate-soluble substances. On the one hand, these mineral phases are derived from the additional mineral phases of low-grade manganese ore. On the other hand, the hydrometallurgical process of sulfuric acid leaching combined with two ore one-step method (pyrite) accumulating a large amount of soluble sulfate. Compared with the previous EMR, the introduction of sulfuric iron ore caused a substantial increase in the concentration of the iron phase (He et al., 2021c). The manganese ore not only formed fine particle under the strong chemical reaction accompanied by sulfuric acid leaching, but also reconstructed into porous particle morphology (**Fig. 2**).

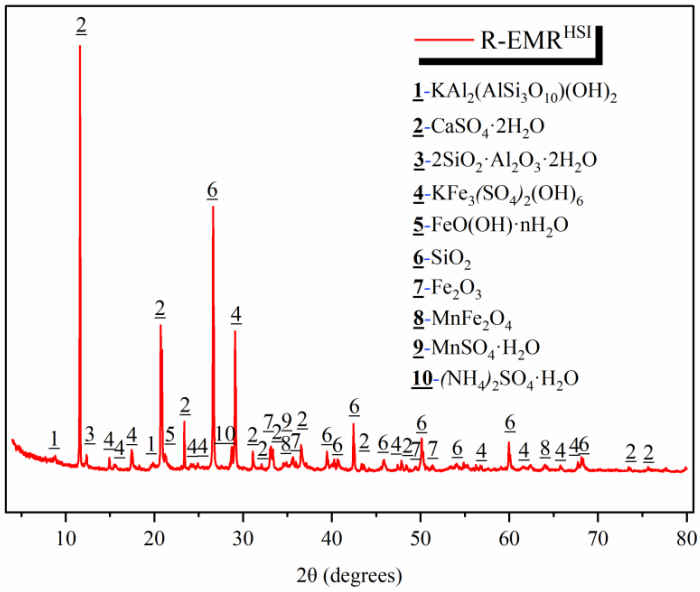

Fig. 3. The mineralogical compositions of the R-EMR^{HSI}.

It is clear from **Fig. 3** that crystal of quartz and gypsum phase has the most intact and sharp diffraction peaks at 26.6° and 11.6° (2θ), respectively. Other mineral phases have lower crystallinity, lower intensity peaks and dispersed peak shapes. From the production of EMR, it is inferred that jarosite and sulfates are the products of the acid leaching, and goethite and dihydrate gypsum are the products of neutralization and precipitation of the leaching substrate. However, the presence of clay-

like minerals, gypsum, and iron phase contributes to the high-water absorption of EMR. In addition, it has been noted that part of the water exists in the fine capillary dissolution pores of EMR, and the traditional drying temperature failed to evaporate this part of the moisture (He et al., 2021c). This may also be an essential contribution to the high viscosity and high-water absorption of EMR.

Fig. 4 shows that R-EMR^{HSI} has seven obvious endothermic peaks at 72, 145, 260, 500, 860, 946, and 1030 ℃. The total mass loss of R-EMR^{HSI} was 25.4 % within the range of 35~1050 ℃. Combined with the setting calcination temperature, the whole calcination can be divided into five stages.

The first stage (0-200 ℃): the two endothermic peaks at 72 ℃ and 145 ℃ in this stage are mainly caused by the desorption of adsorbed water in EMR particles and the removal of crystal water from the dihydrate gypsum, with a mass loss rate of 5.5 %.

The second stage (200-400 °C): further dehydration of the hemihydrate gypsum and the precipitation of ferric sulfate from heat-hydroxyl dehydration of jarosite, which is also the main reason for the heat absorption peaks at 260°C. In addition, the small troughs ranging from 260 to 400°C validate the continued progress. The overall mass loss at this stage reached 4.65 %. Thus, the dehydration effect occurs mainly in EMR below 400 ℃, where the total amount of adsorbed water, crystal water and hydroxyl dehydration are about 10.17 %.

The third stage (400-600 ℃): thermal decomposition of ferric sulfate to generate hematite and the escape of gases from the thermal decomposition of ammonium sulfate, and the overall mass loss in this stage about 6.23 %. The fourth stage (600-800 °C): the activation of alumino-silica minerals and the continuous decomposition of gypsum to increase active ingredients in the system. Although there is no obvious endothermic peak in this stage, the restructuration, recrystallization and amorphization of minerals are continuously proceeding, which is reflected in the subsequent activity test results and other results. It is precisely due to the small fluctuation of chemical composition that the overall mass

loss in this stage is 2.22 %.

The fifth stage (800-1000 °C): the muscovite mineral decomposed as the temperature increases, which was verified by the endothermic peak at 860 °C. The decomposition, recrystallization and amorphization of silica-alumina and sulfate minerals in EMR could be obtained from the two heat endothermic peaks at 946 and 1030 °C with the re-escalation of temperature. At this stage, the overall mass loss was 6.77 % due to the dehydration formation of type II anhydrite, sulfate decomposition and mineral activation.

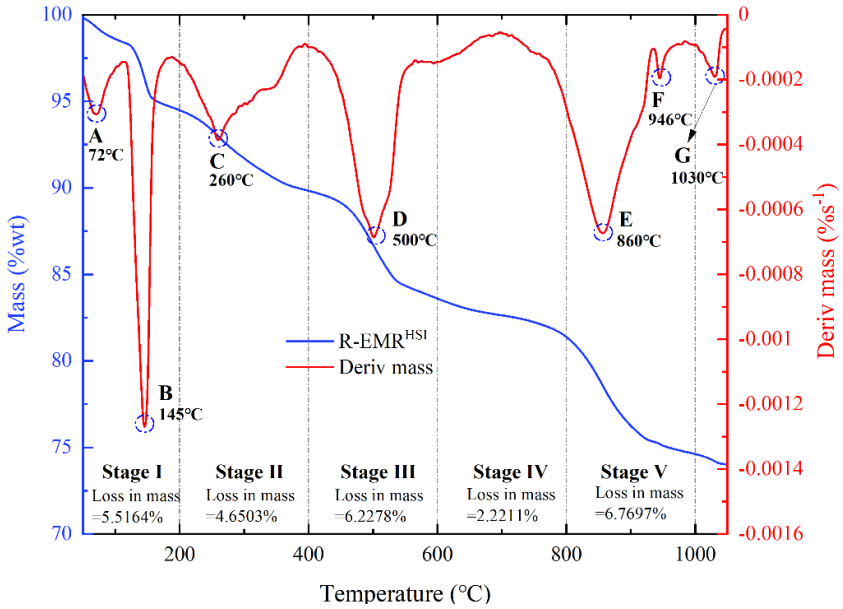

Fig. 4. The TG-DTG diagram of R-EMR^{HSI} (A, B stand for Mineral phase [$CaSO_4 \cdot 2H_2O$] dehydration; C represents mineral phase jarosite and $CaSO_4 \cdot 2H_2O$ dehydration and recrystallization; D shows Kaolinite mineral phase dehydrate activation and gas spillage; E expresses muscovite decomposition and mineral amorphization; F and G signify mineral decomposition, recrystallization and amorphization).

3.2 Physicochemical characteristics of C-EMR^{HSI}

The physicochemical properties of C-EMR^{HSI} via various calcination are exhibited in **Table 4**. The dominant oxides present in the C-EMR^{HSI} consisting of SiO_2, Al_2O_3, CaO, Fe_2O_3, SO_3 and MgO,

which express a close commonality with R-EMR^{HSI} (**Table 2**). However, the oxides proportions of C-EMR^{HSI} varied slightly under different calcination.

Table 4 depicts the main compositions of C-EMR^{HSI} kept basically stable under the calcination from 200 ℃ to 1000 ℃. It is noted that the sulfates are emitted in gaseous form (SO_3) as the increasing calcination temperature, which is attributed to the decomposition of sulfates in the EMR. The reduction of SO_3 can affect the variation in other oxides content.

More specifically, oxides such as SiO_2, Al_2O_3, CaO and Fe_2O_3 slightly increased with the increase of temperature. Other oxides have been tested without large fluctuations because of the low initial content. The loss on ignition (LOI) diminishes with increasing temperature and reaches up to 20.6%. In contrast to blast furnace slag, the production of EMR with a hydrometallurgical process results in a high LOI due to the absence of a precalcination at high temperatures (He et al., 2021a).

Table 4 also exhibits that the amorphous phase of C-EMR^{HSI} increased with the increasing calcining temperature. The maximum amorphous phase content was 42.18% at 800 ℃, which implied that the high temperature has a significantly activation on the pozzolanic activity of EMR and the optimal calcined temperature was of 800 ℃.

The density, particle size, BET surface area and water absorption of EMR after different calcination temperatures are shown in **Table 4**. The density of EMR increased with the increase of temperature. The particle size of calcined EMR increases continuously with density, while the opposite trend of surface area in the calcined EMR. The open pores of EMR particles are gradually closed with the increase of temperature. The unit water demand increases and then decreases with the increase of temperature, which is related to the transformation of the gypsum. In conclusion, the physicochemical properties of EMR are related to the mineral decomposition, reconstruction and crystal transformation.

Table 4. Physicochemical properties of C-EMR^{HSI}

Samples	C-EMR$^{HSI}_{200}$	C-EMR$^{HSI}_{400}$	C-EMR$^{HSI}_{600}$	C-EMR$^{HSI}_{800}$	C-EMR$^{HSI}_{1000}$
	Chemical analysis (% by mass)				
SiO_2	36.87	37.04	38.22	38.58	40.68
Al_2O_3	8.22	8.00	8.65	9.26	9.05
CaO	5.921	5.581	5.924	6.383	6.646
Fe_2O_3	21.8	21.86	22.33	23.31	24.92
SO_3	19.14	20.75	16.79	15.11	10.26
MgO	0.604	0.572	0.618	0.495	0.639
MnO	4.555	4.286	4.531	3.825	4.493
Na_2O	0.372	0.313	0.34	0.327	0.362
K_2O	1.41	1.32	1.44	1.48	1.57
TiO_2	0.252	0.238	0.249	0.265	0.281
P_2O_5	0.376	0.365	0.441	0.508	0.587
Amorphous phase	23.15	27.33	34.12	42.18	41.26
LOI	3.09	5.82	8.86	13.05	20.6
Property	Physical characteristics				
Density (g/cm^3)	2.915	2.924	2.931	2.937	2.945
D50 (μm)	12.83	13.51	13.92	14.25	14.94
BET surface area (m^2/g)	5.6327	3.8751	3.7114	2.8251	2.5671
Water absorption (g/g)	3.15	3.52	3.73	2.02	1.75

The apparent morphological of EMR at different calcination temperatures is exhibited in **Fig. 5**. As can be seen, the EMR gradually turns red in color at 0-400°C, mainly due to the increase in the goethite. In 400-600 ℃, EMR with light-red is deepened and converted to red because of hematite in large amount. When calcined to 800 ℃, there is a light sintering agglomeration and the EMR exhibits the dark-brown in color. At 1000 ℃, EMR transforms to black due to the presence of large amount of

Mn_3O_4 and iron oxide.

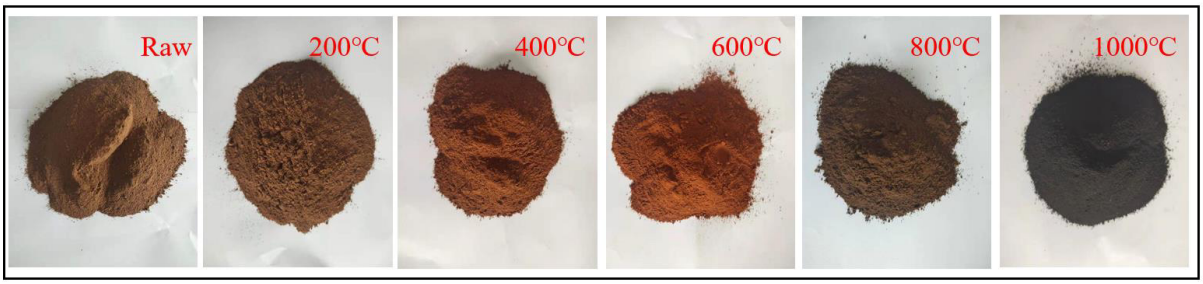

Fig. 5. Apparent morphology of the calcined EMR^{HSI}.

3.3 The transformation of the mineral composition of C-EMR^{HSI}

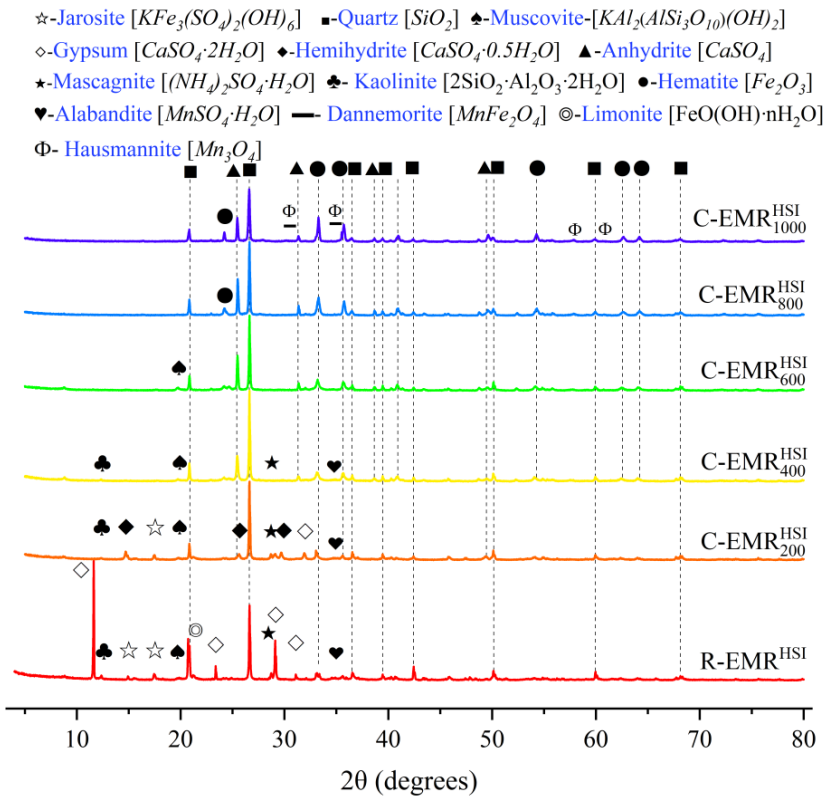

Fig. 6. The mineralogical compositions of the R-EMR^{HSI}.

The mineral compositions of C-EMR^{HSI} were identified by XRD results, as exhibited in **Fig.6**. And TG-DTG results of the calcined samples after experiencing the setting calcination temperature treatment are shown in **Fig. S2**.

3.3.1 Effect of calcination on gypsum phase

Combining the results in **Figs. 4**, **6** and **S2**, the stepwise dehydration of dihydrate gypsum to anhydrous gypsum phase as the rising calcination temperature. Specifically, when the calcination temperature below 200 °C, all crystalline water in the gypsum phase was firstly eliminated. When the calcination temperature exceeds 200 °C, the diffraction peaks disappear at 14.7 º, 25.7 º, 29.7 º and 31.9 º (2θ), indicating the continued dehydration of hemihydrate gypsum. With increasing the temperature below 800 °C, the diffraction peaks progressively strengthen at 25.5 º, 31.4 º and 40.9 º (2θ), showing the decomposition of anhydrous gypsum. Then, the anhydrous gypsum (Type Ⅱ) diffraction peak weakens gradually, which is associated with the inclusion of fused and glassy quartz phases in the EMR. The chemical formulae of the calcined reactions of the gypsum phase are shown in **equations (2)** to **(5)** and **Fig. S3**.

$$2CaSO_4 \cdot 2H_2O \xrightarrow{0\sim200℃} 2CaSO_4 \cdot 0.5H_2O(\beta) + 3H_2O \quad (2)$$

$$2CaSO_4 \cdot 0.5H_2O \xrightarrow{200\sim400℃} 2CaSO_4(\beta) + H_2O \quad (3)$$

$$2CaSO_4(\beta) \xrightarrow{400\sim800℃} CaSO_4(\text{II}) + CaO + SO_3 \quad (4)$$

$$2CaSO_4(\text{II}) \xrightarrow{>900℃} CaSO_4(\text{I}) + CaO + SO_3 \quad (5)$$

3.3.2 Effect of calcination on the iron phase

From Figs.**4, 6** and **S2**, it can be seen that the dehydration of limonite is intensified with the increase of calcination temperature, and recrystallizes to hematite (after 200°C). The newly-presented diffraction peaks about hematite at 33.2° and 35.6° (2θ) all verify this process. In addition, the jarosite is decomposed into sulfates and ferric oxide below 400°C. Then, further decomposition and recrystallization occurred to form hematite. The whole process is shown in **equation (6)**.

$$2KFe_3(SO_4)_2(OH)_6 \xrightarrow{0\sim400℃} 3Fe_2O_3 + K_2SO_4 + 3H_2SO_4 + 3H_2O \quad (6)$$

3.3.3 Effect of calcination on the silica-alumina phase

The diffraction peak intensity of quartz in EMR gradually weakens with the increase of calcination temperature. It speculates that the quartz phase increasingly becomes amorphous and fuse with other metal elements to form glassy silicate within this thermo-range. When the calcination temperature exceeds 500°C, kaolinite first undergoes dehydration and followed by gradually dihydroxylation (Zhou et al., 2021). It is noted that kaolinite is decomposed into active silica and amorphous alumina with low crystallinity and hydration and gelling properties (**eq. (7)**). When the temperature rises to 800 °C, muscovite is significantly enhanced by thermal decomposition into siliceous or silicon-alumina amorphous phases (**eq. (8)**).

$$Al_2(Si_2O_5)(OH)_4 \xrightarrow{400\sim600℃} Al_2O_3 \cdot 2SiO_2 + 2H_2O \quad (7)$$

$$KAl_2(AlSi_3O_{10})(OH)_2 + SiO_2 \xrightarrow{800℃} KAlSi_3O_8 + Al_2SiO_5 + H_2O \quad (8)$$

3.3.4 Effect of calcination on harmful components

NH_4^+-N and Mn^{2+} are the main contaminants in EMR. In the production of manganese ore, ammonia is introduced to neutralize the leachate to form ammonium sulfate. In contrast, the two ore one-step method is adopted due to the decrease in ore grade, which changes the procedure while reduces the introduction of NH_4^+-N. As a result, the characteristic diffraction peak of ammonium sulfate (28.5 °) is not obvious in the XRD results. **Fig.6** shows that the characteristic diffraction peak of ammonium sulfate gradually weakens between 200-400 °C and disappears in the diffraction pattern at 600 °C, indicating that ammonium sulfate escapes as a gas between 400-600 °C. Meanwhile, part of sulfate also partially escaped as gas during the temperature-rise period (above 800 °C). The chemical reactions are shown in **equations (9)** and **(10).**

$$(NH_4)_2SO_4 \cdot H_2O \xrightarrow{200\sim400℃} (NH_4)_2SO_4 + H_2O \quad (9)$$

$$3(NH_4)_2SO_4 \xrightarrow{>400℃} 4NH_3 + N_2 + 3SO_2 + 6H_2O \quad (10)$$

The residual manganese in the EMR is mainly in the form of manganese sulfate and manganese

oxides, which causes the low crystallinity of manganese in the EMR. The manganese sulfate is mainly dehydrated and decomposed at 800 °C to form Mn_2O_3 (**eq. (11-12)**). The part of the manganese sulfate gradually converted into Mn_3O_4 with the calcination temperature higher than 800 °C (**eq. (13)**). The Mn-hercynite compound is formed by calcining Fe_2O_3 and Mn_3O_4 formed as the temperature exceeds 900 °C (**eq. (14)**).

$$MnSO_4 \cdot H_2O \xrightarrow{100\sim600℃} MnSO_4 + H_2O \quad (11)$$

$$2MnSO_4 \xrightarrow{>600℃} Mn_2O_3 + SO_2 + SO_3 \quad (12)$$

$$6Mn_2O_3 \xrightarrow{>800℃} 4Mn_3O_4 + O_2 \quad (13)$$

$$Fe_2O_3 + Mn_3O_4 \xrightarrow{900\sim1000℃} MnFe_2O_4 + Mn_2O_3 \quad (14)$$

The mass loss of the EMR prepared at different calcination temperatures are shown in **Table 5**. The overall mass loss decreases with increasing temperature, which is attributed to the reduction in mass due to dehydration, decomposition, amorphization and podzolization. Specifically, the overall mass loss of EMR is reduced by 3.91%, 6.60%, 3.94%, 3.59% and 5.34% after calcination at 200, 400, 600, 800 and 1000°C, respectively. The water stores between the pores in the porous fineness slag caused by sulfuric-acid leaching, which requires the continuous calcination to achieve complete dehydration (Wang et al., 2020). The TG curves of the calcined EMR are consistent with the analysis in **Fig. 4**, all detailed data are shown in **Fig. S2**.

Table 5. The loss in mass of $R\text{-}EMR^{HSI}$ and $C\text{-}EMR^{HSI}_{200\sim1000}$ at different temperature stages

Sample	Loss in mass (%)					$\sum$ Stage (I~V) Loss in mass
	Stage Ⅰ 35-200℃	Stage Ⅱ 200-400℃	Stage Ⅲ 400-600℃	Stage Ⅳ 600-800℃	Stage Ⅴ 800-1000℃	
$R\text{-}EMR^{HSI}$	5.5164	4.6503	6.2278	2.2211	6.7697	25.3853
$C\text{-}EMR^{HSI}_{200}$	1.2893	3.1128	7.5591	2.4491	7.0693	21.4796
$C\text{-}EMR^{HSI}_{400}$	0.4536	0.2390	1.6875	8.8236	3.0756	14.8793
$C\text{-}EMR^{HSI}_{600}$	0.5614	0.1451	0.2596	5.0881	4.8822	10.9364
$C\text{-}EMR^{HSI}_{800}$	0.2323	0.0425	0.0340	1.8411	5.2005	7.3504

C-EMR$^{HSI}_{1000}$	0.023	0.0066	0.0132	0.0494	1.9138	2.006

In conclusion, the increase in temperature on the one hand facilitates the resourceful recovery of valuable elements. On the other hand, the increase in the content of amorphous substances via calcination is accompanied by dehydration and recrystallization of hydrated minerals into high-activity states. In addition, increasing temperature promotes the aluminosilicate activation and sulfate decomposition, which increase alkalinity and reduces hazardous elements. Thus, the thermodynamic treatment has significant advantages for the resourceful and harmless treatment of EMR.

3.4 Pozzolanic activity of C-EMR^{HSI}

In order to find an optimal calcination temperature for EMR with good pozzolanic activity and compressive strength, the compressive strength of the EMR-blended mortar was tested at 3, 14, 28, 60 and 90 days. The results of SAI test in mortar with 30% EMR at different calcination temperatures are shown in **Table 6**. The control sample with 100% cement was set for comparative analysis. In general, a sample with a SAI of 75% at 28 days is considered as a standard pozzolanic material. The 28-day SAI of the EMR-blended mortar calcining at 200, 800 and 1000 °C all exceeded 75%, in particular the maximum SAI at 800 °C was 84.79%. Therefore, the EMR calcined at 200, 800 and 1000 °C can be classified as a high pozzolanic activity material. In addition, the SAI of all samples increased with the curing age, in which the highest SAI at 800 °C was 87.96%. The reasons for these phenomena are closely related to the evolution of the mineral phases (He et al., 2021c; Zhou et al., 2021).

Table 6. Compressive strength and SAI of EMR-blended mortar

Samples	3 days		14 days		28 days		60 days		90 days	
	CS (MPa)	SAI (%)	CS (MPa)	SAI (%)	CS (MPa)	SAI (%)	CS (MPa)	SAI (%)	CS (MPa)	SAI (%)
PC	16.20	100.00	33.65	100.00	40.75	100.00	44.31	100.00	47.01	100.00
R-EMR^{HSI}	8.50	52.47	22.10	65.68	28.05	68.83	31.52	71.14	33.92	72.15
C-EMR$^{HSI}_{200}$	9.70	59.87	24.81	73.72	30.16	74.01	34.30	77.41	36.78	78.24
C-EMR$^{HSI}_{400}$	6.20	38.27	19.15	56.91	23.80	58.40	27.15	61.27	29.45	62.65
C-EMR$^{HSI}_{600}$	2.55	15.74	17.50	52.01	21.95	53.87	24.75	55.86	27.82	59.18
C-EMR$^{HSI}_{800}$	9.95	61.42	24.95	74.15	34.55	84.79	37.85	85.42	41.35	87.96
C-EMR$^{HSI}_{1000}$	9.75	60.19	23.71	70.46	30.91	75.85	34.33	77.48	39.45	83.92

In early hydration, EMR has a significant retardation on cement hydration due to the presence of gypsum. Thus, the SAI values of all EMR-blended mortar specimens are below 75%. The hemihydrate gypsum phase formed at 160 °C could improve the reactivity of EMR (Zhou et al., 2021). However, the hemihydrate gypsum phase continues to dehydrate with increasing temperature to form a poorly crystalline β-type gypsum phase, which reduces the pozzolanic activity of EMR. Meanwhile, the decomposition of other mineral phases and gas evaporites synergistically builds a porous EMR microstructure, which significantly increases the water absorption of EMR, especially at 400°C and 600°C. It means that the actual water-cement ratio of the mortar decreases and then reduces the fluidity of the mortar and is not conducive to the development of strength. Although kaolinite is dehydrated and decomposed in the range of 400-600°C to form the silica-alumina phase, but the low temperature silica and amorphous aluminum phase formed at this stage do not contribute significantly to the strength development (**Figs. 6** and **S2**). With the increase of calcination temperature, the gypsum phase is thermally decomposed to increase the active calcium oxide content, and the existing silica-alumina phase is activated to form amorphous silica-alumina material. However, the pozzolanic

activity of EMR calcined at 1000 °C is reduced due to recrystallization of amorphous minerals and the massive formation of Mn_3O_4, which also caused a slight decrease in SAI.

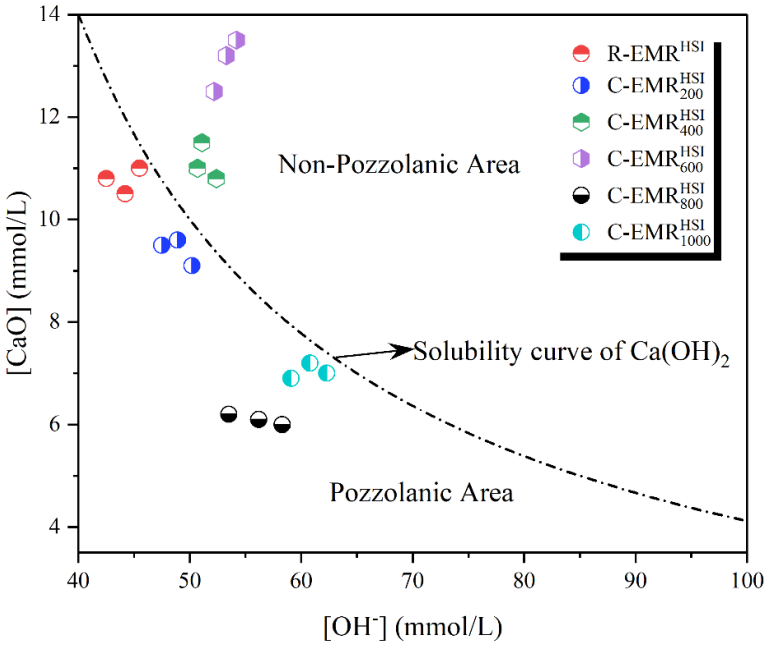

Fig. 7. Frattini test results for EMR with different calcination temperatures after curing at 40°C for 8 days.

Fig. 7 shows the results of the Frattini test for EMR replacing 30% cement blended paste. In the range of 35 and 90 mmol/L [OH], the theoretical maximum [CaO] concentration can be calculated using the equation given in EN 196-5 to plot the $Ca(OH)_2$ solubility curve at 40 ℃,

$$\text{Max[CaO]} = \frac{350}{\text{[OH]-15}} \quad (15)$$

Fig. 7 shows that the positions of R-EMR^{HSI}, C-EMR^{HSI}_{400} and C-EMR^{HSI}_{600} are on the $Ca(OH)_2$ solubility isotherm and this region is defined as the range of non-pozzolanic activity. Test samples within this range lacked qualifying pozzolanic activity. For C-EMR^{HSI}_{200}, C-EMR^{HSI}_{800} and C-EMR^{HSI}_{1000}, the test results all lie below the calibration line, indicating that the samples have a good pozzolanic activity. In particular, when the calcination temperature is increased to 800 °C, the [CaO] and $[OH^-]$ positions of the tested samples were far below the $Ca(OH)_2$ solubility isotherm. It indicates that the Ca^{2+} and OH^- released by cement hydration are consumed by the pozzolanic reaction of EMR.

Therefore, the EMR calcined at 800°C can be considered as a high pozzolanic activity material, which is consistent with the SAI test results.

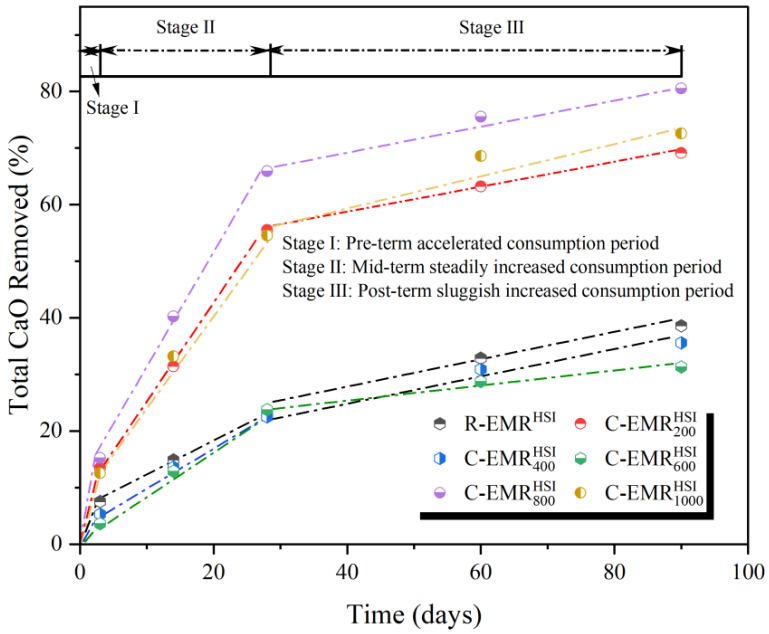

Fig. 8. Results of SL tests with EMR at different calcination temperatures in sealed plastic bottles at 40 °C after 3, 14, 28, 60 and 90 days.

Fig. 8 shows the consumption of saturated lime with EMR after different calcination temperatures. The results can be divided into three stages based on the consumption rate of saturated lime, which are the pre-term accelerated consumption period, mid-term steadily increased consumption period and post-term sluggish increased consumption period. All samples exhibit a rapid lime consumption over 3 days. Specifically, the total lime consumption of the $C\text{-}EMR^{HSI}_{800}$ was 65.87% at 28 days. It is noted that the sample had a lime consumption rate of 0.21% per hour for the first 3 days and an overall lime consumption rate of approximately 0.1% per hour by 28 days, which slowed down again with longer curing age. This is consistent with the SAI results, which reached a value of 84.79% at 28 days. In addition, the calcined samples with high SAI exhibit a greater amount of lime consumption

compared to the samples with low SAI. Overall, lime consumption tests occurred at an accelerated rate during the first 3 days curing age and were essentially complete during the 28 days curing age.

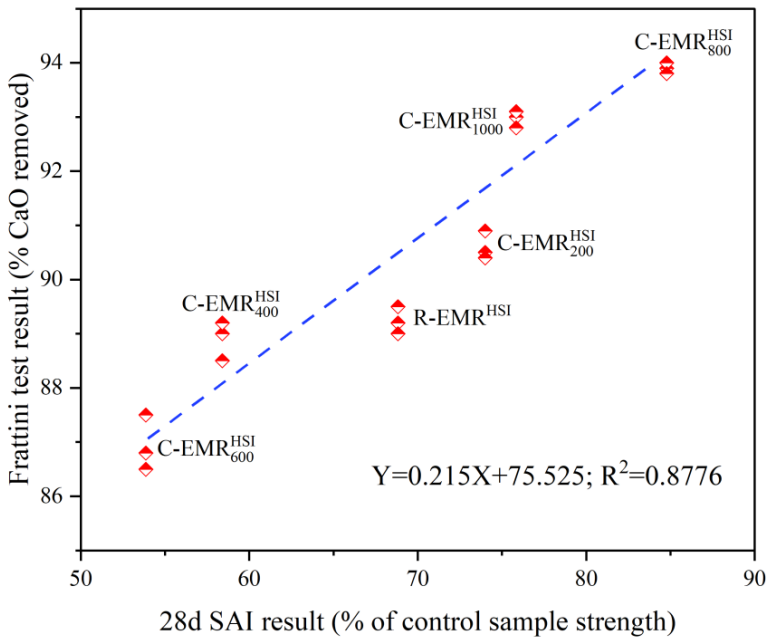

Fig. 9. Correlation between Frattini test and 28-d SAI of EMR at different calcination temperatures.

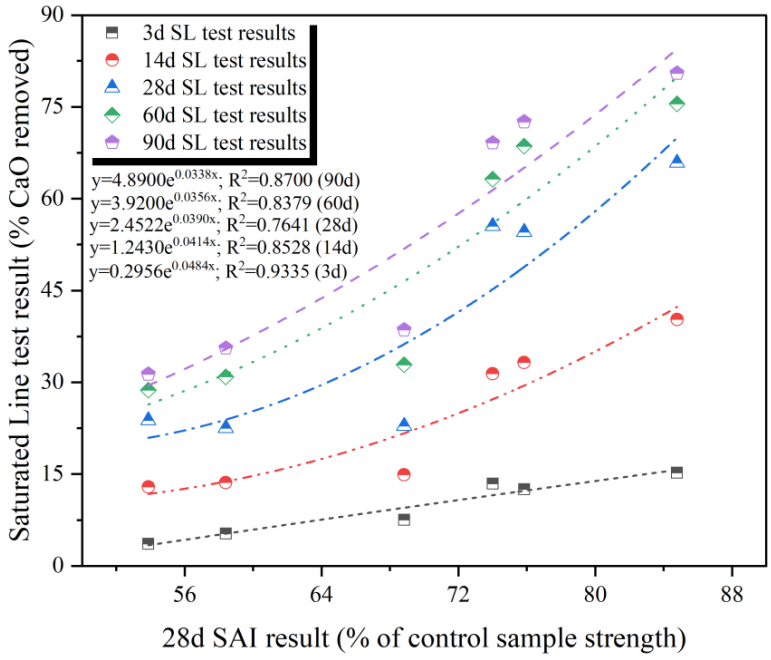

Fig. 10. Correlation between result of 28-d SAI and SL tests (3, 14, 28, 60 and 90 days).

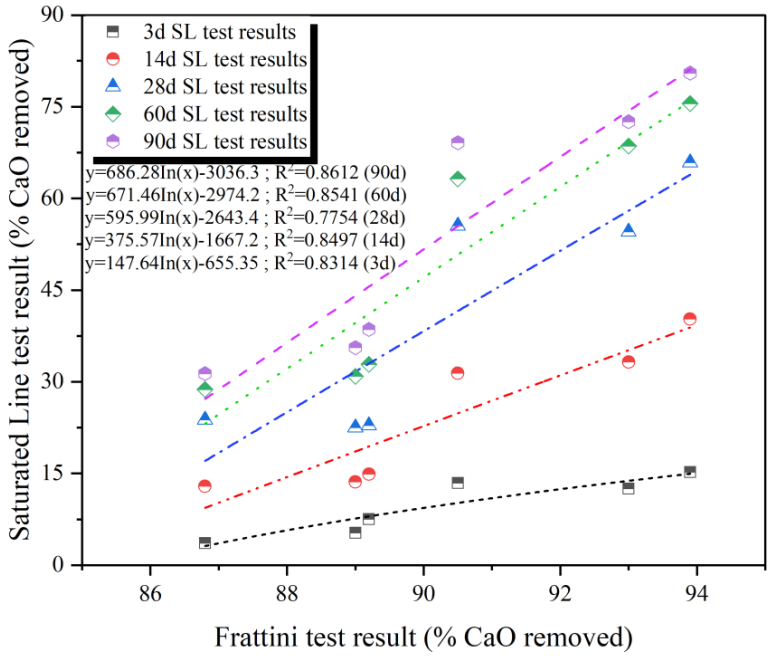

Fig. 11. Correlation results of the 8-d Frattini test and SL tests (3, 14, 28, 60 and 90 days)

Based on **Figs. 9-11**, there is a significant correlation between the SAI results and the Frattini test results (R^2 = 0.8776). In contrast, although Frattini test and SL test, SA1 test and SL test also have a good correlation, the test conditions and errors lead to poor stability. It may be that the mass ratio of lime to EMR formed by mixing 7 g cement with 3 g EMR in the Frattini and SAI tests is much lower than the ratio formed by mixing 1 g of EMR with 75 ml of saturated lime solution in the SL test.

Due to the lower ratio of lime to EMR, the SL test exhibits a higher pozzolanic activity compared to the Frattini test. In addition, unlike the SAI and Frattini tests, where there is no cement and no bulk solid phase is formed because the SL test uses a different system. Further, a small amount of solid $Ca(OH)_2$ passing through the filter has greater buffers in the titration and introduces large errors. Also, previous studies indicated that the SAI test was performed at 23°C for 28 days, while the Frattini test was conducted at 40°C for 8 days (Tironi et al., 2013).

3.5 Effect of calcined EMR on cement hydration

3.5.1 Hydration kinetics

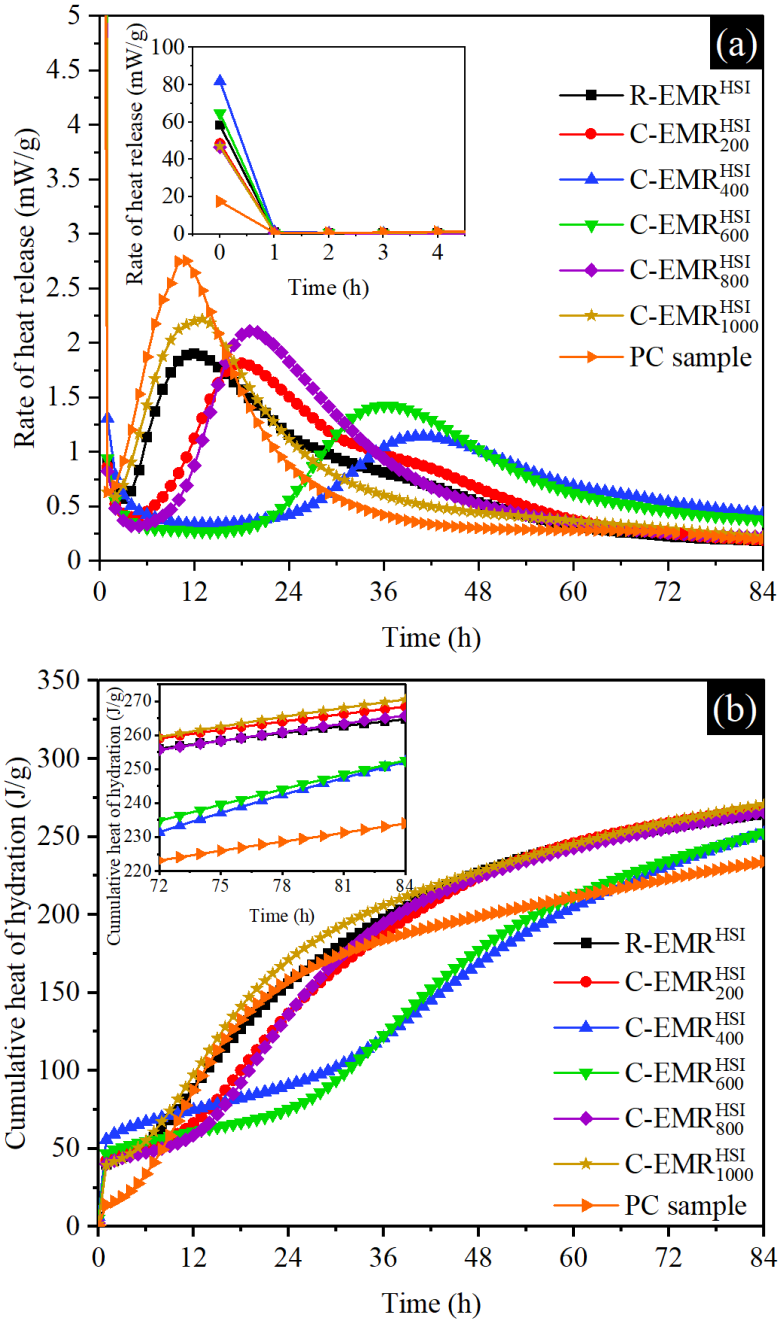

Fig. 12. Exothermic hydration of the EMR-blended slurry (a) rate of heat release (b) cumulative heat of hydration

The results of the exothermic heat of hydration of the slurry mixed with calcined EMR are shown

in **Fig. 12**. The results of setting time and soundness of cement and EMR-blended mortar are presented in Table S1. The mixture consisting of 30% EMR to 70% cement with a water/binder ratio of 0.5 was analyzed in-depth. **Fig. 12** shows that the hydration exothermic peaks of EMR at calcinations of 400 and 600 °C are shifted to the right with various degrees, implying that the addition of EMR is able to retard the hydration process (Table S1). Compared with previous PC results, the addition of EMR reduces the intensity of hydration exothermic peak, especially in the slurry prepared by EMR calcined at 400 °C and 600 °C (He et al, 2021c). The retardation of cement hydration is attributed to two possible reasons: one aspect is the synergistic contribution of the high-water absorption of EMR particles with dissolved sulfate ions (Zhou et al., 2021). The majority of the water are first absorbed by the calcined EMR particles while much less water is used for the cement hydration than for the stoichiometry. On the other hand, a large amount of sulfate ions dissolved in the slurry reacts with calcium and aluminum phase to form hydration products, which adsorb on the surface of the cement particles. It retards the dissolution of cement particles and inhibits the growth of crystals (Wang et al., 2013; Xu et al., 2019).

The exothermic peak of hydration of samples mixed with $C\text{-}EMR^{HSI}_{800}$ and $C\text{-}EMR^{HSI}_{1000}$ is much higher than the other samples, which can be considered that the calcined EMR promotes the hydration reaction. The cumulative heat of hydration of slurry mixed with $C\text{-}EMR^{HSI}_{800}$ and $C\text{-}EMR^{HSI}_{1000}$ was 265 J/g and 269.7 J/g for 84 h, respectively. It also confirms that the activation of EMR on cement components, such as C_3A (Xu et al., 2019). The exothermic peak of hydration of the slurry mixed with $C\text{-}EMR^{HSI}_{200}$ and $R\text{-}EMR^{HSI}$ is lower than that with $C\text{-}EMR^{HSI}_{800}$ and $C\text{-}EMR^{HSI}_{1000}$, but higher than that with $C\text{-}EMR^{HSI}_{400}$ and $C\text{-}EMR^{HSI}_{600}$, which is also closely related to the transformation of the gypsum and the formation of amorphous activated substance. The existing studies indicated that the calcined EMR at 160 ℃ has a high reactivity due to the presence of the

hemihydrate gypsum phase. On the other hand, calcination above 360 ℃ decreases the reactivity of EMR while increasing its water absorption due to the generation of low-activity anhydrous gypsum.

3.5.2 Analysis of hydration products

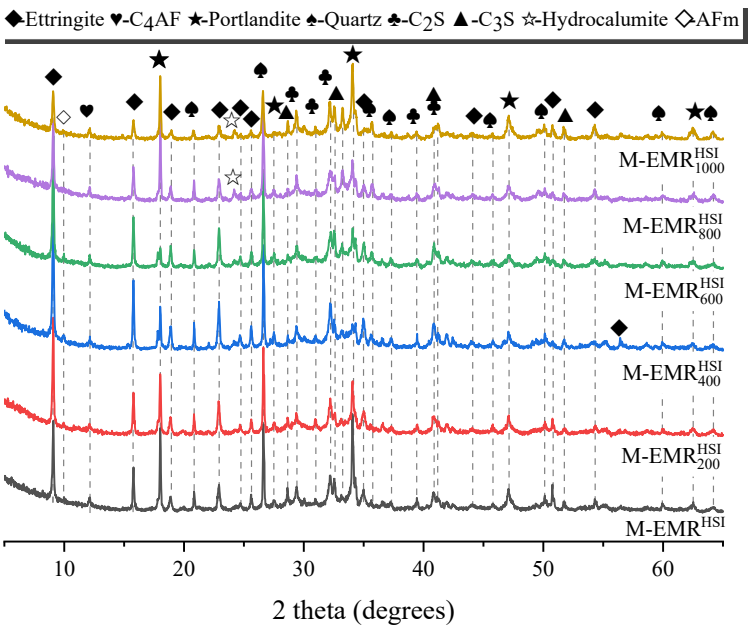

Fig. 13. XRD patterns of EMR-blended mortar curing at 28 days.

Fig. 13 shows results of hydration products of the mixed mortar prepared by EMR at different calcination temperatures after curing for 28 days. The main hydration product phases of the EMR blended mortar were ettringite, AFm (monosulfate), hemi-sulfate and common cement hydration products. **Fig. 13** exhibits that the calcium alumina phase is present in large amounts in the hydration products of mortar. The mortar formed by $C\text{-}EMR_{200}^{HSI}$, $C\text{-}EMR_{400}^{HSI}$ and $C\text{-}EMR_{600}^{HSI}$ produce large amounts of ettringite due to the large amount of gypsum with high temperature transformation. Meanwhile, the formation of aluminate phase may be provided by the high temperature calcination of EMR. **Fig. 13** also shows that the diffraction peak intensity of ettringite increases and then decreases with increasing calcination temperature. In contrast, the diffraction peak of portlandite decreases and then increases with increasing calcination temperature. The mixed mortar prepared by

EMR calcined at 400 and 600 ℃ produces a large amount of calcium alumite and a small number of portlandite. By contrast, the blended mortar prepared by EMR calcined at 800 and 1000 ℃ formed less ettringite and aluminate phases and more portlandite. It is closely related to the high temperature transformation of the gypsum and aluminosilicate phases in the EMR.

3.5.3 Microstructure analysis

Fig. 14 shows the SEM images of the 30% EMR-blended mortar after 28 days of curing. In mortar with 70% PC, portlandite with good crystallinity layered is produced to form a dense structure, and C-S-H gels formed by hydration are interspersed with needle-like ettringite. With the addition of EMR, more discernible pores are observed in the ENR-blended mortar, resulting in a loose microstructure. These pores not filled by hydration products can adversely affect the mechanical properties of the mortar. In addition, a large number of ettringite occurred in $R\text{-}EMR^{HSI}$, $C\text{-}EMR^{HSI}_{200}$, $C\text{-}EMR^{HSI}_{400}$ and $C\text{-}EMR^{HSI}_{600}$ samples due to the presence of gypsum phases. There are significant differences in the morphology of ettringite produced by different gypsum phases. Especially for the mortar blended with $C\text{-}EMR^{HSI}_{400}$ and $C\text{-}EMR^{HSI}_{600}$, a large amount of needle-like ettringite fills the microstructure of the mortar, forming a large number of pores structure. It also verifies the reason for the poor mechanical properties of the mortar blended with $C\text{-}EMR^{HSI}_{400}$ and $C\text{-}EMR^{HSI}_{600}$. The AFm phase with hexagonal lamellar crystals and a large amount of portlandite were found in the mortar blended with $C\text{-}EMR^{HSI}_{800}$ and $C\text{-}EMR^{HSI}_{1000}$. The SEM images of mortar mixed with $C\text{-}EMR^{HSI}_{800}$ and $C\text{-}EMR^{HSI}_{1000}$ exhibit that the short rod-like and vermiculite-like C-S-H gels are formed due to the introduction of additional Si and Al elements from EMR, which reduces the Ca/Si ratio of the gels. However, C-S-H gels with different morphology can not be considered as the products of hydration or EMR-active reactions. The effect of EMR on calcium silicate hydrate gels, including their composition and morphology, needs further investigation.

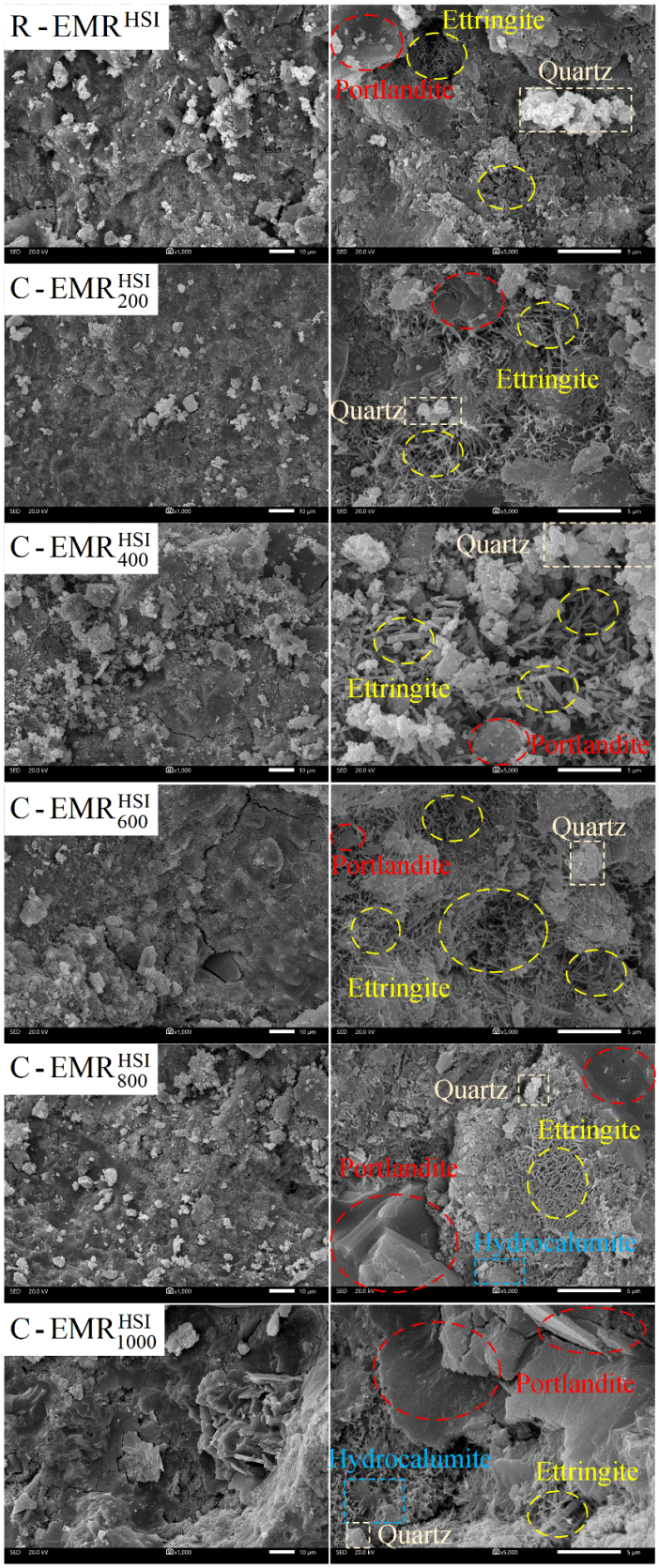

Fig. 14. SEM micrographs of pretreated EMR (0, 200, 400, 600, 800 and 1000 ℃) blend mortar.

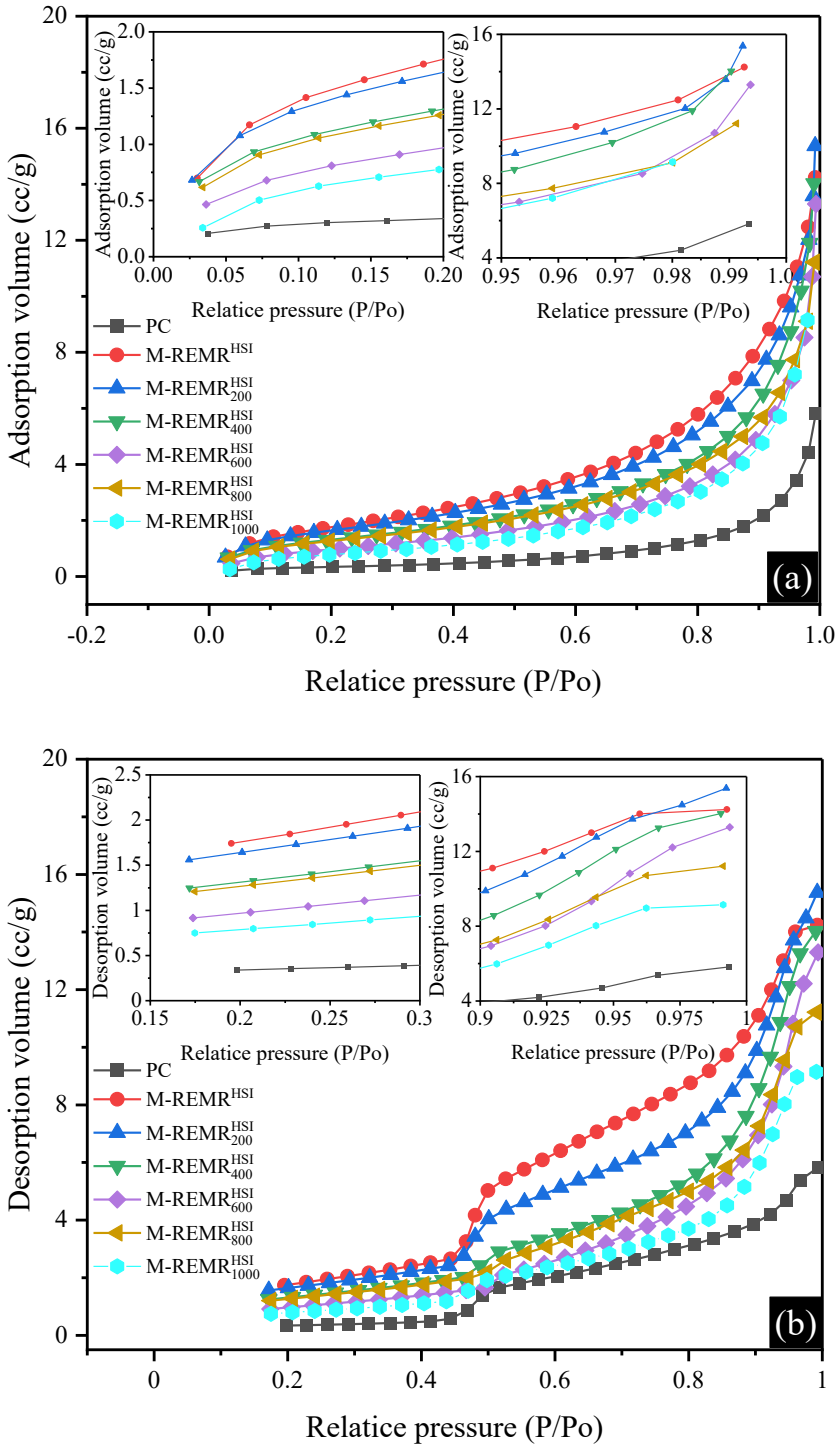

Fig. 15. Nitrogen adsorption isotherm patterns (a) adsorption curve and (b) desorption curve of EMR-blend mortar.

Pore distribution of the EMR-blended mortar is shown in **Fig. 15**. All samples exhibited a hysteresis effect, which indicates that the EMR-blended mortar is unevenly distributed and mostly large pores.

With the addition of EMR, the pore volume of EMR-blended mortar increases. It can be explained by the loose porous properties of EMR (Xu et al., 2013). In addition, the diversity of types and structures of hydration products in the presence of EMR leads to more pores in the mortar structure.

Fig. 15a indicates that the adsorption volume of the EMR-blended mortar decreases with the increase of calcination temperature, which indicates that calcination can reduce pore volume of the mortar. And the desorption curve in **Fig. 15b** exhibits that the desorption volume of the EMR-blended mortar shifts from type-H3 type to type-H4 as the calcination temperature increases. It implies the non-uniform slit-like pores in the mortar are transformed into homogeneous slit-like pores. The test result suggests that the macropores of mortar may be partially or fully filled by the hydration products of EMR. The results of the pore distribution are in agreement with the SAI results and further confirm the occurrence of EMR pozzolanic activity, which is beneficial for the strength development.

3.6 Leaching characteristics analysis

Heavy metal contaminants in EMR, such as Mn, Cr and Zn, are a matter of great concern when used in construction materials (Duan et al., 2011; Han et al., 2020; He et al., 2021b). To ensure the safety of EMR utilization, the toxicity characteristic leaching procedure (TCLP) was used to determine the leaching concentration of raw EMR, calcined EMR, and EMR-blended mortar.

The TCLP test results are shown in **Table 7**. It indicates that the leaching concentrations of heavy metals were well below the standard limits for all samples. In the EMR, the concentrations of Zn and Mn were higher than the other minor constituents. The direct utilization of EMR may bring contaminants into the finished product and cause secondary environmental pollution. After the pretreatment of calcination, the leaching concentration of heavy metal decreases with the increase of calcination temperature. The glassy and crystalline products produced during the calcination can

incorporate metal ions into the amorphous network and crystal structure, leading to the immobilization of heavy metals (Shu et al., 2019a, 2020; Sun et al., 2020). In comparison with calcined EMR, mortar containing 30% EMR exhibited a relatively low leaching concentration, except for elemental Cr that may come from raw PC. In the mortar, heavy metals may be embedded in the hydration products or form precipitates with other ions (Xu et al., 2019). In addition, the dense structure of EMR-blended mortar prevents the leaching behavior of heavy metal. In conclusion, the immobilization of heavy metals in the calcination process and in the mortar leaves no significant concerns for the future utilization of EMR in building materials.

Table 7. Leaching concentrations of EMR-blended mortar using the TCLP

Sample	Concentration of heavy metals (mg/L)								
	Cr	Pb	As	Cu	Zn	Ba	Cd	Se	Ni
R-EMR^{HSI}	0.200	0.010	0.010	0.020	6.500	0.050	0.020	0.010	0.200
C-EMR$^{HSI}_{200}$	0.100	0.050	0.050	0.010	7.000	0.020	0.020	0.050	0.110
C-EMR$^{HSI}_{400}$	0.100	0.040	0.020	0.040	7.200	0.020	0.020	0.070	0.150
C-EMR$^{HSI}_{600}$	0.200	0.050	0.080	0.050	7.500	0.010	0.010	0.080	0.150
C-EMR$^{HSI}_{800}$	0.050	0.020	0.030	0.020	1.200	0.010	0.010	0.020	0.020
C-EMR$^{HSI}_{1000}$	0.002	0.010	0.010	0.010	0.500	0.010	0.010	0.020	0.010
M-REMR^{HSI}	0.002	0.002	0.001	0.005	1.200	0.005	0.002	0.020	0.010
M-CEMR$^{HSI}_{200}$	0.001	0.001	0.005	0.001	2.200	0.002	0.002	0.008	0.020
M-CEMR$^{HSI}_{400}$	0.001	0.002	0.002	0.004	2.700	0.001	0.002	0.008	0.010
M-CEMR$^{HSI}_{600}$	0.002	0.003	0.008	0.005	2.500	0.002	0.001	0.005	0.050
M-CEMR$^{HSI}_{800}$	0.001	ND	0.003	0.002	0.700	ND	0.001	0.001	0.050
M-CEMR$^{HSI}_{1000}$	ND	0.001	0.001	0.001	0.050	ND	0.001	ND	ND
PC	ND	0.004	0.001	0.003	ND	0.005	0.001	ND	ND
GB5085.3-2007	15.0	5.0	5.0	100.0	100.0	100.0	1.0	1.0	5.0
GB5085.3-1996	1.50	1.0	0.5	2.0	5.0	-	0.1	0.5	1.0

Note: ND: not detected.

In addition, the variations of soluble Mn^{2+} and NH_4^+-N content in EMR are also of interest. **Table 8** shows the leaching concentration of calcined EMR under different leaching conditions. It indicates that the leaching content of Mn^{2+} and NH_4^+-N at strong acid condition (pH=2.88) are higher than the weak acid conditions (pH=4.93 and 7). Under the strong acid condition (pH=2.88), the content of Mn^{2+} and NH_4^+-N in the raw material was 127.74 and 15.14 times higher than the standardized limits, while the content of Mn^{2+} and NH_4^+-N in the water leaching was 67.5 and 12.06 times higher than the standardized limits. After calcinating at 200, 400 and 600 ℃, the leaching of Mn^{2+} did not decrease significantly but increase due to the water loss. When the calcinating temperature exceeds 800 ℃, the Mn^{2+} is fixed in glass and crystals in the form of oxides, resulting in a significant decrease in the leaching value and complied with the standard limits (GB5085.3-1996; GB5085.3-2007). The content of NH_4^+-N escapes as a gas at temperatures above 280 °C. When the calcination temperature exceeds 600 °C, the emission of NH_4^+-N complies with the standard (GB5085.3-1996).

Table 8. Leaching concentrations of EMR using the TCLP

Samples	Acid (pH=2.88) leaching		Acid (pH=4.93) leaching		Water (Ph=7) leaching	
	Mn (mg/L)	NH_3-N (mg/L)	Mn (mg/L)	NH_3-N (mg/L)	Mn (mg/L)	NH_3-N (mg/L)
R-EMR^{HS1}	638.70	378.50	543.20	367.50	337.50	301.40
C-EMR$^{HSI}_{200}$	655.20	375.20	564.80	344.20	344.10	311.20
C-EMR$^{HSI}_{400}$	805.10	54.10	641.30	48.40	410.50	24.50
C-EMR$^{HSI}_{600}$	851.50	21.60	710.60	17.30	466.80	10.70
C-EMR$^{HSI}_{800}$	41.71	1.20	38.10	0.90	24.10	ND
C-EMR$^{HSI}_{1000}$	35.81	0.20	29.20	ND	18.70	ND

GB5085.3-1996	5.00	25.00	5.00	25.00	5.00	25.00

The results of the Mn^{2+} and NH_4^+-N in EMR-blended mortar at different curing ages are shown in **Table 9**. The 3-d leaching concentrations of Mn^{2+} and NH_4^+-N in mortar prepared by raw EMR and EMR calcined at 200 °C still exceeded standard limit. Meanwhile, the 3-d leaching of Mn^{2+} in the EMR-blended mortar mixed with the EMR calcined at 400 °C and 600 °C also exceeded the standard limits. As the continued cement hydration promotes the solidification of Mn^{2+} and the release of NH_4^+-N, all the specimens meet the standard limits after 28-d. The leaching of Mn^{2+} and NH_4^+-N of mortar formed by EMR calcined at temperatures above 800 °C for 3 d, 28 d and 90 d were all in accordance with the standard limits (GB5085.3-1996).

Table 9. Leaching concentrations of EMR mortar using the TCLP

Samples	3 days		28 days		90 days	
	Mn (mg/L)	NH_3-N (mg/L)	Mn (mg/L)	NH_3-N (mg/L)	Mn (mg/L)	NH_3-N (mg/L)
M-REMR^{HSI}	55.20	27.20	2.80	7.20	2.81	5.60
M-CEMR$^{HSI}_{200}$	62.50	25.50	3.20	5.20	3.11	5.10
M-CEMR$^{HSI}_{400}$	75.20	12.40	4.70	3.10	4.85	4.00
M-CEMR$^{HSI}_{600}$	80.10	8.70	4.20	2.00	4.66	3.20
M-CEMR$^{HSI}_{800}$	2.10	1.00	1.10	0.50	1.00	ND
M-CEMR$^{HSI}_{1000}$	0.50	0.10	0.20	ND	0.10	ND
GB5085.3-1996	5.00	25.00	5.00	25.00	5.00	25.00

4 Conclusion

The effects of calcination on the physicochemical properties and pozzolanic activity of EMR were investigated. In addition, the feasibility of EMR as a construction material was explored in terms of hydration kinetics, hydration phase, pore structure and leaching behavior. Based on the experimental

results, the following conclusions can be drawn:

(1) The mineral composition of raw EMR mainly includes jarosite, dihydrate gypsum, quartz, hematite, limonite, muscovite, and other sulfate-based dissolved materials. The high-water absorption of EMR is mainly associated with the gypsum and the formed porous structure after calcination. The density of EMR increases and the BET specific surface area decreases with the increase of calcination temperature, as the open pores of EMR particles become closed.

(2) The EMR calcined at 800℃ has the optimum pozzolanic activity, which is attributed to the decomposition of dihydrate gypsum and the formation of activated calcium, silicon and aluminum oxide. At 200 °C, calcination increased the pozzolanic activity of EMR due to the dihydrate gypsum dehydrated into β-type hemihydrate gypsum. Above 800 °C, the type II anhydrous gypsum weakens and transforms into type I anhydrous gypsum, which is related to the intercalation of fused quartz phases in EMR. The pozzolanic activity of EMR calcined at 1000°C was reduced due to the recrystallization of amorphous minerals and the formation of stable Mn-spinel (Mn_3O_4) and Mn-hercynite ($MnFe_2O_4$).

(3) A large amount of sulfate ions dissolved in the slurry reacts with calcium and aluminum phase to form hydration products, which adsorbs on the surface of the cement particles. It retards the cement hydration and inhibits the growth of crystals. The pore volume of EMR-blended mortar increases as the addition of EMR, which can be explained by the loose porous properties of EMR. However, the pores volume in the EMR-blended mortar gradually decreased due to the filling effect of the hydration products caused by the increasing pozzolanic activity of EMR.

(4) After calcinating at 200 ℃, the leaching of Mn^{2+} and NH_4^+-N did not decrease significantly but increase due to the water loss. The Mn^{2+} and NH_4^+-N fully below the national standards at calcination above 800°C (GB5085.3-1996; GB5085.3-2007). As the continued cement hydration promotes the

solidification of Mn^{2+} and the release of NH_4^+-N, all the specimens meet the standard limits after 28-d. The leaching of Mn^{2+} and NH_4^+-N of mortar formed by EMR calcined at temperatures above 800 °C for 3 d, 28 d and 90 d were all in accordance with the standard limits (GB5085.3-1996).

(5) The leaching tests results indicated that the leaching concentration of heavy metals decreased with increasing calcination temperature. It is because the glassy and crystalline products produced after calcination can incorporate metal ions into the amorphous network and crystal structure, leading to the immobilization of heavy metals. In EMR-blended mortar, heavy metal may be embedded in the hydration products or form precipitates with other ions. In addition, the dense structure of the mortar prevents the leaching behavior of heavy metal.

All heavy metals are fixed in the cement and calcination process, ensuring the cleaner utilization of EMR in building materials. Further studies on the effect of EMR on the C-S-H composition and structure of concrete, the effect of EMR on other components of concrete, the improvement of EMR reactivity, and the long-term durability of EMR-infused concrete are recommended.

Conflicts of interest

The authors declare no competing financial interests.

Acknowledgements

The authors appreciate the financial support from Hunan Province Key Field R&D Program (Grant No.2020wk2005), and the Postgraduate Scholarship, Central South University, Changsha, China.

CRediT author statement

Fan Wang: Conceptualization**,** Data curation, Writing-Original draft, and Writing-review & editing;

Guangcheng Long: Funding acquisition, Project administration, and Validation; **Min Bai:** Writing-review & editing, Investigation and Validation; **Jilin Wang:** Investigation and Validation; **JohnL Zhou:** Formal analysis, Methodology and Conceptualization, Writing-review & editing; **Xiang Zhou:** Formal analysis.

References

ASTM C618-17A, Standard specification for coal fly ash and raw or calcined natural pozzolan for use in concrete, ASTM International, West Conshohocken, PA, 2019, www.astm.org doi.org/ 10.1520/C0618-17A

Bal, B., Ghosh, S., Das, A. P., 2018. Microbial recovery and recycling of manganese waste and their future application: a review. Geomicrobiol J. 36, 85-96. doi.org/10.1080/01490451.2018.1497731

CEN-CENELEC, EN 196-5:2011. Methods of Testing Cement – Part 5: Pozzolanicity Test for Pozzolanic Cement, CEN-CENELEC, Brussels, Belgium, 2011.

Chen, H., Long, Q., Zhang, Y., Wang, S., Deng, F., 2020. A novel method for the stabilization of soluble contaminants in electrolytic manganese residue: Using low-cost phosphogypsum leachate and magnesia/calcium oxide. Ecotoxicol Environ Saf. 194, 110384. doi.org/10.1016/j.ecoenv.2020.110384

Crumbie, A., Walenta, G., Füllmann, T., 2006. Where is the iron? Clinker microanalysis with XRD Rietveld, optical microscopy/point counting, Bogue and SEM-EDS techniques. Cement Concrete Res. 36(8), 1542-1547. doi.org/10.1016/j.cemconres.2006.05.031

Donatello, S., Tyrer, M., Cheeseman, C. R., 2010. Comparison of test methods to assess pozzolanic activity. Cement Concrete Comp. 32, 121-127. doi.org/10.1016/j.cemconcomp.2009.10.008

Duan, N., Fan, W., Changbo, Z., Chunlei, Z., Hongbing, Y., 2010. Analysis of pollution materials generated from electrolytic manganese industries in China. Resour Conserv Recy. 54, 506-511. doi.org/10.1016/j.resconrec.2009.10.007

Duan, N., Dan, Z., Wang, F., Pan, C., Zhou, C., Jiang, L., 2011. Electrolytic manganese metal industry experience based China's new model for cleaner production promotion. J Clean Prod. 19, 2082-2087. doi.org/10.1016/j.jclepro.2011.06.024

Han, F., Wu, L., 2019. Resource utilization of electrolytic manganese residues, in: Industrial solid waste recycling in western China, 127-164. doi.org/10.1007/978-981-13-8086-0_3

Han, L., Wang, J., Liu, Z., Zhang, Y., Jin, Y., Li, J., Wang, D., 2020. Synthesis of fly ash-based self-supported zeolites foam geopolymer via saturated steam treatment. J Hazard Mater. 393, 122468. doi.org/10.1016/j.jhazmat.2020.122468

Han, Y., Cui, X., Lv, X., Wang, K., 2018. Preparation and characterization of geopolymers based on a phosphoric-acid-activated electrolytic manganese dioxide residue. J Clean Prod. 205, 488-498. doi.org/10.1016/j.jclepro.2018.09.141

Hardjito, D., Antoni, Wibowo, G. M., Christianto, D., 2012. Pozzolanic activity assessment of LUSI (LUmpur SIdoarjo) mud in semi high volume pozzolanic mortar. Materials. 5, 1654-1660. doi.org/10.3390/ma5091654

He, D., Shu, J., Wang, R., Chen, M., Wang, R., Gao, Y., Liu, R., Liu, Z., Xu, Z., Tan, D., Gu, H., Wang, N., 2021a. A critical review on approaches for electrolytic manganese residue treatment and disposal technology: Reduction, pretreatment, and reuse. J Hazard Mater. 418, 126235. doi.org/10.1016/j.jhazmat.2021.126235

He, P., Zhu, J., Chen, Y., Chen, F., Zhu, J., Liu, M., Zhang, K., Gan, M., 2021b. Pyrite-activated persulfate for simultaneous 2,4-DCP oxidation and Cr(VI) reduction. Chem. Eng. J. 406, 126758. doi.org/10.1016/j.cej.2020.126758

He, S., Jiang, D., Hong, M., Liu, Z., 2021c. Hazard-free treatment and resource utilisation of electrolytic manganese residue: A review. J Clean Prod. 306, 127224. doi.org/10.1016/j.jclepro.2021.127224

He, S., Wilson, B. P., Lundstrom, M., Liu, Z., 2021d. Hazard-free treatment of electrolytic manganese residue and recovery of manganese using low temperature roasting-water washing process. J Hazard Mater. 402, 123561.

doi.org/10.1016/j.jhazmat.2020.123561

Hou, P. k., Qian, J. s., Wang, Z., Deng, C., 2012. Production of quasi-sulfoaluminate cementitious materials with electrolytic manganese residue. Cement Concrete Comp. 34, 248-254. doi.org/10.1016/j.cemconcomp.2011.10.003

Lan, J., Dong, Y., Sun, Y., Fen, L., Zhou, M., Hou, H., Du, D., 2021a. A novel method for solidification/stabilization of Cd(II), Hg(II), Cu(II), and Zn(II) by activated electrolytic manganese slag. J Hazard Mater. 409, 124933. doi.org/10.1016/j.jhazmat.2020.124933

Lan, J., Dong, Y., Xiang, Y., Zhang, S., Mei, T., Hou, H., 2021b. Selective recovery of manganese from electrolytic manganese residue by using water as extractant under mechanochemical ball grinding: Mechanism and kinetics. J Hazard Mater. 415, 125556. doi.org/10.1016/j.jhazmat.2021.125556

Lan, J., Sun, Y., Chen, X., Zhan, W., Du, Y., Zhang, T. C., Ye, H., Du, D., Hou, H., 2021c. Bio-leaching of manganese from electrolytic manganese slag by Microbacterium trichothecenolyticum Y1: Mechanism and characteristics of microbial metabolites. Bioresour Technol. 319, 124056. doi.org/10.1016/j.biortech.2020.124056

Lan, J., Sun, Y., Tian, H., Zhan, W., Du, Y., Ye, H., Du, D., Zhang, T. C., Hou, H., 2021d. Electrolytic manganese residue-based cement for manganese ore pit backfilling: Performance and mechanism. J Hazard Mater. 411, 124941. doi.org/10.1016/j.jhazmat.2020.124941

Li, J., Du, D., Peng, Q., Wu, C., Lv, K., Ye, H., Chen, S., Zhan, W., 2018. Activation of silicon in the electrolytic manganese residue by mechanical grinding-roasting. J Clean Prod. 192, 347-353. doi.org/10.1016/j.jclepro.2018.04.184

Li, Q., Liu, Q., Peng, B., Chai, L., Liu, H., 2016. Self-cleaning performance of TiO_2-coating cement materials prepared based on solidification/stabilization of electrolytic manganese residue. Cons Build Mater. 106, 236-242. doi.org/10.1016/j.conbuildmat.2015.12.088

Li, J., Lv, Y., Jiao, X., Sun, P., Li, J., Wuri, L., Zhang, T. C., 2020. Electrolytic manganese residue based autoclaved bricks with $Ca(OH)_2$ and thermal-mechanical activated K-feldspar additions. Cons Build Mater. doi.org/230.10.1016/j.conbuildmat.2019.116848

Liu, Y., Lei, S., Lin, M., Li, Y., Ye, Z., Fan, Y., 2017. Assessment of pozzolanic activity of calcined coal-series kaolin. Appl Clay Sci 143, 159-167. doi.org/10.1016/j.clay.2017.03.038

Ma, M., Du, Y., Bao, S., Li, J., Wei, H., Lv, Y., Song, X., Zhang, T., Du, D., 2020. Removal of cadmium and lead from aqueous solutions by thermal activated electrolytic manganese residues. Sci Total Environ. 748, 141490. doi.org/10.1016/j.scitotenv.2020.141490

Pourkhorshidi, A.R., Najimi, M., Parhizkar, T., Jafarpour, F., Hillemeier, B., 2010, Applicability of the standard specifications of ASTM C618 for evaluation of natural pozzolans. Cement Concrete Comp. 32, 794-800. doi.org/10.1016/j.cemconcomp.2010.08.007

Shu, J., Chen, M., Wu, H., Li, B., Wang, B., Li, B., Liu, R., Liu, Z., 2019a. An innovative method for synergistic stabilization/solidification of Mn^{2+}, NH_4^+-N, PO_4^{3-} and F^- in electrolytic manganese residue and phosphogypsum. J Hazard Mater. 376, 212-222. doi.org/10.1016/j.jhazmat.2019.05.017

Shu, J., Li, B., Chen, M., Sun, D., Wei, L., Wang, Y., Wang, J., 2020. An innovative method for manganese (Mn^{2+}) and ammonia nitrogen (NH_4^+-N) stabilization/solidification in electrolytic manganese residue by basic burning raw material. Chemosphere. 253, 126896. doi.org/10.1016/j.chemosphere.2020.126896

Shu, J., Liu, R., Liu, Z., Chen, H., Du, J., Tao, C., 2016. Solidification/stabilization of electrolytic manganese residue using phosphate resource and low-grade MgO/CaO. J Hazard Mater. 317, 267-274. doi.org/10.1016/j.jhazmat.2016.05.076

Shu, J., Wu, H., Chen, M., Peng, H., Li, B., Liu, R., Liu, Z., Wang, B., Huang, T., Hu, Z., 2019b. Fractional removal of manganese and ammonia nitrogen from electrolytic metal manganese residue leachate using carbonate and struvite precipitation. Water Res. 153, 229-238. doi.org/10.1016/j.watres.2018.12.044

Shu, J., Wu, H., Liu, R., Liu, Z., Li, B., Chen, M., Tao, C., 2018. Simultaneous stabilization/solidification of Mn^{2+} and NH_4^+-N from electrolytic manganese residue using MgO and different phosphate resource. Ecotoxicol Environ Saf. 148, 220-227. doi.org/10.1016/j.ecoenv.2017.10.027

Standards, 1996. The State Bureau of Environmental Protection and The State Bureau of Technical Supervision. Identification standard for hazardous wastes-Identification for extraction procedure toxicity. The State Standard of the People's Republic of China, GB 5085.3-1996, Standards Press of China, Beijing. [in Chinese]

Standards, 2007. The State Bureau of Environmental Protection and The State Bureau of Technical Supervision. Identification standard for hazardous wastes-Identification for extraction procedure toxicity. The State Standard of the People's Republic of China, GB 5085.3-2007, Standards Press of China, Beijing. [in Chinese]

Standards, 2000. The State General Administration of the People's Republic of China for Quality Supervision and Inspection and Quarantine. Methods for chemical analysis of aluminate cement. The State Standard of the People's Republic of China, GB/T 205-2000, Standards Press of China, Beijing. [in Chinese]

Standards, 2005. General Administration of the People's Republic of China for Quality Supervision and Inspection and Quarantine. Pozzolanic materials used for cement production. The State Standard of the People's Republic of China, GB/T 2847-2005, Standards Press of China, Beijing. [in Chinese]

Standards, 2007. The State Environmental Protection Administration. Solid waste-Extraction procedure for leaching toxicity-Acetic acid buffer solution method. The People's Republic of China Environmental Protection Industry Standards, HJ/T 300-2007, China Environmental Science Press, Beijing. [in Chinese]

Standards, 2009a. The Ministry of Environmental Protection. Water quality-Determination of cyanide-Volumetric and spectrophotometry method. The People's Republic of China Environmental Protection Industry Standards, HJ 484-2009, China Environmental Science Press, Beijing. [in Chinese]

Standards, 2009b. The Ministry of Environmental Protection. Water quality-Determination of ammonium nitrogen-Nessler's reagent spectrophotometry. The People's Republic of China Environmental Protection Industry Standards, HJ 535-2009, China Environmental Science Press, Beijing. [in Chinese]

Standards, 2010. The Ministry of Environmental Protection. Solid waste-Extraction procedure for leaching toxicity-Horizontal vibration method. The State Standard of the People's Republic of China, HJ-557-2010, China Environmental Science Press, Beijing. [in Chinese]

Standards, 2017. The Ministry of Environmental Protection. Water quality-Determination of chromium (VI) - Flow injection analysis (FIA) and diphenylcarbazide spectrometric method. The People's Republic of China Environmental Protection Industry Standards, HJ 908-2017, China Environmental Science Press, Beijing. [in Chinese]

Standards, 2017. General Administration of the People's Republic of China for Quality Supervision and Inspection and Quarantine. Fly ash used for cement and concrete. The State Standard of the People's Republic of China, GB/T 1596-2017, Standards Press of China, Beijing. [in Chinese]

Sun, D., Yang, L., Liu, N., Jiang, W., Jiang, X., Li, J., Yang, Z., Song, Z., 2020. Sulfur resource recovery based on electrolytic manganese residue calcination and manganese oxide ore desulfurization for the clean production of electrolytic manganese. Chinese J Chem Eng. 28, 864-870. doi.org/10.1016/j.cjche.2019.11.013

Tironi, A., Trezza, M.A., Scian, A.N., Irassar, E.F., 2013. Assessment of pozzolanic activity of different calcined clays. Cement Concrete Comp. 37, 319-327. doi.org/10.1016/j.cemconcomp.2013.01.002

Wang, D., Wang, Q., Xue, J., 2020. Reuse of hazardous electrolytic manganese residue: Detailed leaching characterization and novel application as a cementitious material. Resour Conserv Recy. 154, 104645. doi.org/10.1016/j.resconrec.2019.104645

Wang, J., Peng, B., Chai, L., Zhang, Q., Liu, Q., 2013. Preparation of electrolytic manganese residue–ground granulated blast furnace slag cement. Powder Technol. 241, 12-18. doi.org/10.1016/j.powtec.2013.03.003

Wang, N., Fang, Z., Peng, S., Cheng, D., Du, B., Zhou, C., 2016. Recovery of soluble manganese from electrolyte manganese residue using a combination of ammonia and CO_2. Hydrometallurgy. 164, 288-294. doi.org/10.1016/j.hydromet.2016.06.019

Wang, Y., Gao, S., Liu, X., Tang, B., Mukiza, E., Zhang, N., 2019. Preparation of non-sintered permeable bricks using electrolytic manganese residue: Environmental and NH_3-N recovery benefits. J Hazard Mater. 378, 120768. doi.org/10.1016/j.jhazmat.2019.120768

Wu, F., Li, X., Zhong, H., Wang, S., 2016. Utilization of electrolytic manganese residues in production of porous ceramics. Int. J. Appl. Ceram. Technol. 13(3), 511-521. doi.org/10.1111/ijac.12502

Xie, H., Li, S., Guo, Z., Xu, Z., 2021. Extraction of lead from electrolytic manganese anode mud by microwave coupled ultrasound technology. J Hazard Mater. 407, 124622. doi.org/10.1016/j.jhazmat.2020.124622

Xu, F., Jiang, L., Dan, Z., Gao, X., Duan, N., Han, G., 2014. Water balance analysis and wastewater recycling investigation in electrolytic manganese industry of China - A case study. Hydrometallurgy 149, 12-22. doi.org/10.1016/j.hydromet.2014.05.002

Xu, L. J., Wang, X. M., Chen, H. C., Liu, C. L., 2011. Mn forms and environmental impact of electrolytic manganese residue. Adv Mater Res. 183-185, 570-574. doi.org/10.4028/www.scientific.net/AMR.183-185.570

Xu, Y., Liu, X., Zhang, Y., Tang, B., Mukiza, E., 2019. Investigation on sulfate activation of electrolytic manganese residue on early activity of blast furnace slag in cement-based cementitious material. Constr Build Mater. 229, 116831. doi.org/10.1016/j.conbuildmat.2019.116831

Yang, C., Lv, X., Tian, X., Wang, Y., Komarneni, S., 2014. An investigation on the use of electrolytic manganese residue as filler in sulfur concrete. Constr Build Mater. 73, 305-310. doi.org/10.1016/j.conbuildmat.2014.09.046

Zhang, R., Ma, X., Shen, X., Zhai, Y., Zhang, T., Ji, C., Hong, J., 2020a. Life cycle assessment of electrolytic manganese metal production. J Clean Prod. 253, 119951. doi.org/10.1016/j.jclepro.2019.119951

Zhang, Y., Liu, X., Xu, Y., Tang, B., Wang, Y., 2020b. Preparation of road base material by utilizing electrolytic manganese residue based on Si-Al structure: Mechanical properties and Mn^{2+} stabilization/solidification characterization. J Hazard Mater. 390, 122188. doi.org/10.1016/j.jhazmat.2020.122188

Zhang, Y., Liu, X., Xu, Y., Tang, B., Wang, Y., Mukiza, E., 2019a. Synergic effects of electrolytic manganese residue-red mud-carbide slag on the road base strength and durability properties. Constr Build Mater. 220, 364-374. doi.org/10.1016/j.conbuildmat.2019.06.009

Zhang, Y., Liu, X., Xu, Y., Tang, B., Wang, Y., Mukiza, E., 2019b. Preparation and characterization of cement treated road base material utilizing electrolytic manganese residue. J Clean Prod. 232, 980-992. doi.org/10.1016/j.jclepro.2019.05.352

Zhou, C., Du, B., Wang, N., Chen, Z., 2014. Preparation and strength property of autoclaved bricks from electrolytic manganese residue. J Clean Prod. 84, 707-714. doi.org/10.1016/j.jclepro.2014.01.052

Zhou, Y., 2021. Reusing electrolytic manganese residue as an activator: The effect of calcination on its mineralogy and activity. Constr Build Mater. 294, 123533. doi.org/10.1016/j.conbuildmat.2021.123533

Application of electrolytic manganese residues in cement products through pozzolanic activity motivation and calcination

Fan Wang[1], Guangcheng Long[2,1], Min Bai[1], Jilin Wang[1], John L. Zhou[1,2], Xiang Zhou[1]

[1] School of Civil Engineering, Central South University, 68 South Shaoshan Road, Changsha, Hunan 410075, China

[2] Centre for Green Technology, School of Civil and Environmental Engineering, University of Technology Sydney, Sydney, NSW 2007, Australia

Supporting Information

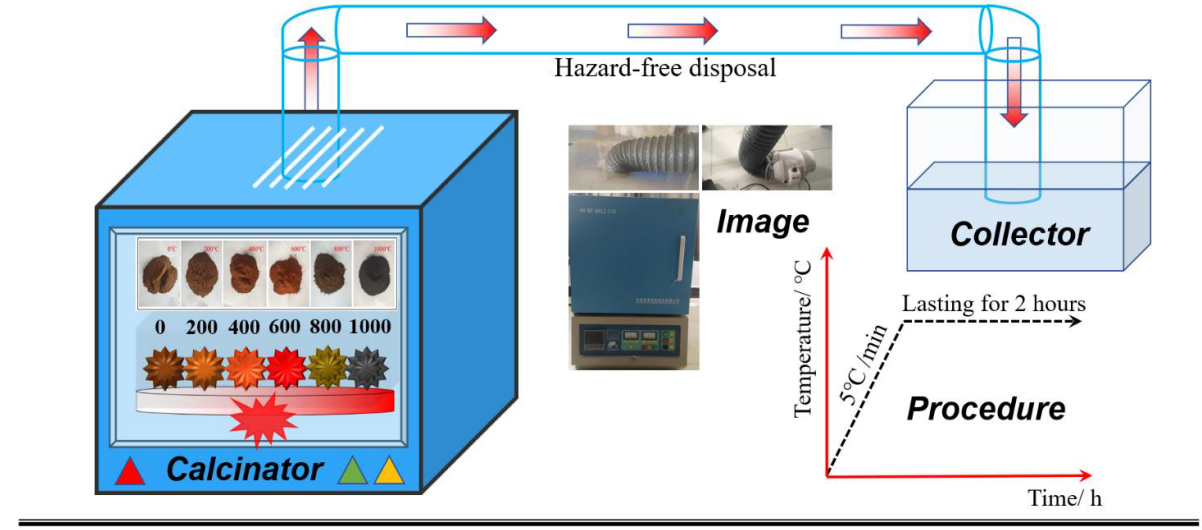

Fig. S1. Calcination, collection and pretreatment system.

[2] Corresponding author: longguangcheng@csu.edu.cn (G. Long)

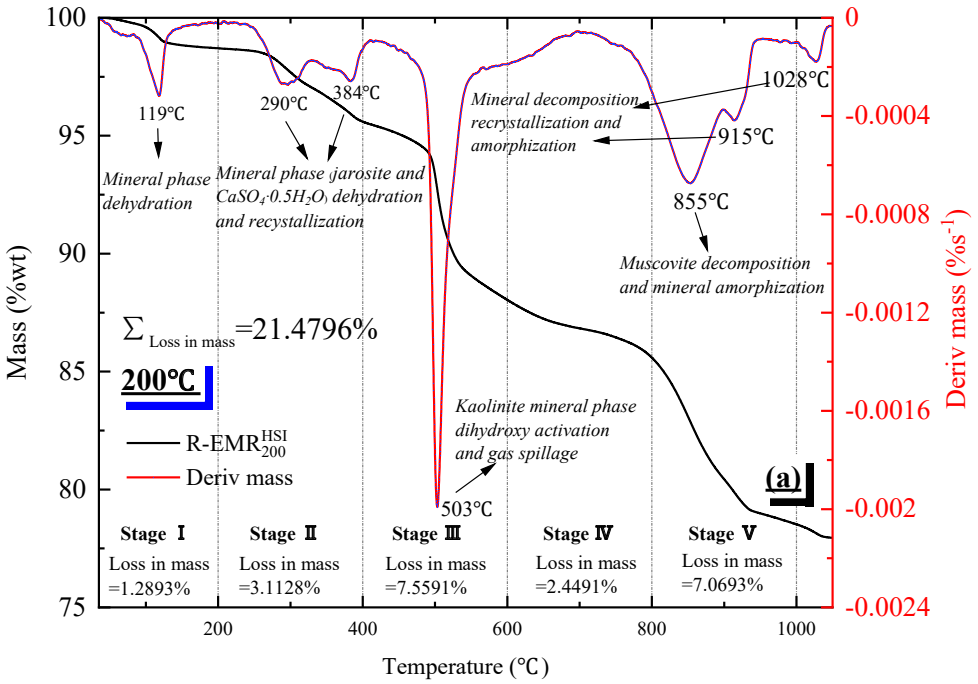
100
95
90
85
80
75
0
-0.0004
-0.0008
-0.0012
-0.0016
-0.002
-0.0024
200
400
600
800
1000
Mass (%wt)
Deriv mass (%s-1)
Temperature (℃)
119℃
290℃
384℃
503℃
855℃
915℃
1028℃
Mineral phase dehydration
Mineral phase (jarosite and CaSO4·0.5H2O) dehydration and recrystallization
Mineral decomposition recrystallization and amorphization
Muscovite decomposition and mineral amorphization
Kaolinite mineral phase dihydroxy activation and gas spillage
∑Loss in mass=21.4796%
200℃
R-EMR200HSI
Deriv mass
(a)
Stage Ⅰ
Loss in mass =1.2893%
Stage Ⅱ
Loss in mass =3.1128%
Stage Ⅲ
Loss in mass =7.5591%
Stage Ⅳ
Loss in mass =2.4491%
Stage Ⅴ
Loss in mass =7.0693%

849

850

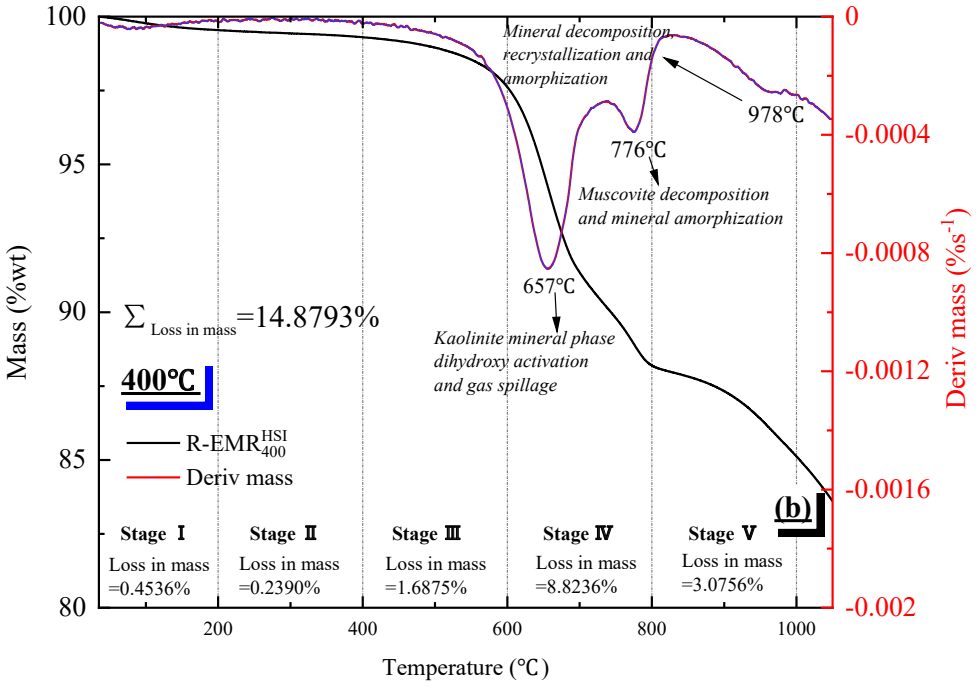
100
95
90
85
80
0
-0.0004
-0.0008
-0.0012
-0.0016
-0.002
200
400
600
800
1000
Mass (%wt)
Deriv mass (%s-1)
Temperature (℃)
657℃
776℃
978℃
Mineral decomposition recrystallization and amorphization
Muscovite decomposition and mineral amorphization
Kaolinite mineral phase dihydroxy activation and gas spillage
∑Loss in mass=14.8793%
400℃
R-EMR400HSI
Deriv mass
(b)
Stage Ⅰ
Loss in mass =0.4536%
Stage Ⅱ
Loss in mass =0.2390%
Stage Ⅲ
Loss in mass =1.6875%
Stage Ⅳ
Loss in mass =8.8236%
Stage Ⅴ
Loss in mass =3.0756%

851

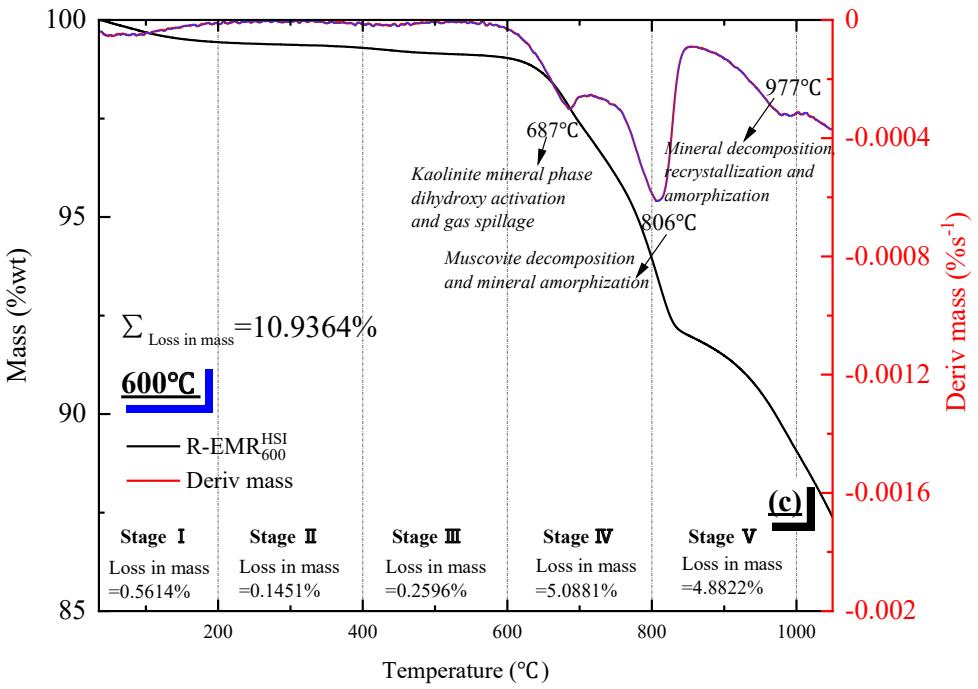
100
95
90
85
0
-0.0004
-0.0008
-0.0012
-0.0016
-0.002
200
400
600
800
1000
Mass (%wt)
Deriv mass (%s^{-1})
Temperature (℃)
977℃
687℃
806℃
Kaolinite mineral phase dihydroxy activation and gas spillage
Mineral decomposition, recrystallization and amorphization
Muscovite decomposition and mineral amorphization
$\sum_{\text{Loss in mass}}$=10.9364%
600℃
R-EMR$^{HSI}_{600}$
Deriv mass
(c)
Stage Ⅰ Loss in mass =0.5614%
Stage Ⅱ Loss in mass =0.1451%
Stage Ⅲ Loss in mass =0.2596%
Stage Ⅳ Loss in mass =5.0881%
Stage Ⅴ Loss in mass =4.8822%

852

853

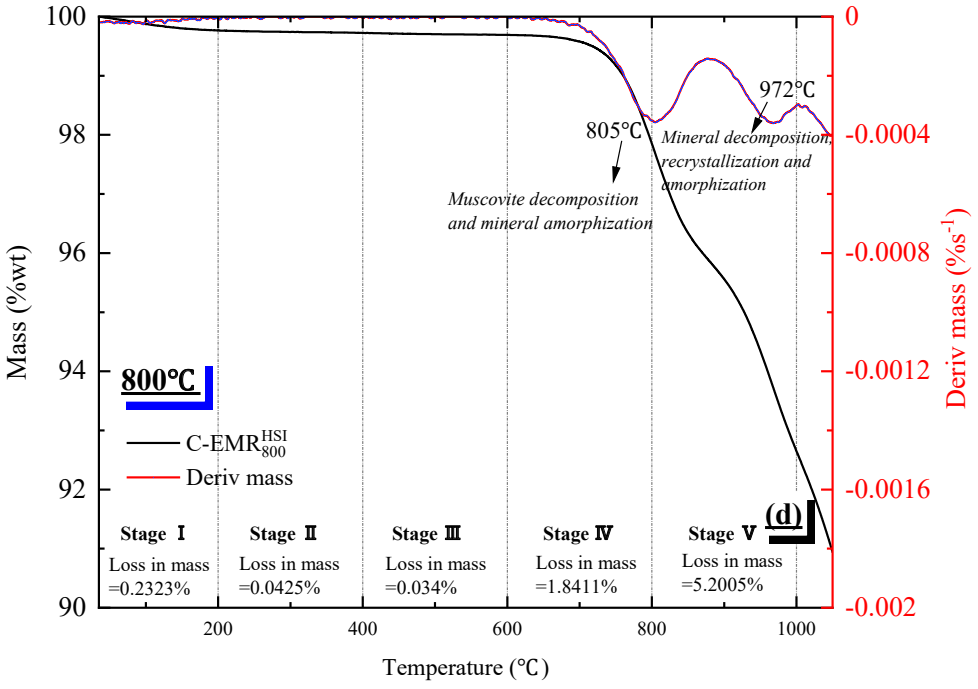
100
98
96
94
92
90
0
-0.0004
-0.0008
-0.0012
-0.0016
-0.002
200
400
600
800
1000
Mass (%wt)
Deriv mass (%s^{-1})
Temperature (℃)
972℃
805℃
Mineral decomposition, recrystallization and amorphization
Muscovite decomposition and mineral amorphization
800℃
C-EMR$^{HSI}_{800}$
Deriv mass
(d)
Stage Ⅰ Loss in mass =0.2323%
Stage Ⅱ Loss in mass =0.0425%
Stage Ⅲ Loss in mass =0.034%
Stage Ⅳ Loss in mass =1.8411%
Stage Ⅴ Loss in mass =5.2005%

854

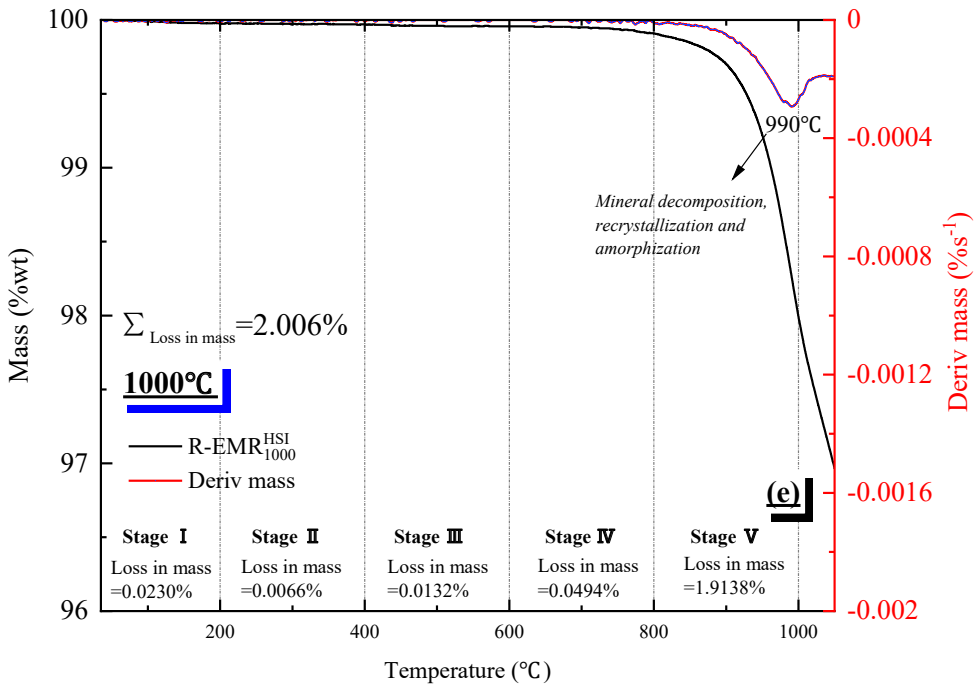

Fig. S2. TG-DTG results of the calcined samples after experiencing the setting calcination temperature treatment (a) 200℃, (b) 400℃, (c) 600℃, (d) 800℃, and (e) 1000℃.

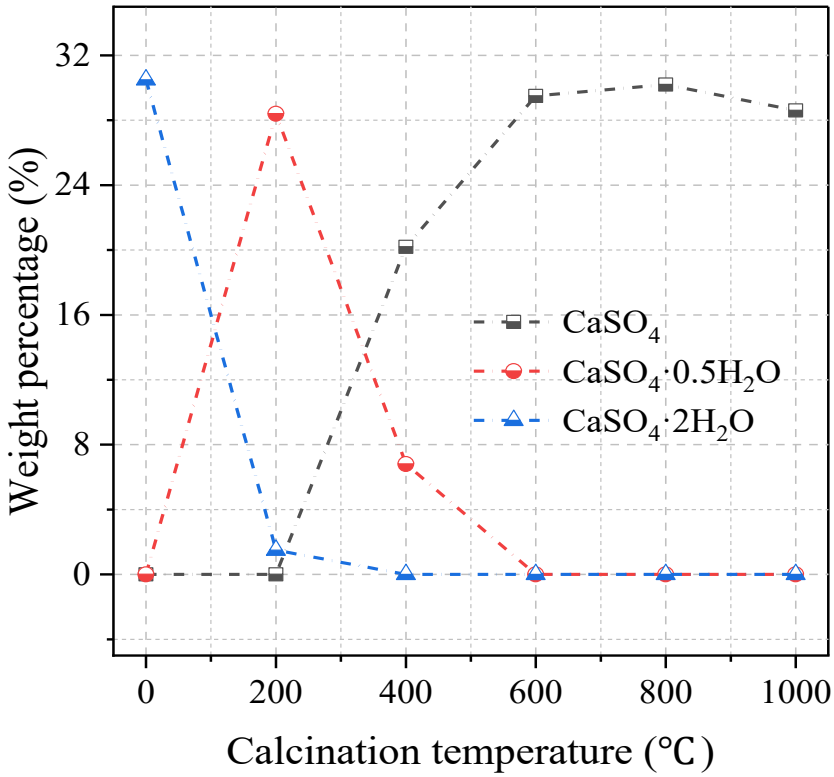

Fig.S3. Quantitative results of gypsum phases at different calcination temperatures

Application of electrolytic manganese residues in cement products through pozzolanic activity motivation and calcination

Fan Wang[1], Guangcheng Long[*1], Min Bai[1], Jilin Wang[1], John L. Zhou[12], Xiang Zhou[1]

[1] School of Civil Engineering, Central South University, 68 South Shaoshan Road, Changsha, Hunan 410075, China

[2] Centre for Green Technology, School of Civil and Environmental Engineering, University of Technology Sydney, Sydney, NSW 2007, Australia

Fan Wang, Email: wn2020@csu.edu.cn

(Corresponding author) Guangcheng Long, Email: longguangcheng@csu.edu.cn

Min Bai, Email: minbai2021@163.com

Jilin Wang, Email: 193571717@qq.com

John L. Zhou, Email: junliang.zhou@uts.edu.au

Xiang Zhou, Email: xiangzhou@csu.edu.cn

[*] Corresponding author: longguangcheng@csu.edu.cn (G. Long)

Highlights

- EMR calcined at 800 ℃ has the optimum strength activity index of 84.79 at 28-d.
- Pozzolan activity of EMR is boosted in β-$CaSO_4 \cdot 0.5H_2O$ and weakened in Mn_3O_4 and $MnFe_2O_4$.
- Presence of gypsum in EMR retards the cement hydration and forms ettringite.
- Mn^{2+} and NH_4^+-N below national standards at calcination above 800 °C.

Graphical abstract

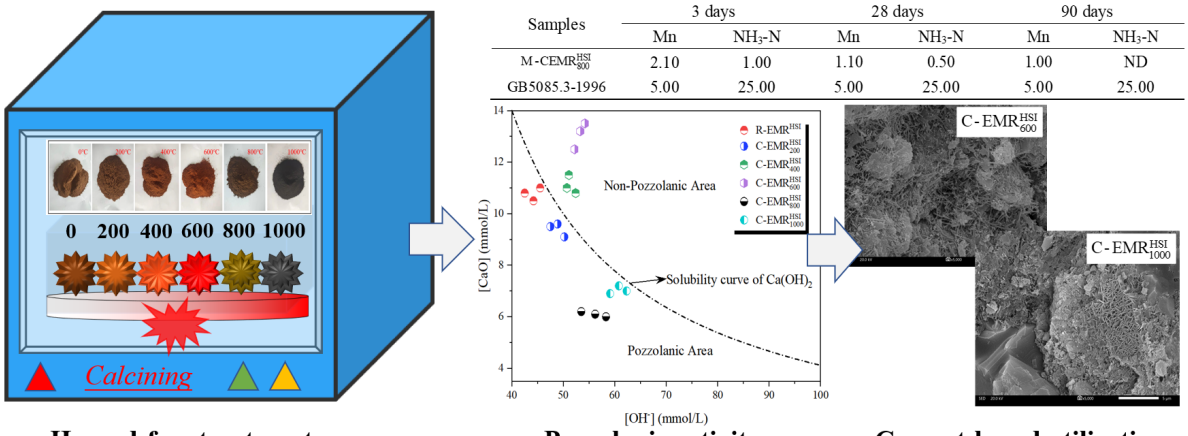

Samples	3 days		28 days		90 days	
	Mn	NH_3-N	Mn	NH_3-N	Mn	NH_3-N
M-CEMR$^{HSI}_{800}$	2.10	1.00	1.10	0.50	1.00	ND
GB5085.3-1996	5.00	25.00	5.00	25.00	5.00	25.00

Hazard-free treatment **Pozzolanic activity** **Cement-based utilization**

Abstract

Degradation in grade of manganese ore aggravates the complexity of electrolytic manganese residue (EMR). Calcination is one of the most practical pretreatment methods to improve EMR activity and dispose the hazardous elements. In this paper, the evolution of mineral phase, pozzolanic activity, pore structure and harmful components induced by calcining EMR was investigated. The results show that EMR calcined at 800 ℃has the strength activity index (SAI) of 84.79 at 28 d, which is attributed to the decomposition of dihydrate gypsum and the formation of activated calcium, silicon and aluminum oxide. The formation of β-type hemihydrate gypsum increases the pozzolan activity, while the latter is limited by the formation of stable Mn-spinel (Mn_3O_4) and Mn-hercynite ($MnFe_2O_4$). In the EMR-doped mortar matrix, the production of a large amount of ettringite due to the existence of gypsum, as well as common C-S-H, portlandite and AFm, which strongly verify the pozzolanic activity of EMR. Leaching results show that Mn^{2+} and NH_4^+-N could not be eliminated completely at low temperature (< 600 ℃), but could be completely stabilized in the alkaline environment provided by the cement. The Mn^{2+} and NH_4^+-N levels in mortar are fully below the regulatory standards when calcinated above 800°C. All heavy metals are fixed in the cement and calcination process, ensuring the cleaner utilization of EMR in building materials.

Keywords: Calcination; Electrolytic manganese residue; Pozzolanic activity; Hazard-free treatment; Mortar stabilization.

1 Introduction

Electrolytic manganese is an essential metallurgical and raw material that is widely used in the production of batteries, steels, alloys, building and other industries (Duan et al., 2010; Duan et al, 2011). China is currently the top producer of electrolytic manganese with an annual production of over 1.5 million tons, accounting for approximately 98% of global output (Xu et al., 2014; Zhou et al., 2014; Shu et al., 2016; Li et al., 2016; Han and Wu, 2019; He et al., 2021a). Electrolytic manganese residue (EMR) is a hazardous solid waste produced as a byproduct after the traditional sulfuric acid leaching of manganese carbonate ore and ammonia neutralization (Wang et al., 2019; Wang et al., 2020; He et al., 2021b).

Currently, fabricating one ton of electrolytic manganese metal could produce about 10-14 tons of EMR (Shu et al., 2016; Wang et al., 2019; Shu et al., 2019a). It is noted that this condition has worsened rapidly due to the continued depletion of global raw ore (Duan et al., 2010; He et al., 2021c). The stacked EMR with a high-water content of 25-35 wt.% and a low-pH range of 5.0-6.5, and the particle size of 20-500 μm, which changes with the disposed time and formation process (Han and Wu, 2019). In addition, EMR contains not only a large number of soluble salts, such as ammonium sulfate and manganese sulfate, but also heavy metal elements including Ni, Co, Cd, Pb, Cu, etc (He et al., 2021c; Shu et al., 2020b; Ma et al., 2020; Wang et al., 2020). The discharged EMR is significantly difficult to be disposed because of its diversity, fineness, and viscosity (Duan et al, 2011; Zhang et al., 2020b; He et al., 2021c). Therefore, electrolytic manganese smelters dispose of their EMR in designated waste landfill sites without any effective pretreatment (Duan et al, 2011; Wang et al., 2020; He et al., 2021c). It is inevitably that a large amount of landfill sites and the surrounding soil and groundwater may be seriously polluted (Han and Wu, 2019). In addition, as the continuous stockpiled EMR is exposed to the open-air environment, inevitably soluble metal sulfate and

ammonium sulfate decomposition occurs, resulting in harmful gases emissions (e.g., SO_2 and NH_3) (Wang et al., 2016; Sun et al., 2020; Li et al., 2016). Therefore, the stored EMR has significantly hindered the development of the manganese industry and posed a serious threat to the ecological environment (He et al., 2021c; Lan et al., 2021a). These environmental problems caused by EMR have currently attracted widespread concern in society, and urgently need solutions.

At present, the existing landfills can dispose of EMR in bulk, but the subsequent secondary pollution does not solve the problem completely (He et al., 2021b). Utilization of water leaching, acid leaching, and bioleaching treatments can effectively extract the valuable substances from EMR, but the disposal of secondary contamination induced by the leachate is still an inevitable hidden trouble (Duan et al., 2010; Bal et al., 2018; Han et al., 2018; Lan et al., 2021b; He et al., 2021c, 2021d). The stabilization/solidification technology can be used to immobilize hazardous components in EMR, and the disposed EMR is directly applied in building materials (Chen et al., 2020; Han et al., 2020; He et al., 2021d; Lan et al., 2021a). The resource utilization of EMR has been realized to a certain extent. However, its application in engineering practice is severely limited by high immobilization charges, uncontrollable hardening efficacy and potential re-leaching risks. However, calcination is widely employed in the solid waste pretreatment procedure as one of the most environmentally friendly disposal methods (Xu et al., 2011; Li et al., 2018; Ma et al., 2020; He et al., 2021d). Calcination has many benefits with respect to other methods, as the hazardous substances in EMR are cleaned during the calcination process. Although the calcination causes energy consumption, a small minority of the heat released by calcination can be used for power generation, while the collected gases are made into chemical reagents or recycled reserves (Shu et al., 2020; Zhang et al., 2020; Zhou, 2021). More importantly, compared with untreated EMR, calcined EMR tends to have high reactivity and is more suitable for the production of building materials, such as bricks, ceramics, lightweight aggregates and

93 supplemental cementitious materials (Yang et al., 2014; Wu et al., 2016; Wang et al., 2019; Zhang et
94 al., 2019a, 2019b; Xu et al., 2019; Zhang et al., 2020a; Han et al., 2020; Zhou et al., 2021). Meanwhile,
95 the quasi-sulfoaluminate cement with high compressive strength was manufactured by EMR (close
96 to 40%) combined with limestone and kaolinite calcined at 1200°C (Hou et al., 2012). Numerous
97 studies have explored the recycling alternatives of EMR in building materials, especially the potential
98 use as a substitute for cement in mortar and concrete (Hou et al., 2012; Lan et al., 2021d). The high
99 specific surface area and gypsum phase of EMR significantly increase the unit water demand, and
100 gypsum accelerates cement hydration as it promotes ettringite production and provides more
101 nucleation space for precipitation of hydration products (Zhou et al., 2021). It is expected that EMR
102 can replace part of the cement and obtain acceptable mechanical strength and significant economic
103 benefits due to the higher pozzolanic activity (Ma et al., 2020; Zhou et al., 2021). Calcination or
104 incineration temperature has a significant effect on the reactivity of EMR. Recent studies have
105 confirmed that the potential pozzolanic activity of EMR can be activated by thermal treatment, either
106 by incineration alone or in combination with other solid wastes (Wang et al., 2013; Liu et al., 2017;
107 Li et al., 2018; Li et al., 2020; Xie et al., 2021).
108 Notwithstanding the satisfying results for EMR-combined matrix, more research is needed
109 regarding the effect of heat treatment on the physicochemical properties and pozzolan activity of
110 EMR. Therefore, this paper aims to identify and quantify the changes in the physicochemical
111 properties and pozzolanic activity of EMR disposed by different calcination temperatures. The
112 evolution of physicochemical characteristics and mineral phase of the undisturbed and calcined EMR
113 was characterized. Then, their pozzolan activity was analyzed in terms of the mortar strength activity
114 index, Frattini test and calcium hydroxide consumption. The effects of EMR at different calcination
115 temperatures on cement hydration, product phase formation and the microscopic pore structure of the

cementitious matrix were investigated. The leaching test was used to determine the leaching content of harmful components of EMR and the EMR-blended matrix with different calcination temperatures.

2 Material and methods

2.1 Raw materials

The EMR used was obtained from an electrolytic manganese smelter from Xiangtan Electrochemical Group. It is noted that the raw EMR is yellow mud-like material different from the common black (**Fig.1a**), which is due to the pyrite and soft manganese ore are introduced to two ore one-step process. Prior to test, the in-situ EMR was first dried at 75 ℃ for 72 hours, and then crushed and ground until it passed through a 150 meshes sieve with a specific surface area of 4.01 m^2/g (measured by nitrogen adsorption BET method). The basic physical characteristics of EMR according to ASTM standard are shown in **Table 1**.

The microstructure of EMR was described using scanning electron microscopy (SEM) (**Fig. 1b**). The results showed the grinded EMR particles with different sizes and morphologies, in which the smaller particles tend to cluster around the larger particles. The particle size distribution of EMR was detected with a particle size analyzer, as shown in **Fig. 2**. The chemical compositions of EMR and ordinary Portland cement (OPC) are shown in **Table 2**. As can be seen, the EMR has a large loss on ignition (LOI) of 18.24 % due to its high-water content. In addition to that, the raw EMR has a superior sulfate and iron, so the raw EMR is labeled R-EMR^{HSI}. Besides, the estimated Bogue potential phase composition of tested PC is shown in **Table 3**.

Table 1. Basic physical parameter of EMR

Feature	Water content (%)	Density ($g \cdot cm^{-3}$)	Stacking density ($g \cdot cm^{-3}$)	Mass fraction of water-soluble substance (%)	pH
Value	31.2±2	2.8±0.2	0.9±0.1	15.5±2	6.2±0.2

Table 2. The chemical compositions of EMR and ordinary Portland cement

Sample	SiO_2 (%)	CaO (%)	Fe_2O_3 (%)	Al_2O_3 (%)	MgO (%)	SO_3 (%)	MnO (%)	Cr_2O_3 (%)	LOI (%)
EMR	34.67	5.58	21.21	9.01	0.61	20.53	3.94	0.03	19.6
OPC	20.08	63.41	3.01	5.29	2.06	2.17	N. D	1.62	3.6

Note: N. D stands for not detected.

Table 3. Potential phase composition of tested OPC

Clinker	C_3S	C_2S	C_3A	C_4AF
Mass fraction (%)	54.4	22.6	6.9	10.1

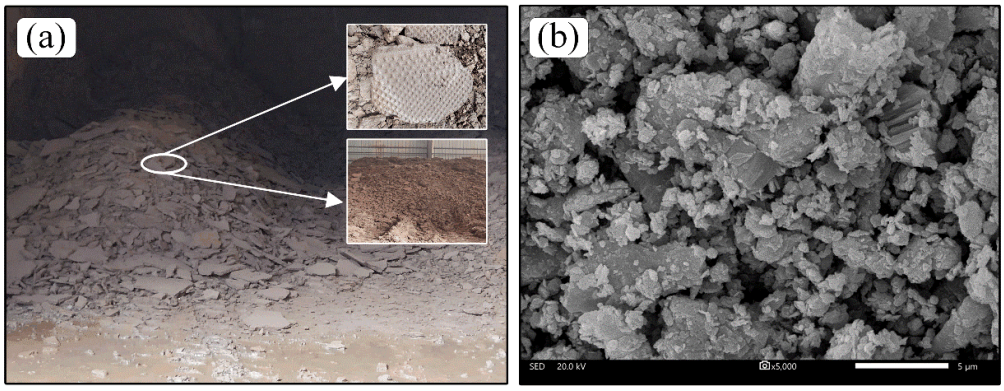

Fig. 1. The R-EMR^{HSI} stockpiles produced by the two ore one-step process (a) the storage field of the R-EMR^{HSI} (b) the microstructure of EMR by SEM.

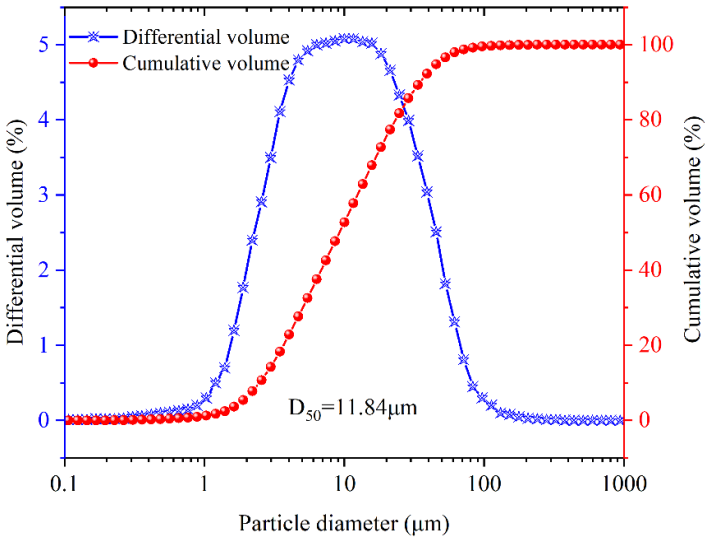

Fig. 2. The specific particle size distribution of R-EMR^{HSI} by BET method.

2.2 Different calcining temperatures

The calcined high-sulfur and iron-based EMR (C-EMR^{HSI}) was prepared at the desired calcining temperature in a muffle furnace. Calcining was conducted with a controlled airflow, where any flue-gas generated was collected and treated by a recovery device (**Fig. S1**). Five calcination temperatures (200 ℃, 400 ℃, 600 ℃, 800 ℃, 1000 ℃) were set and compared with the R-EMR^{HSI} to investigate the evolution of mineral phases and the fluctuation of pozzolanic activity. To promote the high-quality calcination, R-EMR^{HSI} was calcined for lasting 2 hours after increasing the temperature to the setting value at the heating rate of 5 ℃/min. After calcination, the C-EMR^{HSI} was rapidly collected from the muffle furnace, and then promptly cooled in the air. The label "C_{200}-EMR^{HSI}" means that the EMR^{HSI} calcined at 200 ℃was used to follow-on operational test and evaluation, and so does the other ‘‘EMR-temperature" labels.

2.3 Characterization methods

The chemical compositions of R-EMR^{HSI} and C-EMR^{HSI} were determined using the X-ray

fluorescence (XRF, Bruker S4 Pioneer spectrometer). The mineralogical compositions of the R-EMR^{HSI} and C-EMR^{HSI} were identified using an X-ray diffractometer (XRD, Bruker D8 Advance diffractometer) employing Cukα radiation (λ = 0.154 nm, 40 kV, 50 mA) over scanning range 2θ = 5–80° with step width 2°/min^{-1}. The results of mineral phases were quantified by XRD-Rietveld analysis (Crumbie et al., 2006). The transition of mineral phases at various elevated temperatures was characterized by simultaneous thermal analyzer (TG-DTG, 50-1200 ℃, 10 ℃/min). The morphology of R-EMR^{HSI} and C-EMR^{HSI} was observed by a scanning electron microscope (SEM, JSM-6490LV, 20.0 kV with different magnification times). The particle size distribution and the specific surface area of R-EMR^{HSI} and C-EMR^{HSI} were determined by laser particle size scanning analyzer (BT-9300S, Bettersize Instruments Ltd., CN) and the Brunauer-Emmett-Teller (BET)-N_2 adsorption method, respectively. The density and water absorption of R-EMR^{HSI} and C-EMR^{HSI} was determined using a pycnometer with kerosene as a medium and tea-bag method, respectively.

2.4 Evaluation of calcined EMR pozzolanic activity

The pozzolanic activity of C-EMR^{HSI} samples was analyzed by strength activity index (SAI) test, Frattini test and saturated lime (SL) consumption test.

SAI test

The SAI results were used to characterize the pozzolanic activity of supplementary cementitious materials (Liu et al., 2017; Pourkhorshidi et al., 2010; Tironi et al., 2013). The SAI was calculated as the ratio of the compressive strength of the blended mortar to that of the referred ordinary Portland cement at the same curing age, as shown in equation (1). The compressive strength of blended mortar at 3, 14, 28, 60 and 90 days was detected to characterize the pozzolanic activity of C-EMR^{HSI} at different temperatures based on the Chinese standard (GB/T 1596-2017). Compared with ASTM

C618-17A, the pozzolanic activity of C-EMR^{HSI} was amplified by replacing 20% pozzolanic and 80% cement with 30% pozzolanic and 70% cement mixed mortar. The compressive strength of blended cement was evaluated on mortar cubes (4 cm ×4 cm×4 cm) performed with fixed sand/ binder (1:3 by mass ratios) and water/ binder mass ratios (1:2). After the strength test, some fragments on the sample center were collected and then immersed in ethyl alcohol for 48 hours and then dried at 60 ℃ over 12 hours to eliminate the moisture.

$$SAI = \frac{CS_A}{CS_B} \quad (1)$$

where, CS_A is the compressive strength of the tested C-EMR^{HSI} sample (MPa) and CS_B is the compressive strength of the controlled mortar (MPa). In comparison with ASTM C618, the test sample has a positive pozzolanic activity as SAI greater than 0.75 after 7 and 28 days at 20% cement replacement. According to GB 2847-2005, the test specimen possesses a positive pozzolanic activity as the results of SAI greater than 0.65 after 28 days with 30% cement replacement.

Frattini test

Based on EN 196-5, the Frattini test involves chemical titration to determine the concentrations of dissolved [Ca^{+}] and [OH^{-}] in a solution with 30% pozzolanic and 70% cement. Thus, 14 g cement and 6 g C-EMR^{HSI} mixed with 100 mL deionized water for preparing test samples. The pozzolanic activity of the tested sample was qualified as the test result was lower than the concentration of $Ca(OH)_2$ in saturation concentration at the same alkalinity. The samples were sealed for 8 days in a cylindrical polyethylene container and then placed in water bath kettle at 40 ℃. The solution was filtered in vacuum and then cooled to ambient temperature upon test ages to detect. The filtrates were titrated with 0.1 mol/L HCl solution with methyl orange indicator and 0.015 mol/L EDTA solution to analyze [OH^{-}] and [Ca^{2+}], respectively. The comparative analysis was made with the solubility curve of $Ca(OH)_2$ at 40 ℃as the reference. The C-EMR^{HSI} was defined as active pozzolanic material when

211 [Ca^{2+}] and [OH^{-}] in solution were down the solubility isotherm.

212 **SL consumption test**

213 Considering the Frattini test only qualitatively determined the pozzolanic activity of C-EMR^{HSI}, the
214 SL test was performed to further investigate the reacted yield and rate of C-EMR^{HSI} with $Ca(OH)_2$.
215 Thus, a mixture consisting of C-EMR^{HSI}, $Ca(OH)_2$ and water was fabricated as a certain weight ratio
216 of 1:1:2. Then, the samples were placed in the water bath at 40 ℃until the specified test ages. Samples
217 were then filtered and titrated for [OH^{-}] and [Ca^{2+}] using the same procedure as the aforementioned
218 Frattini test. Notably, the absolute amount of $Ca(OH)_2$ in the system is settled and the raised
219 temperature guarantee rapid reaction with the pozzolan substance (Hardjito et al., 2012).

220

221 **2.5 Leaching test**

222 The leaching tests of R-EMR^{HSI} and C-EMR^{HSI} were conducted using the horizontal vibration
223 extraction procedure (HJ/T 300-2007; HJ-557-2010; HJ 908-20). The fragmentized samples (5g each)
224 were placed into a plastic bottle with a solid/ liquid mass ratio of 1:20 (100 mL), respectively. After
225 vibrating for 8 hours at a frequency of $120min^{-1}$ and then sitting for 16 hours, all samples were filtered
226 and stored for inductively coupled plasma optical emission spectrometry (ICP-OES) tests. Atomic
227 absorption spectrophotometry inflame was used for determining the concentration of metal ions (HJ
228 484-2009). NH_4^{+}-N was measured via Nessler's reagent spectrophotometry method of HJ 535-2009
229 (Standards, 2009b) and GB/T 205-2000 (Standards, 2000).

230

231 # 3 Results and discussion

232 **3.1 Physicochemical characteristics and mineral composition of R-EMR^{HSI}**

233 The XRD diagram of dried EMR is given in **Fig. 3**. The mineral composition of dried EMR mainly

includes jarosite, dihydrate gypsum, quartz, kaolinite, hematite, limonite, muscovite, and other sulfate-soluble substances. On the one hand, these mineral phases are derived from the additional mineral phases of low-grade manganese ore. On the other hand, the hydrometallurgical process of sulfuric acid leaching combined with two ore one-step method (pyrite) accumulating a large amount of soluble sulfate. Compared with the previous EMR, the introduction of sulfuric iron ore caused a substantial increase in the concentration of the iron phase (He et al., 2021c). The manganese ore not only formed fine particle under the strong chemical reaction accompanied by sulfuric acid leaching, but also reconstructed into porous particle morphology (**Fig. 2**).

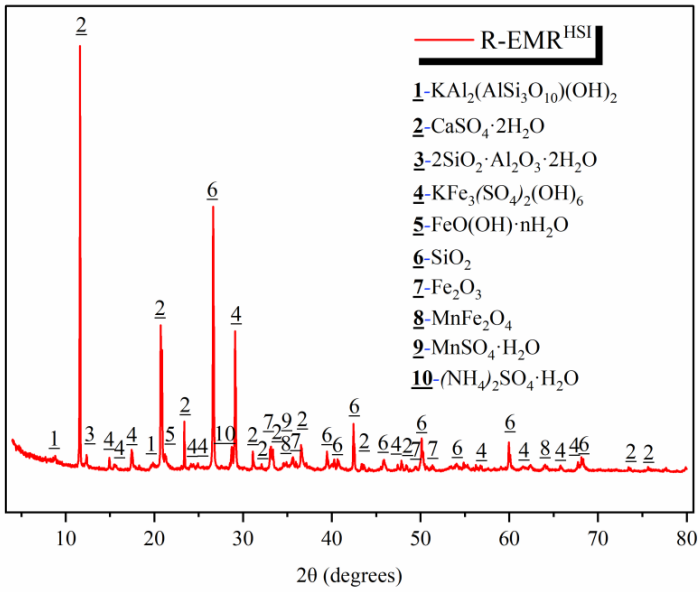

Fig. 3. The mineralogical compositions of the R-EMR^{HSI}.

It is clear from **Fig. 3** that crystal of quartz and gypsum phase has the most intact and sharp diffraction peaks at 26.6° and 11.6° (2θ), respectively. Other mineral phases have lower crystallinity, lower intensity peaks and dispersed peak shapes. From the production of EMR, it is inferred that jarosite and sulfates are the products of the acid leaching, and goethite and dihydrate gypsum are the products of neutralization and precipitation of the leaching substrate. However, the presence of clay-

like minerals, gypsum, and iron phase contributes to the high-water absorption of EMR. In addition, it has been noted that part of the water exists in the fine capillary dissolution pores of EMR, and the traditional drying temperature failed to evaporate this part of the moisture (He et al., 2021c). This may also be an essential contribution to the high viscosity and high-water absorption of EMR.

Fig. 4 shows that R-EMR^{HSI} has seven obvious endothermic peaks at 72, 145, 260, 500, 860, 946, and 1030 ℃. The total mass loss of R-EMR^{HSI} was 25.4 % within the range of 35~1050 ℃. Combined with the setting calcination temperature, the whole calcination can be divided into five stages.

The first stage (0-200 ℃): the two endothermic peaks at 72 ℃ and 145 ℃ in this stage are mainly caused by the desorption of adsorbed water in EMR particles and the removal of crystal water from the dihydrate gypsum, with a mass loss rate of 5.5 %.

The second stage (200-400 °C): further dehydration of the hemihydrate gypsum and the precipitation of ferric sulfate from heat-hydroxyl dehydration of jarosite, which is also the main reason for the heat absorption peaks at 260°C. In addition, the small troughs ranging from 260 to 400°C validate the continued progress. The overall mass loss at this stage reached 4.65 %. Thus, the dehydration effect occurs mainly in EMR below 400 ℃, where the total amount of adsorbed water, crystal water and hydroxyl dehydration are about 10.17 %.

The third stage (400-600 ℃): thermal decomposition of ferric sulfate to generate hematite and the escape of gases from the thermal decomposition of ammonium sulfate, and the overall mass loss in this stage about 6.23 %. The fourth stage (600-800 °C): the activation of alumino-silica minerals and the continuous decomposition of gypsum to increase active ingredients in the system. Although there is no obvious endothermic peak in this stage, the restructuration, recrystallization and amorphization of minerals are continuously proceeding, which is reflected in the subsequent activity test results and other results. It is precisely due to the small fluctuation of chemical composition that the overall mass

loss in this stage is 2.22 %.

The fifth stage (800-1000 °C): the muscovite mineral decomposed as the temperature increases, which was verified by the endothermic peak at 860 °C. The decomposition, recrystallization and amorphization of silica-alumina and sulfate minerals in EMR could be obtained from the two heat endothermic peaks at 946 and 1030 °C with the re-escalation of temperature. At this stage, the overall mass loss was 6.77 % due to the dehydration formation of type II anhydrite, sulfate decomposition and mineral activation.

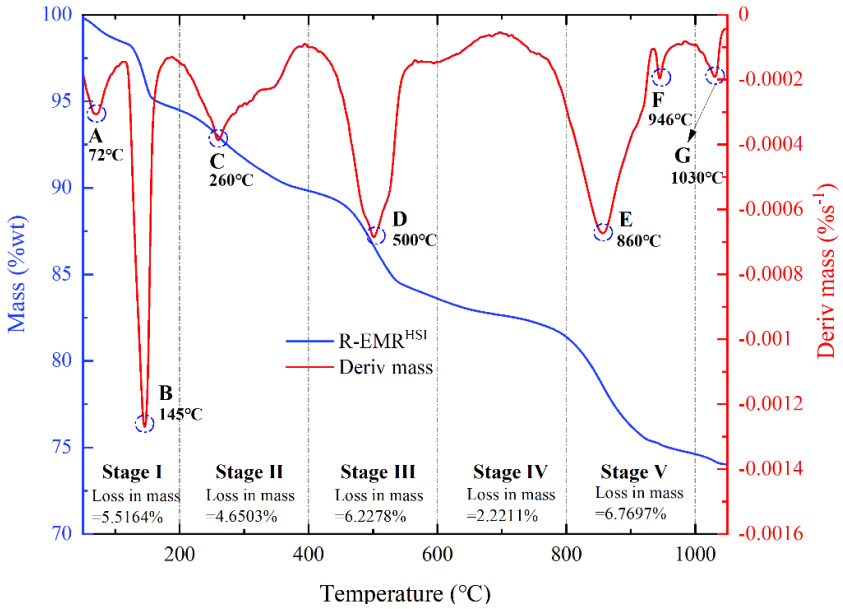

Fig. 4. The TG-DTG diagram of R-EMR^{HSI} (A, B stand for Mineral phase [$CaSO_4 \cdot 2H_2O$] dehydration; C represents mineral phase jarosite and $CaSO_4 \cdot 2H_2O$ dehydration and recrystallization; D shows Kaolinite mineral phase dehydrate activation and gas spillage; E expresses muscovite decomposition and mineral amorphization; F and G signify mineral decomposition, recrystallization and amorphization).

3.2 Physicochemical characteristics of C-EMR^{HSI}

The physicochemical properties of C-EMR^{HSI} via various calcination are exhibited in **Table 4**. The dominant oxides present in the C-EMR^{HSI} consisting of SiO_2, Al_2O_3, CaO, Fe_2O_3, SO_3 and MgO,

which express a close commonality with R-EMR^{HSI} (**Table 2**). However, the oxides proportions of C-EMR^{HSI} varied slightly under different calcination.

Table 4 depicts the main compositions of C-EMR^{HSI} kept basically stable under the calcination from 200 ℃ to 1000 ℃. It is noted that the sulfates are emitted in gaseous form (SO_3) as the increasing calcination temperature, which is attributed to the decomposition of sulfates in the EMR. The reduction of SO_3 can affect the variation in other oxides content.

More specifically, oxides such as SiO_2, Al_2O_3, CaO and Fe_2O_3 slightly increased with the increase of temperature. Other oxides have been tested without large fluctuations because of the low initial content. The loss on ignition (LOI) diminishes with increasing temperature and reaches up to 20.6%. In contrast to blast furnace slag, the production of EMR with a hydrometallurgical process results in a high LOI due to the absence of a precalcination at high temperatures (He et al., 2021a).

Table 4 also exhibits that the amorphous phase of C-EMR^{HSI} increased with the increasing calcining temperature. The maximum amorphous phase content was 42.18% at 800 ℃, which implied that the high temperature has a significantly activation on the pozzolanic activity of EMR and the optimal calcined temperature was of 800 ℃.

The density, particle size, BET surface area and water absorption of EMR after different calcination temperatures are shown in **Table 4**. The density of EMR increased with the increase of temperature. The particle size of calcined EMR increases continuously with density, while the opposite trend of surface area in the calcined EMR. The open pores of EMR particles are gradually closed with the increase of temperature. The unit water demand increases and then decreases with the increase of temperature, which is related to the transformation of the gypsum. In conclusion, the physicochemical properties of EMR are related to the mineral decomposition, reconstruction and crystal transformation.

Table 4. Physicochemical properties of C-EMR^{HSI}

Samples	C-EMR$^{HSI}_{200}$	C-EMR$^{HSI}_{400}$	C-EMR$^{HSI}_{600}$	C-EMR$^{HSI}_{800}$	C-EMR$^{HSI}_{1000}$
	Chemical analysis (% by mass)				
SiO_2	36.87	37.04	38.22	38.58	40.68
Al_2O_3	8.22	8.00	8.65	9.26	9.05
CaO	5.921	5.581	5.924	6.383	6.646
Fe_2O_3	21.8	21.86	22.33	23.31	24.92
SO_3	19.14	20.75	16.79	15.11	10.26
MgO	0.604	0.572	0.618	0.495	0.639
MnO	4.555	4.286	4.531	3.825	4.493
Na_2O	0.372	0.313	0.34	0.327	0.362
K_2O	1.41	1.32	1.44	1.48	1.57
TiO_2	0.252	0.238	0.249	0.265	0.281
P_2O_5	0.376	0.365	0.441	0.508	0.587
Amorphous phase	23.15	27.33	34.12	42.18	41.26
LOI	3.09	5.82	8.86	13.05	20.6
Property	Physical characteristics				
Density (g/cm^3)	2.915	2.924	2.931	2.937	2.945
D50 (μm)	12.83	13.51	13.92	14.25	14.94
BET surface area (m^2/g)	5.6327	3.8751	3.7114	2.8251	2.5671
Water absorption (g/g)	3.15	3.52	3.73	2.02	1.75

The apparent morphological of EMR at different calcination temperatures is exhibited in **Fig. 5**. As can be seen, the EMR gradually turns red in color at 0-400°C, mainly due to the increase in the goethite. In 400-600 ℃, EMR with light-red is deepened and converted to red because of hematite in large amount. When calcined to 800 ℃, there is a light sintering agglomeration and the EMR exhibits the dark-brown in color. At 1000 ℃, EMR transforms to black due to the presence of large amount of

Mn_3O_4 and iron oxide.

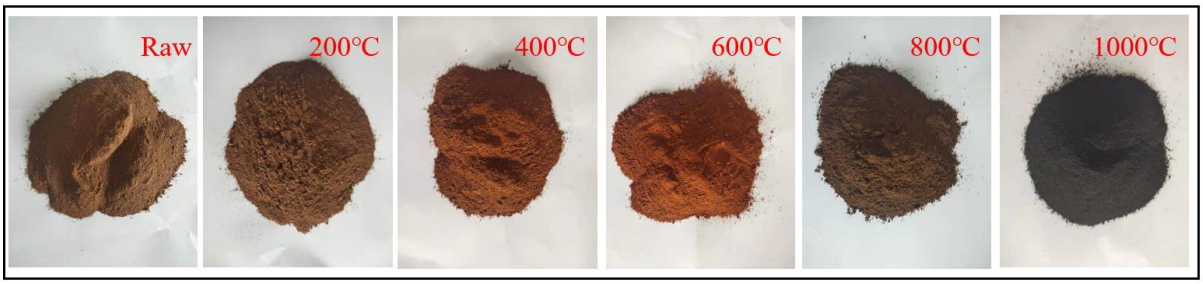

Fig. 5. Apparent morphology of the calcined EMR^{HSI}.

3.3 The transformation of the mineral composition of C-EMR^{HSI}

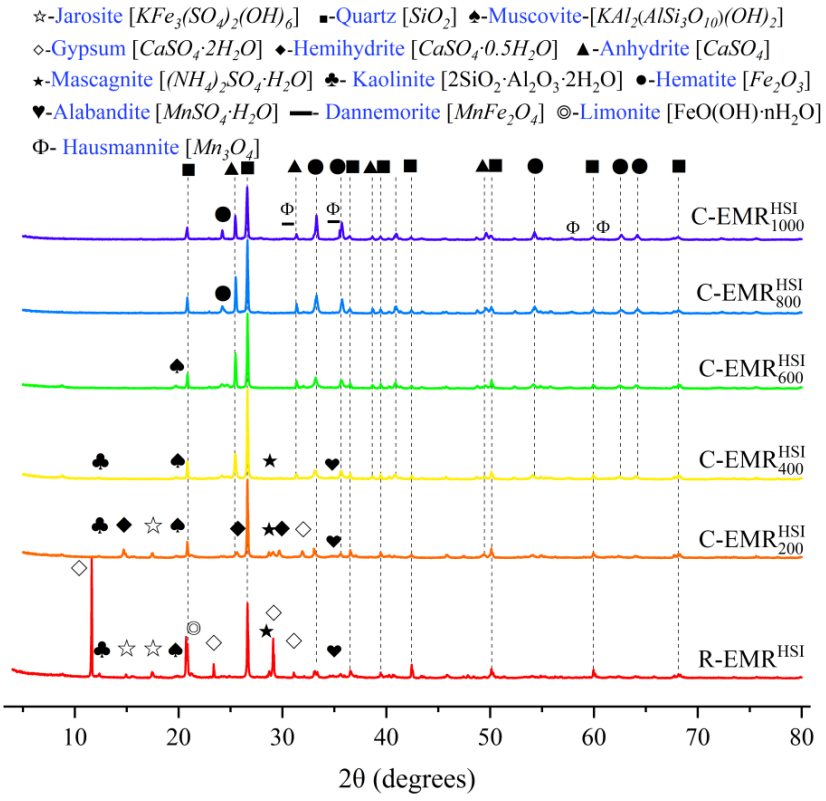

Fig. 6. The mineralogical compositions of the R-EMR^{HSI}.

The mineral compositions of C-EMR^{HSI} were identified by XRD results, as exhibited in **Fig.6**. And TG-DTG results of the calcined samples after experiencing the setting calcination temperature treatment are shown in **Fig. S2**.

3.3.1 Effect of calcination on gypsum phase

Combining the results in **Figs. 4**, **6** and **S2**, the stepwise dehydration of dihydrate gypsum to anhydrous gypsum phase as the rising calcination temperature. Specifically, when the calcination temperature below 200 °C, all crystalline water in the gypsum phase was firstly eliminated. When the calcination temperature exceeds 200 °C, the diffraction peaks disappear at 14.7 º, 25.7 º, 29.7 º and 31.9 º (2θ), indicating the continued dehydration of hemihydrate gypsum. With increasing the temperature below 800 °C, the diffraction peaks progressively strengthen at 25.5 º, 31.4 º and 40.9 º (2θ), showing the decomposition of anhydrous gypsum. Then, the anhydrous gypsum (Type Ⅱ) diffraction peak weakens gradually, which is associated with the inclusion of fused and glassy quartz phases in the EMR. The chemical formulae of the calcined reactions of the gypsum phase are shown in **equations (2)** to **(5)** and **Fig. S3**.

$$2CaSO_4 \cdot 2H_2O \xrightarrow{0\sim200℃} 2CaSO_4 \cdot 0.5H_2O(\beta) + 3H_2O \quad (2)$$

$$2CaSO_4 \cdot 0.5H_2O \xrightarrow{200\sim400℃} 2CaSO_4(\beta) + H_2O \quad (3)$$

$$2CaSO_4(\beta) \xrightarrow{400\sim800℃} CaSO_4(\text{II}) + CaO + SO_3 \quad (4)$$

$$2CaSO_4(\text{II}) \xrightarrow{>900℃} CaSO_4(\text{I}) + CaO + SO_3 \quad (5)$$

3.3.2 Effect of calcination on the iron phase

From Figs.**4, 6** and **S2**, it can be seen that the dehydration of limonite is intensified with the increase of calcination temperature, and recrystallizes to hematite (after 200°C). The newly-presented diffraction peaks about hematite at 33.2° and 35.6° (2θ) all verify this process. In addition, the jarosite is decomposed into sulfates and ferric oxide below 400°C. Then, further decomposition and recrystallization occurred to form hematite. The whole process is shown in **equation (6)**.

$$2KFe_3(SO_4)_2(OH)_6 \xrightarrow{0\sim400℃} 3Fe_2O_3 + K_2SO_4 + 3H_2SO_4 + 3H_2O \quad (6)$$

3.3.3 Effect of calcination on the silica-alumina phase

The diffraction peak intensity of quartz in EMR gradually weakens with the increase of calcination temperature. It speculates that the quartz phase increasingly becomes amorphous and fuse with other metal elements to form glassy silicate within this thermo-range. When the calcination temperature exceeds 500°C, kaolinite first undergoes dehydration and followed by gradually dihydroxylation (Zhou et al., 2021). It is noted that kaolinite is decomposed into active silica and amorphous alumina with low crystallinity and hydration and gelling properties (**eq. (7)**). When the temperature rises to 800 °C, muscovite is significantly enhanced by thermal decomposition into siliceous or silicon-alumina amorphous phases (**eq. (8)**).

$$Al_2(Si_2O_5)(OH)_4 \xrightarrow{400\sim600℃} Al_2O_3 \cdot 2SiO_2 + 2H_2O \quad (7)$$

$$KAl_2(AlSi_3O_{10})(OH)_2 + SiO_2 \xrightarrow{800℃} KAlSi_3O_8 + Al_2SiO_5 + H_2O \quad (8)$$

3.3.4 Effect of calcination on harmful components

NH_4^+-N and Mn^{2+} are the main contaminants in EMR. In the production of manganese ore, ammonia is introduced to neutralize the leachate to form ammonium sulfate. In contrast, the two ore one-step method is adopted due to the decrease in ore grade, which changes the procedure while reduces the introduction of NH_4^+-N. As a result, the characteristic diffraction peak of ammonium sulfate (28.5 °) is not obvious in the XRD results. **Fig.6** shows that the characteristic diffraction peak of ammonium sulfate gradually weakens between 200-400 °C and disappears in the diffraction pattern at 600 °C, indicating that ammonium sulfate escapes as a gas between 400-600 °C. Meanwhile, part of sulfate also partially escaped as gas during the temperature-rise period (above 800 °C). The chemical reactions are shown in **equations (9)** and **(10).**

$$(NH_4)_2SO_4 \cdot H_2O \xrightarrow{200\sim400℃} (NH_4)_2SO_4 + H_2O \quad (9)$$

$$3(NH_4)_2SO_4 \xrightarrow{>400℃} 4NH_3 + N_2 + 3SO_2 + 6H_2O \quad (10)$$

The residual manganese in the EMR is mainly in the form of manganese sulfate and manganese

oxides, which causes the low crystallinity of manganese in the EMR. The manganese sulfate is mainly dehydrated and decomposed at 800 °C to form Mn_2O_3 (**eq. (11-12)**). The part of the manganese sulfate gradually converted into Mn_3O_4 with the calcination temperature higher than 800 °C (**eq. (13)**). The Mn-hercynite compound is formed by calcining Fe_2O_3 and Mn_3O_4 formed as the temperature exceeds 900 °C (**eq. (14)**).

$$MnSO_4 \cdot H_2O \xrightarrow{100\sim600℃} MnSO_4 + H_2O \quad (11)$$

$$2MnSO_4 \xrightarrow{>600℃} Mn_2O_3 + SO_2 + SO_3 \quad (12)$$

$$6Mn_2O_3 \xrightarrow{>800℃} 4Mn_3O_4 + O_2 \quad (13)$$

$$Fe_2O_3 + Mn_3O_4 \xrightarrow{900\sim1000℃} MnFe_2O_4 + Mn_2O_3 \quad (14)$$

The mass loss of the EMR prepared at different calcination temperatures are shown in **Table 5**. The overall mass loss decreases with increasing temperature, which is attributed to the reduction in mass due to dehydration, decomposition, amorphization and podzolization. Specifically, the overall mass loss of EMR is reduced by 3.91%, 6.60%, 3.94%, 3.59% and 5.34% after calcination at 200, 400, 600, 800 and 1000°C, respectively. The water stores between the pores in the porous fineness slag caused by sulfuric-acid leaching, which requires the continuous calcination to achieve complete dehydration (Wang et al., 2020). The TG curves of the calcined EMR are consistent with the analysis in **Fig. 4**, all detailed data are shown in **Fig. S2**.

Table 5. The loss in mass of $R\text{-}EMR^{HSI}$ and $C\text{-}EMR^{HSI}_{200\sim1000}$ at different temperature stages

Sample	Loss in mass (%)					$\sum$ Stage (I~V) Loss in mass
	Stage Ⅰ 35-200℃	Stage Ⅱ 200-400℃	Stage Ⅲ 400-600℃	Stage Ⅳ 600-800℃	Stage Ⅴ 800-1000℃	
$R\text{-}EMR^{HSI}$	5.5164	4.6503	6.2278	2.2211	6.7697	25.3853
$C\text{-}EMR^{HSI}_{200}$	1.2893	3.1128	7.5591	2.4491	7.0693	21.4796
$C\text{-}EMR^{HSI}_{400}$	0.4536	0.2390	1.6875	8.8236	3.0756	14.8793
$C\text{-}EMR^{HSI}_{600}$	0.5614	0.1451	0.2596	5.0881	4.8822	10.9364
$C\text{-}EMR^{HSI}_{800}$	0.2323	0.0425	0.0340	1.8411	5.2005	7.3504

C-EMR$^{HSI}_{1000}$	0.023	0.0066	0.0132	0.0494	1.9138	2.006

In conclusion, the increase in temperature on the one hand facilitates the resourceful recovery of valuable elements. On the other hand, the increase in the content of amorphous substances via calcination is accompanied by dehydration and recrystallization of hydrated minerals into high-activity states. In addition, increasing temperature promotes the aluminosilicate activation and sulfate decomposition, which increase alkalinity and reduces hazardous elements. Thus, the thermodynamic treatment has significant advantages for the resourceful and harmless treatment of EMR.

3.4 Pozzolanic activity of C-EMR^{HSI}

In order to find an optimal calcination temperature for EMR with good pozzolanic activity and compressive strength, the compressive strength of the EMR-blended mortar was tested at 3, 14, 28, 60 and 90 days. The results of SAI test in mortar with 30% EMR at different calcination temperatures are shown in **Table 6**. The control sample with 100% cement was set for comparative analysis. In general, a sample with a SAI of 75% at 28 days is considered as a standard pozzolanic material. The 28-day SAI of the EMR-blended mortar calcining at 200, 800 and 1000 °C all exceeded 75%, in particular the maximum SAI at 800 °C was 84.79%. Therefore, the EMR calcined at 200, 800 and 1000 °C can be classified as a high pozzolanic activity material. In addition, the SAI of all samples increased with the curing age, in which the highest SAI at 800 °C was 87.96%. The reasons for these phenomena are closely related to the evolution of the mineral phases (He et al., 2021c; Zhou et al., 2021).

Table 6. Compressive strength and SAI of EMR-blended mortar

Samples	3 days		14 days		28 days		60 days		90 days	
	CS (MPa)	SAI (%)	CS (MPa)	SAI (%)	CS (MPa)	SAI (%)	CS (MPa)	SAI (%)	CS (MPa)	SAI (%)
PC	16.20	100.00	33.65	100.00	40.75	100.00	44.31	100.00	47.01	100.00
R-EMR^{HSI}	8.50	52.47	22.10	65.68	28.05	68.83	31.52	71.14	33.92	72.15
C-EMR$^{HSI}_{200}$	9.70	59.87	24.81	73.72	30.16	74.01	34.30	77.41	36.78	78.24
C-EMR$^{HSI}_{400}$	6.20	38.27	19.15	56.91	23.80	58.40	27.15	61.27	29.45	62.65
C-EMR$^{HSI}_{600}$	2.55	15.74	17.50	52.01	21.95	53.87	24.75	55.86	27.82	59.18
C-EMR$^{HSI}_{800}$	9.95	61.42	24.95	74.15	34.55	84.79	37.85	85.42	41.35	87.96
C-EMR$^{HSI}_{1000}$	9.75	60.19	23.71	70.46	30.91	75.85	34.33	77.48	39.45	83.92

In early hydration, EMR has a significant retardation on cement hydration due to the presence of gypsum. Thus, the SAI values of all EMR-blended mortar specimens are below 75%. The hemihydrate gypsum phase formed at 160 °C could improve the reactivity of EMR (Zhou et al., 2021). However, the hemihydrate gypsum phase continues to dehydrate with increasing temperature to form a poorly crystalline β-type gypsum phase, which reduces the pozzolanic activity of EMR. Meanwhile, the decomposition of other mineral phases and gas evaporites synergistically builds a porous EMR microstructure, which significantly increases the water absorption of EMR, especially at 400°C and 600°C. It means that the actual water-cement ratio of the mortar decreases and then reduces the fluidity of the mortar and is not conducive to the development of strength. Although kaolinite is dehydrated and decomposed in the range of 400-600°C to form the silica-alumina phase, but the low temperature silica and amorphous aluminum phase formed at this stage do not contribute significantly to the strength development (**Figs. 6** and **S2**). With the increase of calcination temperature, the gypsum phase is thermally decomposed to increase the active calcium oxide content, and the existing silica-alumina phase is activated to form amorphous silica-alumina material. However, the pozzolanic

activity of EMR calcined at 1000 °C is reduced due to recrystallization of amorphous minerals and the massive formation of Mn_3O_4, which also caused a slight decrease in SAI.

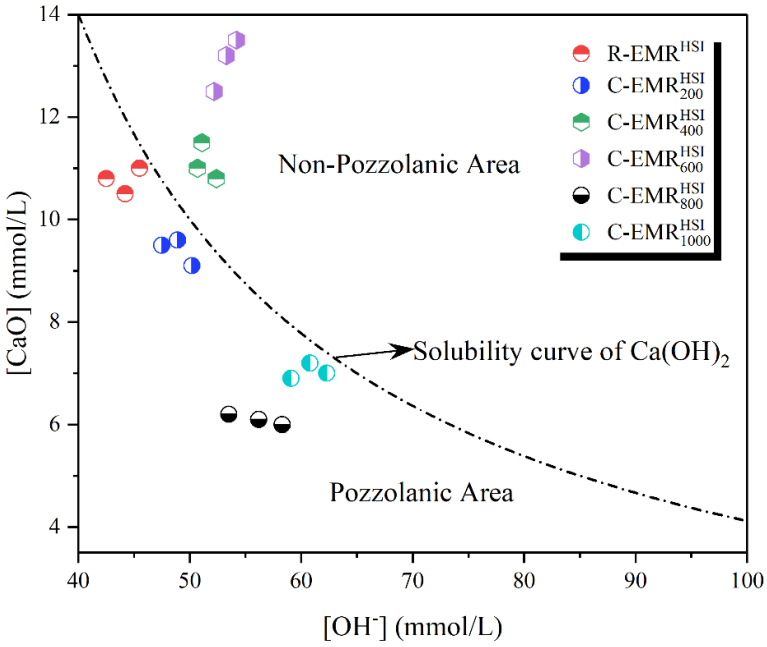

Fig. 7. Frattini test results for EMR with different calcination temperatures after curing at 40°C for 8 days.

Fig. 7 shows the results of the Frattini test for EMR replacing 30% cement blended paste. In the range of 35 and 90 mmol/L [OH], the theoretical maximum [CaO] concentration can be calculated using the equation given in EN 196-5 to plot the $Ca(OH)_2$ solubility curve at 40 ℃,

$$\text{Max[CaO]} = \frac{350}{\text{[OH]-15}} \quad (15)$$

Fig. 7 shows that the positions of R-EMR^{HSI}, C-EMR$^{HSI}_{400}$ and C-EMR$^{HSI}_{600}$ are on the $Ca(OH)_2$ solubility isotherm and this region is defined as the range of non-pozzolanic activity. Test samples within this range lacked qualifying pozzolanic activity. For C-EMR$^{HSI}_{200}$, C-EMR$^{HSI}_{800}$ and C-EMR$^{HSI}_{1000}$, the test results all lie below the calibration line, indicating that the samples have a good pozzolanic activity. In particular, when the calcination temperature is increased to 800 °C, the [CaO] and [OH^-] positions of the tested samples were far below the $Ca(OH)_2$ solubility isotherm. It indicates that the Ca^{2+} and OH^- released by cement hydration are consumed by the pozzolanic reaction of EMR.

Therefore, the EMR calcined at 800°C can be considered as a high pozzolanic activity material, which is consistent with the SAI test results.

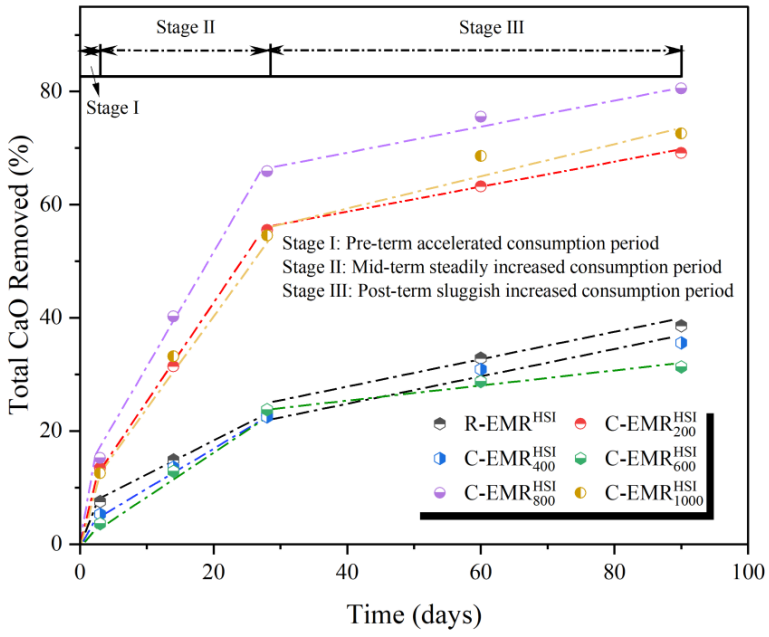

Fig. 8. Results of SL tests with EMR at different calcination temperatures in sealed plastic bottles at 40 °C after 3, 14, 28, 60 and 90 days.

Fig. 8 shows the consumption of saturated lime with EMR after different calcination temperatures. The results can be divided into three stages based on the consumption rate of saturated lime, which are the pre-term accelerated consumption period, mid-term steadily increased consumption period and post-term sluggish increased consumption period. All samples exhibit a rapid lime consumption over 3 days. Specifically, the total lime consumption of the $C\text{-}EMR^{HSI}_{800}$ was 65.87% at 28 days. It is noted that the sample had a lime consumption rate of 0.21% per hour for the first 3 days and an overall lime consumption rate of approximately 0.1% per hour by 28 days, which slowed down again with longer curing age. This is consistent with the SAI results, which reached a value of 84.79% at 28 days. In addition, the calcined samples with high SAI exhibit a greater amount of lime consumption

compared to the samples with low SAI. Overall, lime consumption tests occurred at an accelerated rate during the first 3 days curing age and were essentially complete during the 28 days curing age.

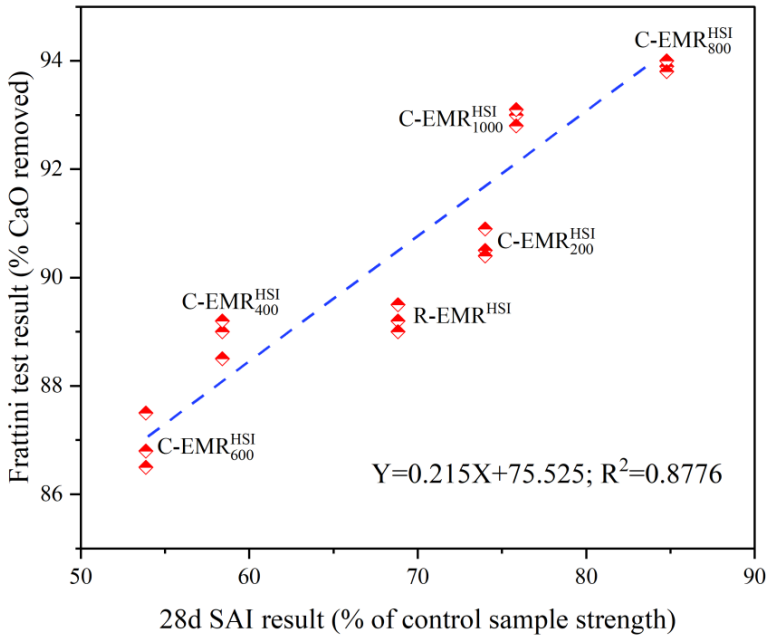

Fig. 9. Correlation between Frattini test and 28-d SAI of EMR at different calcination temperatures.

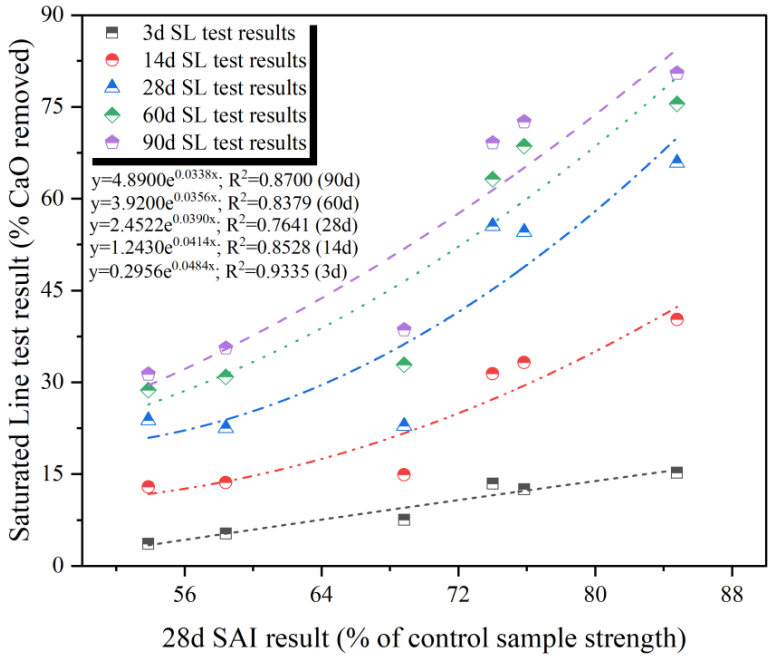

Fig. 10. Correlation between result of 28-d SAI and SL tests (3, 14, 28, 60 and 90 days).

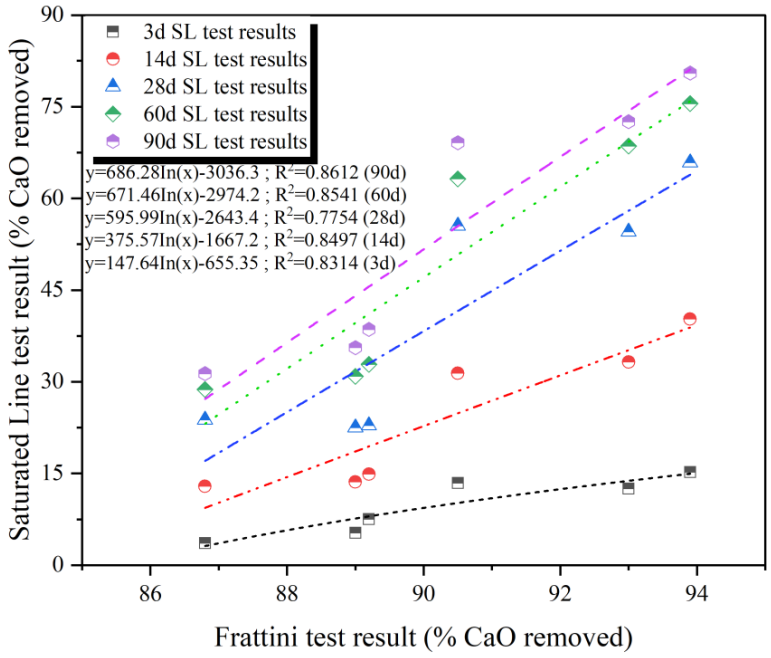

Fig. 11. Correlation results of the 8-d Frattini test and SL tests (3, 14, 28, 60 and 90 days)

Based on **Figs. 9-11**, there is a significant correlation between the SAI results and the Frattini test results (R^2 = 0.8776). In contrast, although Frattini test and SL test, SA1 test and SL test also have a good correlation, the test conditions and errors lead to poor stability. It may be that the mass ratio of lime to EMR formed by mixing 7 g cement with 3 g EMR in the Frattini and SAI tests is much lower than the ratio formed by mixing 1 g of EMR with 75 ml of saturated lime solution in the SL test.

Due to the lower ratio of lime to EMR, the SL test exhibits a higher pozzolanic activity compared to the Frattini test. In addition, unlike the SAI and Frattini tests, where there is no cement and no bulk solid phase is formed because the SL test uses a different system. Further, a small amount of solid $Ca(OH)_2$ passing through the filter has greater buffers in the titration and introduces large errors. Also, previous studies indicated that the SAI test was performed at 23°C for 28 days, while the Frattini test was conducted at 40°C for 8 days (Tironi et al., 2013).

3.5 Effect of calcined EMR on cement hydration

3.5.1 Hydration kinetics

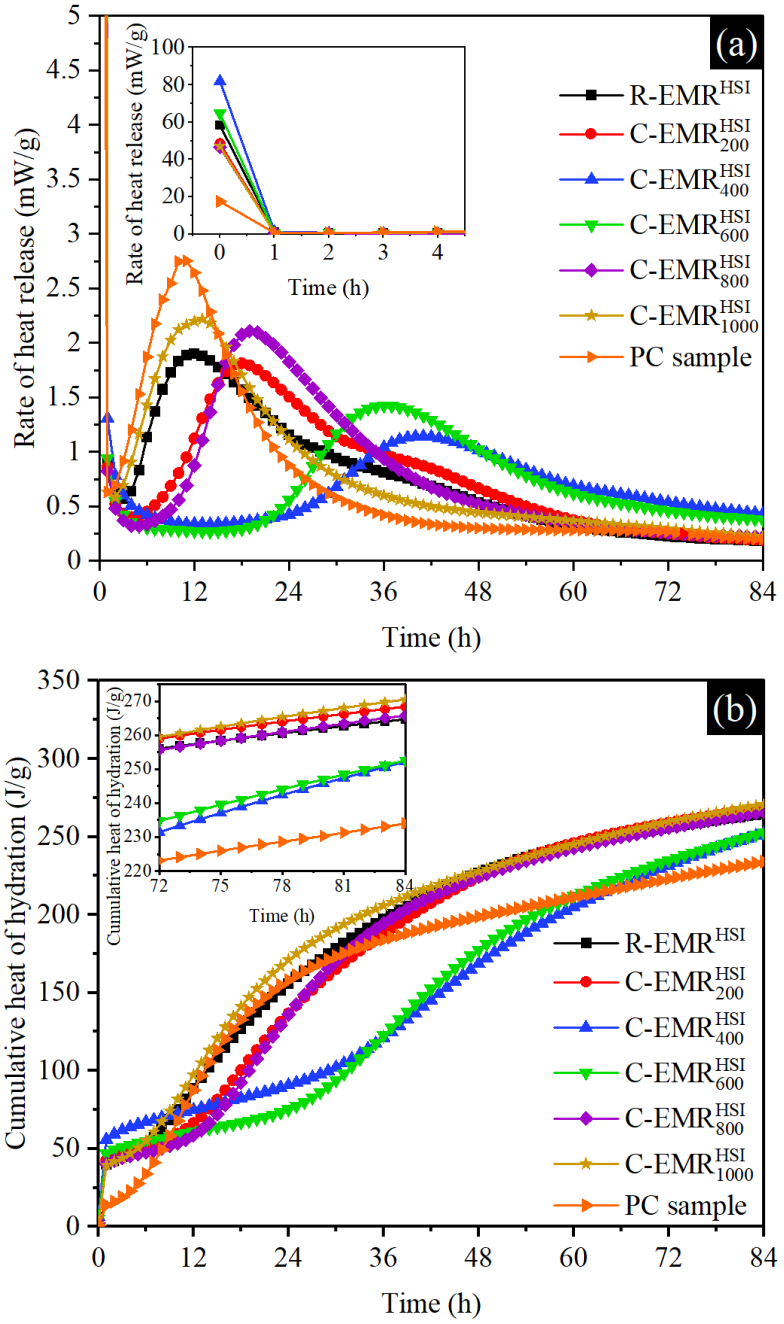

Fig. 12. Exothermic hydration of the EMR-blended slurry (a) rate of heat release (b) cumulative heat of hydration

The results of the exothermic heat of hydration of the slurry mixed with calcined EMR are shown

500 in **Fig. 12**. The results of setting time and soundness of cement and EMR-blended mortar are
501 presented in Table S1. The mixture consisting of 30% EMR to 70% cement with a water/binder ratio
502 of 0.5 was analyzed in-depth. **Fig. 12** shows that the hydration exothermic peaks of EMR at
503 calcinations of 400 and 600 °C are shifted to the right with various degrees, implying that the addition
504 of EMR is able to retard the hydration process (Table S1). Compared with previous PC results, the
505 addition of EMR reduces the intensity of hydration exothermic peak, especially in the slurry prepared
506 by EMR calcined at 400 °C and 600 °C (He et al, 2021c). The retardation of cement hydration is
507 attributed to two possible reasons: one aspect is the synergistic contribution of the high-water
508 absorption of EMR particles with dissolved sulfate ions (Zhou et al., 2021). The majority of the water
509 are first absorbed by the calcined EMR particles while much less water is used for the cement
510 hydration than for the stoichiometry. On the other hand, a large amount of sulfate ions dissolved in
511 the slurry reacts with calcium and aluminum phase to form hydration products, which adsorb on the
512 surface of the cement particles. It retards the dissolution of cement particles and inhibits the growth
513 of crystals (Wang et al., 2013; Xu et al., 2019).
514 The exothermic peak of hydration of samples mixed with $C\text{-}EMR^{HSI}_{800}$ and $C\text{-}EMR^{HSI}_{1000}$ is much
515 higher than the other samples, which can be considered that the calcined EMR promotes the hydration
516 reaction. The cumulative heat of hydration of slurry mixed with $C\text{-}EMR^{HSI}_{800}$ and $C\text{-}EMR^{HSI}_{1000}$ was
517 265 J/g and 269.7 J/g for 84 h, respectively. It also confirms that the activation of EMR on cement
518 components, such as C_3A (Xu et al., 2019). The exothermic peak of hydration of the slurry mixed
519 with $C\text{-}EMR^{HSI}_{200}$ and $R\text{-}EMR^{HSI}$ is lower than that with $C\text{-}EMR^{HSI}_{800}$ and $C\text{-}EMR^{HSI}_{1000}$, but
520 higher than that with $C\text{-}EMR^{HSI}_{400}$ and $C\text{-}EMR^{HSI}_{600}$, which is also closely related to the
521 transformation of the gypsum and the formation of amorphous activated substance. The existing
522 studies indicated that the calcined EMR at 160 ℃ has a high reactivity due to the presence of the

hemihydrate gypsum phase. On the other hand, calcination above 360 ℃ decreases the reactivity of EMR while increasing its water absorption due to the generation of low-activity anhydrous gypsum.

3.5.2 Analysis of hydration products

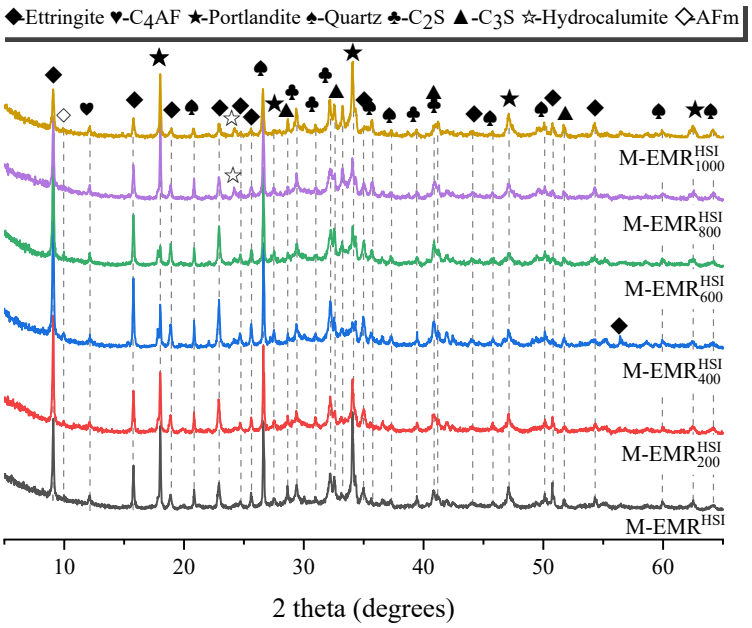

Fig. 13. XRD patterns of EMR-blended mortar curing at 28 days.

Fig. 13 shows results of hydration products of the mixed mortar prepared by EMR at different calcination temperatures after curing for 28 days. The main hydration product phases of the EMR blended mortar were ettringite, AFm (monosulfate), hemi-sulfate and common cement hydration products. **Fig. 13** exhibits that the calcium alumina phase is present in large amounts in the hydration products of mortar. The mortar formed by $C\text{-}EMR_{200}^{HSI}$, $C\text{-}EMR_{400}^{HSI}$ and $C\text{-}EMR_{600}^{HSI}$ produce large amounts of ettringite due to the large amount of gypsum with high temperature transformation. Meanwhile, the formation of aluminate phase may be provided by the high temperature calcination of EMR. **Fig. 13** also shows that the diffraction peak intensity of ettringite increases and then decreases with increasing calcination temperature. In contrast, the diffraction peak of portlandite decreases and then increases with increasing calcination temperature. The mixed mortar prepared by

539 EMR calcined at 400 and 600 ℃ produces a large amount of calcium alumite and a small number of
540 portlandite. By contrast, the blended mortar prepared by EMR calcined at 800 and 1000 ℃ formed
541 less ettringite and aluminate phases and more portlandite. It is closely related to the high temperature
542 transformation of the gypsum and aluminosilicate phases in the EMR.

543 3.5.3 Microstructure analysis

544 **Fig. 14** shows the SEM images of the 30% EMR-blended mortar after 28 days of curing. In mortar
545 with 70% PC, portlandite with good crystallinity layered is produced to form a dense structure, and
546 C-S-H gels formed by hydration are interspersed with needle-like ettringite. With the addition of
547 EMR, more discernible pores are observed in the ENR-blended mortar, resulting in a loose
548 microstructure. These pores not filled by hydration products can adversely affect the mechanical
549 properties of the mortar. In addition, a large number of ettringite occurred in $R\text{-}EMR^{HSI}$,
550 $C\text{-}EMR^{HSI}_{200}$, $C\text{-}EMR^{HSI}_{400}$ and $C\text{-}EMR^{HSI}_{600}$ samples due to the presence of gypsum phases. There are
551 significant differences in the morphology of ettringite produced by different gypsum phases.
552 Especially for the mortar blended with $C\text{-}EMR^{HSI}_{400}$ and $C\text{-}EMR^{HSI}_{600}$, a large amount of needle-like
553 ettringite fills the microstructure of the mortar, forming a large number of pores structure. It also
554 verifies the reason for the poor mechanical properties of the mortar blended with $C\text{-}EMR^{HSI}_{400}$ and
555 $C\text{-}EMR^{HSI}_{600}$. The AFm phase with hexagonal lamellar crystals and a large amount of portlandite were
556 found in the mortar blended with $C\text{-}EMR^{HSI}_{800}$ and $C\text{-}EMR^{HSI}_{1000}$. The SEM images of mortar mixed
557 with $C\text{-}EMR^{HSI}_{800}$ and $C\text{-}EMR^{HSI}_{1000}$ exhibit that the short rod-like and vermiculite-like C-S-H gels
558 are formed due to the introduction of additional Si and Al elements from EMR, which reduces the
559 Ca/Si ratio of the gels. However, C-S-H gels with different morphology can not be considered as the
560 products of hydration or EMR-active reactions. The effect of EMR on calcium silicate hydrate gels,
561 including their composition and morphology, needs further investigation.

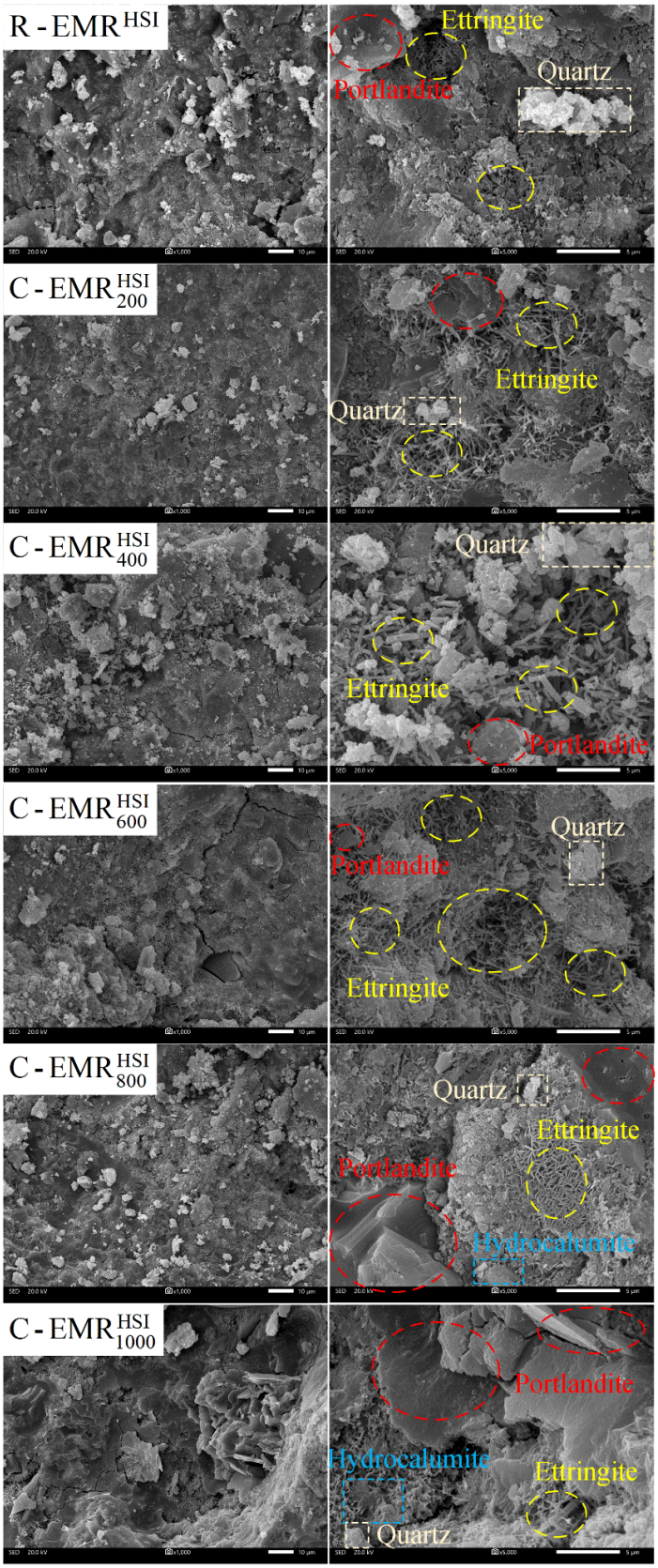

562

563 Fig. 14. SEM micrographs of pretreated EMR (0, 200, 400, 600, 800 and 1000 ℃) blend mortar.

564

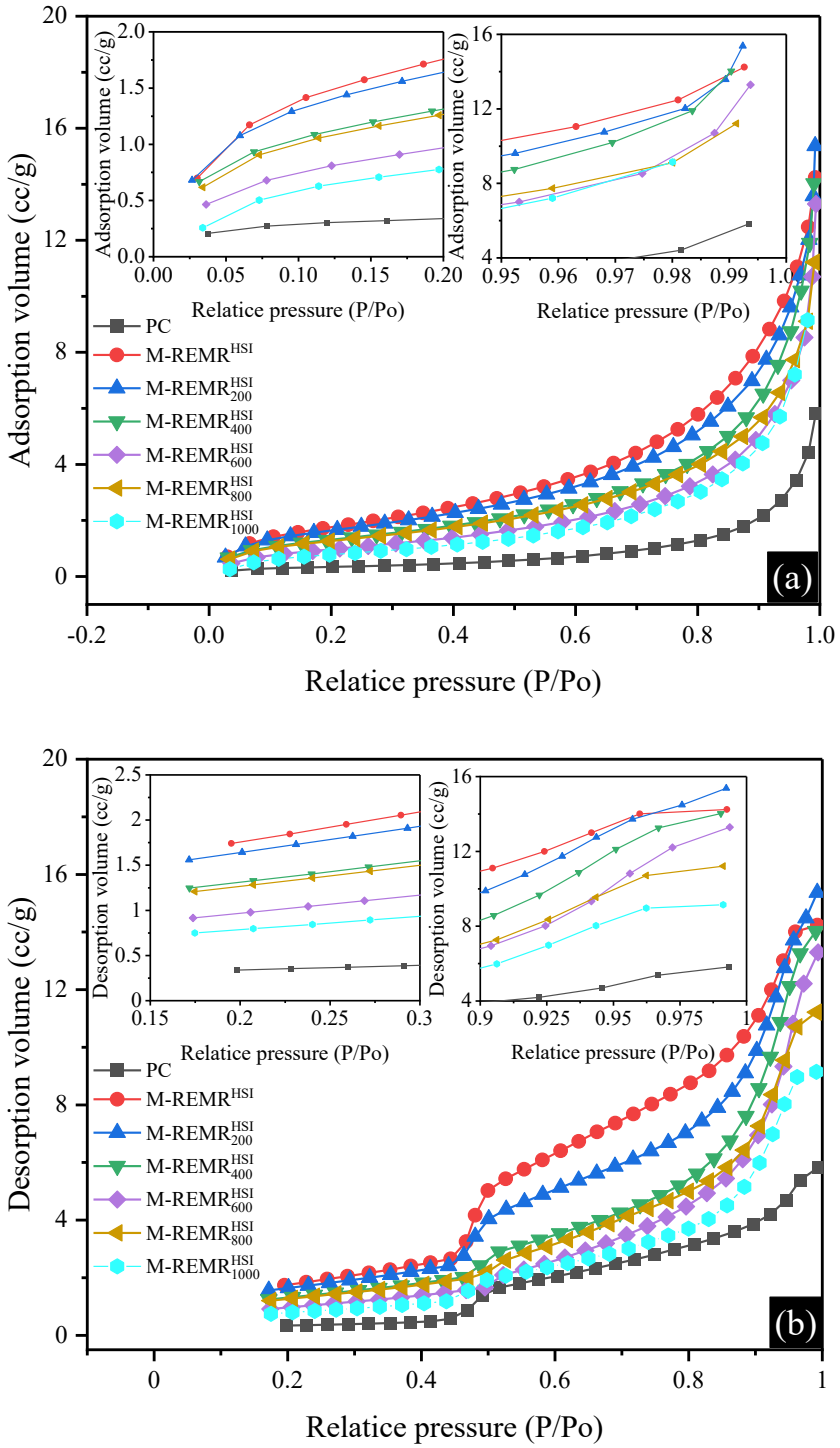

565

566

567 Fig. 15. Nitrogen adsorption isotherm patterns (a) adsorption curve and (b) desorption curve of EMR-blend

568 mortar.

569

570 Pore distribution of the EMR-blended mortar is shown in **Fig. 15**. All samples exhibited a hysteresis

571 effect, which indicates that the EMR-blended mortar is unevenly distributed and mostly large pores.

With the addition of EMR, the pore volume of EMR-blended mortar increases. It can be explained by the loose porous properties of EMR (Xu et al., 2013). In addition, the diversity of types and structures of hydration products in the presence of EMR leads to more pores in the mortar structure.

Fig. 15a indicates that the adsorption volume of the EMR-blended mortar decreases with the increase of calcination temperature, which indicates that calcination can reduce pore volume of the mortar. And the desorption curve in **Fig. 15b** exhibits that the desorption volume of the EMR-blended mortar shifts from type-H3 type to type-H4 as the calcination temperature increases. It implies the non-uniform slit-like pores in the mortar are transformed into homogeneous slit-like pores. The test result suggests that the macropores of mortar may be partially or fully filled by the hydration products of EMR. The results of the pore distribution are in agreement with the SAI results and further confirm the occurrence of EMR pozzolanic activity, which is beneficial for the strength development.

3.6 Leaching characteristics analysis

Heavy metal contaminants in EMR, such as Mn, Cr and Zn, are a matter of great concern when used in construction materials (Duan et al., 2011; Han et al., 2020; He et al., 2021b). To ensure the safety of EMR utilization, the toxicity characteristic leaching procedure (TCLP) was used to determine the leaching concentration of raw EMR, calcined EMR, and EMR-blended mortar.

The TCLP test results are shown in **Table 7**. It indicates that the leaching concentrations of heavy metals were well below the standard limits for all samples. In the EMR, the concentrations of Zn and Mn were higher than the other minor constituents. The direct utilization of EMR may bring contaminants into the finished product and cause secondary environmental pollution. After the pretreatment of calcination, the leaching concentration of heavy metal decreases with the increase of calcination temperature. The glassy and crystalline products produced during the calcination can

595 incorporate metal ions into the amorphous network and crystal structure, leading to the
596 immobilization of heavy metals (Shu et al., 2019a, 2020; Sun et al., 2020). In comparison with
597 calcined EMR, mortar containing 30% EMR exhibited a relatively low leaching concentration, except
598 for elemental Cr that may come from raw PC. In the mortar, heavy metals may be embedded in the
599 hydration products or form precipitates with other ions (Xu et al., 2019). In addition, the dense
600 structure of EMR-blended mortar prevents the leaching behavior of heavy metal. In conclusion, the
601 immobilization of heavy metals in the calcination process and in the mortar leaves no significant
602 concerns for the future utilization of EMR in building materials.
603
604 Table 7. Leaching concentrations of EMR-blended mortar using the TCLP

Sample	Concentration of heavy metals (mg/L)								
	Cr	Pb	As	Cu	Zn	Ba	Cd	Se	Ni
R-EMR^{HSI}	0.200	0.010	0.010	0.020	6.500	0.050	0.020	0.010	0.200
C-EMR$^{HSI}_{200}$	0.100	0.050	0.050	0.010	7.000	0.020	0.020	0.050	0.110
C-EMR$^{HSI}_{400}$	0.100	0.040	0.020	0.040	7.200	0.020	0.020	0.070	0.150
C-EMR$^{HSI}_{600}$	0.200	0.050	0.080	0.050	7.500	0.010	0.010	0.080	0.150
C-EMR$^{HSI}_{800}$	0.050	0.020	0.030	0.020	1.200	0.010	0.010	0.020	0.020
C-EMR$^{HSI}_{1000}$	0.002	0.010	0.010	0.010	0.500	0.010	0.010	0.020	0.010
M-REMR^{HSI}	0.002	0.002	0.001	0.005	1.200	0.005	0.002	0.020	0.010
M-CEMR$^{HSI}_{200}$	0.001	0.001	0.005	0.001	2.200	0.002	0.002	0.008	0.020
M-CEMR$^{HSI}_{400}$	0.001	0.002	0.002	0.004	2.700	0.001	0.002	0.008	0.010
M-CEMR$^{HSI}_{600}$	0.002	0.003	0.008	0.005	2.500	0.002	0.001	0.005	0.050
M-CEMR$^{HSI}_{800}$	0.001	ND	0.003	0.002	0.700	ND	0.001	0.001	0.050
M-CEMR$^{HSI}_{1000}$	ND	0.001	0.001	0.001	0.050	ND	0.001	ND	ND
PC	ND	0.004	0.001	0.003	ND	0.005	0.001	ND	ND
GB5085.3-2007	15.0	5.0	5.0	100.0	100.0	100.0	1.0	1.0	5.0
GB5085.3-1996	1.50	1.0	0.5	2.0	5.0	-	0.1	0.5	1.0

Note: ND: not detected.

In addition, the variations of soluble Mn^{2+} and NH_4^+-N content in EMR are also of interest. **Table 8** shows the leaching concentration of calcined EMR under different leaching conditions. It indicates that the leaching content of Mn^{2+} and NH_4^+-N at strong acid condition (pH=2.88) are higher than the weak acid conditions (pH=4.93 and 7). Under the strong acid condition (pH=2.88), the content of Mn^{2+} and NH_4^+-N in the raw material was 127.74 and 15.14 times higher than the standardized limits, while the content of Mn^{2+} and NH_4^+-N in the water leaching was 67.5 and 12.06 times higher than the standardized limits. After calcinating at 200, 400 and 600 ℃, the leaching of Mn^{2+} did not decrease significantly but increase due to the water loss. When the calcinating temperature exceeds 800 ℃, the Mn^{2+} is fixed in glass and crystals in the form of oxides, resulting in a significant decrease in the leaching value and complied with the standard limits (GB5085.3-1996; GB5085.3-2007). The content of NH_4^+-N escapes as a gas at temperatures above 280 °C. When the calcination temperature exceeds 600 °C, the emission of NH_4^+-N complies with the standard (GB5085.3-1996).

Table 8. Leaching concentrations of EMR using the TCLP

Samples	Acid (pH=2.88) leaching		Acid (pH=4.93) leaching		Water (Ph=7) leaching	
	Mn (mg/L)	NH_3-N (mg/L)	Mn (mg/L)	NH_3-N (mg/L)	Mn (mg/L)	NH_3-N (mg/L)
R-EMR^{HSI}	638.70	378.50	543.20	367.50	337.50	301.40
C-EMR$^{HSI}_{200}$	655.20	375.20	564.80	344.20	344.10	311.20
C-EMR$^{HSI}_{400}$	805.10	54.10	641.30	48.40	410.50	24.50
C-EMR$^{HSI}_{600}$	851.50	21.60	710.60	17.30	466.80	10.70
C-EMR$^{HSI}_{800}$	41.71	1.20	38.10	0.90	24.10	ND
C-EMR$^{HSI}_{1000}$	35.81	0.20	29.20	ND	18.70	ND

GB5085.3-1996	5.00	25.00	5.00	25.00	5.00	25.00

The results of the Mn^{2+} and NH_4^+-N in EMR-blended mortar at different curing ages are shown in **Table 9**. The 3-d leaching concentrations of Mn^{2+} and NH_4^+-N in mortar prepared by raw EMR and EMR calcined at 200 °C still exceeded standard limit. Meanwhile, the 3-d leaching of Mn^{2+} in the EMR-blended mortar mixed with the EMR calcined at 400 °C and 600 °C also exceeded the standard limits. As the continued cement hydration promotes the solidification of Mn^{2+} and the release of NH_4^+-N, all the specimens meet the standard limits after 28-d. The leaching of Mn^{2+} and NH_4^+-N of mortar formed by EMR calcined at temperatures above 800 °C for 3 d, 28 d and 90 d were all in accordance with the standard limits (GB5085.3-1996).

Table 9. Leaching concentrations of EMR mortar using the TCLP

Samples	3 days		28 days		90 days	
	Mn (mg/L)	NH_3-N (mg/L)	Mn (mg/L)	NH_3-N (mg/L)	Mn (mg/L)	NH_3-N (mg/L)
M-REMR^{HSI}	55.20	27.20	2.80	7.20	2.81	5.60
M-CEMR$^{HSI}_{200}$	62.50	25.50	3.20	5.20	3.11	5.10
M-CEMR$^{HSI}_{400}$	75.20	12.40	4.70	3.10	4.85	4.00
M-CEMR$^{HSI}_{600}$	80.10	8.70	4.20	2.00	4.66	3.20
M-CEMR$^{HSI}_{800}$	2.10	1.00	1.10	0.50	1.00	ND
M-CEMR$^{HSI}_{1000}$	0.50	0.10	0.20	ND	0.10	ND
GB5085.3-1996	5.00	25.00	5.00	25.00	5.00	25.00

4 Conclusion

The effects of calcination on the physicochemical properties and pozzolanic activity of EMR were investigated. In addition, the feasibility of EMR as a construction material was explored in terms of hydration kinetics, hydration phase, pore structure and leaching behavior. Based on the experimental

results, the following conclusions can be drawn:

(1) The mineral composition of raw EMR mainly includes jarosite, dihydrate gypsum, quartz, hematite, limonite, muscovite, and other sulfate-based dissolved materials. The high-water absorption of EMR is mainly associated with the gypsum and the formed porous structure after calcination. The density of EMR increases and the BET specific surface area decreases with the increase of calcination temperature, as the open pores of EMR particles become closed.

(2) The EMR calcined at 800℃ has the optimum pozzolanic activity, which is attributed to the decomposition of dihydrate gypsum and the formation of activated calcium, silicon and aluminum oxide. At 200 °C, calcination increased the pozzolanic activity of EMR due to the dihydrate gypsum dehydrated into β-type hemihydrate gypsum. Above 800 °C, the type II anhydrous gypsum weakens and transforms into type I anhydrous gypsum, which is related to the intercalation of fused quartz phases in EMR. The pozzolanic activity of EMR calcined at 1000°C was reduced due to the recrystallization of amorphous minerals and the formation of stable Mn-spinel (Mn_3O_4) and Mn-hercynite ($MnFe_2O_4$).

(3) A large amount of sulfate ions dissolved in the slurry reacts with calcium and aluminum phase to form hydration products, which adsorbs on the surface of the cement particles. It retards the cement hydration and inhibits the growth of crystals. The pore volume of EMR-blended mortar increases as the addition of EMR, which can be explained by the loose porous properties of EMR. However, the pores volume in the EMR-blended mortar gradually decreased due to the filling effect of the hydration products caused by the increasing pozzolanic activity of EMR.

(4) After calcinating at 200 ℃, the leaching of Mn^{2+} and NH_4^+-N did not decrease significantly but increase due to the water loss. The Mn^{2+} and NH_4^+-N fully below the national standards at calcination above 800°C (GB5085.3-1996; GB5085.3-2007). As the continued cement hydration promotes the

solidification of Mn^{2+} and the release of NH_4^+-N, all the specimens meet the standard limits after 28-d. The leaching of Mn^{2+} and NH_4^+-N of mortar formed by EMR calcined at temperatures above 800 °C for 3 d, 28 d and 90 d were all in accordance with the standard limits (GB5085.3-1996).

(5) The leaching tests results indicated that the leaching concentration of heavy metals decreased with increasing calcination temperature. It is because the glassy and crystalline products produced after calcination can incorporate metal ions into the amorphous network and crystal structure, leading to the immobilization of heavy metals. In EMR-blended mortar, heavy metal may be embedded in the hydration products or form precipitates with other ions. In addition, the dense structure of the mortar prevents the leaching behavior of heavy metal.

All heavy metals are fixed in the cement and calcination process, ensuring the cleaner utilization of EMR in building materials. Further studies on the effect of EMR on the C-S-H composition and structure of concrete, the effect of EMR on other components of concrete, the improvement of EMR reactivity, and the long-term durability of EMR-infused concrete are recommended.

Conflicts of interest

The authors declare no competing financial interests.

Acknowledgements

The authors appreciate the financial support from Hunan Province Key Field R&D Program (Grant No.2020wk2005), and the Postgraduate Scholarship, Central South University, Changsha, China.

CRediT author statement

Fan Wang: Conceptualization**,** Data curation, Writing-Original draft, and Writing-review & editing;

Guangcheng Long: Funding acquisition, Project administration, and Validation; **Min Bai:** Writing-review & editing, Investigation and Validation; **Jilin Wang:** Investigation and Validation; **JohnL Zhou:** Formal analysis, Methodology and Conceptualization, Writing-review & editing; **Xiang Zhou:** Formal analysis.

References

ASTM C618-17A, Standard specification for coal fly ash and raw or calcined natural pozzolan for use in concrete, ASTM International, West Conshohocken, PA, 2019, www.astm.org doi.org/ 10.1520/C0618-17A

Bal, B., Ghosh, S., Das, A. P., 2018. Microbial recovery and recycling of manganese waste and their future application: a review. Geomicrobiol J. 36, 85-96. doi.org/10.1080/01490451.2018.1497731

CEN-CENELEC, EN 196-5:2011. Methods of Testing Cement – Part 5: Pozzolanicity Test for Pozzolanic Cement, CEN-CENELEC, Brussels, Belgium, 2011.

Chen, H., Long, Q., Zhang, Y., Wang, S., Deng, F., 2020. A novel method for the stabilization of soluble contaminants in electrolytic manganese residue: Using low-cost phosphogypsum leachate and magnesia/calcium oxide. Ecotoxicol Environ Saf. 194, 110384. doi.org/10.1016/j.ecoenv.2020.110384

Crumbie, A., Walenta, G., Füllmann, T., 2006. Where is the iron? Clinker microanalysis with XRD Rietveld, optical microscopy/point counting, Bogue and SEM-EDS techniques. Cement Concrete Res. 36(8), 1542-1547. doi.org/10.1016/j.cemconres.2006.05.031

Donatello, S., Tyrer, M., Cheeseman, C. R., 2010. Comparison of test methods to assess pozzolanic activity. Cement Concrete Comp. 32, 121-127. doi.org/10.1016/j.cemconcomp.2009.10.008

Duan, N., Fan, W., Changbo, Z., Chunlei, Z., Hongbing, Y., 2010. Analysis of pollution materials generated from electrolytic manganese industries in China. Resour Conserv Recy. 54, 506-511. doi.org/10.1016/j.resconrec.2009.10.007

Duan, N., Dan, Z., Wang, F., Pan, C., Zhou, C., Jiang, L., 2011. Electrolytic manganese metal industry experience based China's new model for cleaner production promotion. J Clean Prod. 19, 2082-2087. doi.org/10.1016/j.jclepro.2011.06.024

Han, F., Wu, L., 2019. Resource utilization of electrolytic manganese residues, in: Industrial solid waste recycling in western China, 127-164. doi.org/10.1007/978-981-13-8086-0_3

Han, L., Wang, J., Liu, Z., Zhang, Y., Jin, Y., Li, J., Wang, D., 2020. Synthesis of fly ash-based self-supported zeolites foam geopolymer via saturated steam treatment. J Hazard Mater. 393, 122468. doi.org/10.1016/j.jhazmat.2020.122468

Han, Y., Cui, X., Lv, X., Wang, K., 2018. Preparation and characterization of geopolymers based on a phosphoric-acid-activated electrolytic manganese dioxide residue. J Clean Prod. 205, 488-498. doi.org/10.1016/j.jclepro.2018.09.141

Hardjito, D., Antoni, Wibowo, G. M., Christianto, D., 2012. Pozzolanic activity assessment of LUSI (LUmpur SIdoarjo) mud in semi high volume pozzolanic mortar. Materials. 5, 1654-1660. doi.org/10.3390/ma5091654

He, D., Shu, J., Wang, R., Chen, M., Wang, R., Gao, Y., Liu, R., Liu, Z., Xu, Z., Tan, D., Gu, H., Wang, N., 2021a. A critical review on approaches for electrolytic manganese residue treatment and disposal technology: Reduction, pretreatment, and reuse. J Hazard Mater. 418, 126235. doi.org/10.1016/j.jhazmat.2021.126235

He, P., Zhu, J., Chen, Y., Chen, F., Zhu, J., Liu, M., Zhang, K., Gan, M., 2021b. Pyrite-activated persulfate for simultaneous 2,4-DCP oxidation and Cr(VI) reduction. Chem. Eng. J. 406, 126758. doi.org/10.1016/j.cej.2020.126758

He, S., Jiang, D., Hong, M., Liu, Z., 2021c. Hazard-free treatment and resource utilisation of electrolytic manganese residue: A review. J Clean Prod. 306, 127224. doi.org/10.1016/j.jclepro.2021.127224

He, S., Wilson, B. P., Lundstrom, M., Liu, Z., 2021d. Hazard-free treatment of electrolytic manganese residue and recovery of manganese using low temperature roasting-water washing process. J Hazard Mater. 402, 123561.

doi.org/10.1016/j.jhazmat.2020.123561

Hou, P. k., Qian, J. s., Wang, Z., Deng, C., 2012. Production of quasi-sulfoaluminate cementitious materials with electrolytic manganese residue. Cement Concrete Comp. 34, 248-254. doi.org/10.1016/j.cemconcomp.2011.10.003

Lan, J., Dong, Y., Sun, Y., Fen, L., Zhou, M., Hou, H., Du, D., 2021a. A novel method for solidification/stabilization of Cd(II), Hg(II), Cu(II), and Zn(II) by activated electrolytic manganese slag. J Hazard Mater. 409, 124933. doi.org/10.1016/j.jhazmat.2020.124933

Lan, J., Dong, Y., Xiang, Y., Zhang, S., Mei, T., Hou, H., 2021b. Selective recovery of manganese from electrolytic manganese residue by using water as extractant under mechanochemical ball grinding: Mechanism and kinetics. J Hazard Mater. 415, 125556. doi.org/10.1016/j.jhazmat.2021.125556

Lan, J., Sun, Y., Chen, X., Zhan, W., Du, Y., Zhang, T. C., Ye, H., Du, D., Hou, H., 2021c. Bio-leaching of manganese from electrolytic manganese slag by Microbacterium trichothecenolyticum Y1: Mechanism and characteristics of microbial metabolites. Bioresour Technol. 319, 124056. doi.org/10.1016/j.biortech.2020.124056

Lan, J., Sun, Y., Tian, H., Zhan, W., Du, Y., Ye, H., Du, D., Zhang, T. C., Hou, H., 2021d. Electrolytic manganese residue-based cement for manganese ore pit backfilling: Performance and mechanism. J Hazard Mater. 411, 124941. doi.org/10.1016/j.jhazmat.2020.124941

Li, J., Du, D., Peng, Q., Wu, C., Lv, K., Ye, H., Chen, S., Zhan, W., 2018. Activation of silicon in the electrolytic manganese residue by mechanical grinding-roasting. J Clean Prod. 192, 347-353. doi.org/10.1016/j.jclepro.2018.04.184

Li, Q., Liu, Q., Peng, B., Chai, L., Liu, H., 2016. Self-cleaning performance of TiO_2-coating cement materials prepared based on solidification/stabilization of electrolytic manganese residue. Cons Build Mater. 106, 236-242. doi.org/10.1016/j.conbuildmat.2015.12.088

Li, J., Lv, Y., Jiao, X., Sun, P., Li, J., Wuri, L., Zhang, T. C., 2020. Electrolytic manganese residue based autoclaved bricks with $Ca(OH)_2$ and thermal-mechanical activated K-feldspar additions. Cons Build Mater. doi.org/230.10.1016/j.conbuildmat.2019.116848

Liu, Y., Lei, S., Lin, M., Li, Y., Ye, Z., Fan, Y., 2017. Assessment of pozzolanic activity of calcined coal-series kaolin. Appl Clay Sci 143, 159-167. doi.org/10.1016/j.clay.2017.03.038

Ma, M., Du, Y., Bao, S., Li, J., Wei, H., Lv, Y., Song, X., Zhang, T., Du, D., 2020. Removal of cadmium and lead from aqueous solutions by thermal activated electrolytic manganese residues. Sci Total Environ. 748, 141490. doi.org/10.1016/j.scitotenv.2020.141490

Pourkhorshidi, A.R., Najimi, M., Parhizkar, T., Jafarpour, F., Hillemeier, B., 2010, Applicability of the standard specifications of ASTM C618 for evaluation of natural pozzolans. Cement Concrete Comp. 32, 794-800. doi.org/10.1016/j.cemconcomp.2010.08.007

Shu, J., Chen, M., Wu, H., Li, B., Wang, B., Li, B., Liu, R., Liu, Z., 2019a. An innovative method for synergistic stabilization/solidification of Mn^{2+}, NH_4^+-N, PO_4^{3-} and F^- in electrolytic manganese residue and phosphogypsum. J Hazard Mater. 376, 212-222. doi.org/10.1016/j.jhazmat.2019.05.017

Shu, J., Li, B., Chen, M., Sun, D., Wei, L., Wang, Y., Wang, J., 2020. An innovative method for manganese (Mn^{2+}) and ammonia nitrogen (NH_4^+-N) stabilization/solidification in electrolytic manganese residue by basic burning raw material. Chemosphere. 253, 126896. doi.org/10.1016/j.chemosphere.2020.126896

Shu, J., Liu, R., Liu, Z., Chen, H., Du, J., Tao, C., 2016. Solidification/stabilization of electrolytic manganese residue using phosphate resource and low-grade MgO/CaO. J Hazard Mater. 317, 267-274. doi.org/10.1016/j.jhazmat.2016.05.076

Shu, J., Wu, H., Chen, M., Peng, H., Li, B., Liu, R., Liu, Z., Wang, B., Huang, T., Hu, Z., 2019b. Fractional removal of manganese and ammonia nitrogen from electrolytic metal manganese residue leachate using carbonate and struvite precipitation. Water Res. 153, 229-238. doi.org/10.1016/j.watres.2018.12.044

Shu, J., Wu, H., Liu, R., Liu, Z., Li, B., Chen, M., Tao, C., 2018. Simultaneous stabilization/solidification of Mn^{2+} and NH_4^+-N from electrolytic manganese residue using MgO and different phosphate resource. Ecotoxicol Environ Saf. 148, 220-227. doi.org/10.1016/j.ecoenv.2017.10.027

Standards, 1996. The State Bureau of Environmental Protection and The State Bureau of Technical Supervision. Identification standard for hazardous wastes-Identification for extraction procedure toxicity. The State Standard of the People's Republic of China, GB 5085.3-1996, Standards Press of China, Beijing. [in Chinese]

Standards, 2007. The State Bureau of Environmental Protection and The State Bureau of Technical Supervision. Identification standard for hazardous wastes-Identification for extraction procedure toxicity. The State Standard of the People's Republic of China, GB 5085.3-2007, Standards Press of China, Beijing. [in Chinese]

Standards, 2000. The State General Administration of the People's Republic of China for Quality Supervision and Inspection and Quarantine. Methods for chemical analysis of aluminate cement. The State Standard of the People's Republic of China, GB/T 205-2000, Standards Press of China, Beijing. [in Chinese]

Standards, 2005. General Administration of the People's Republic of China for Quality Supervision and Inspection and Quarantine. Pozzolanic materials used for cement production. The State Standard of the People's Republic of China, GB/T 2847-2005, Standards Press of China, Beijing. [in Chinese]

Standards, 2007. The State Environmental Protection Administration. Solid waste-Extraction procedure for leaching toxicity-Acetic acid buffer solution method. The People's Republic of China Environmental Protection Industry Standards, HJ/T 300-2007, China Environmental Science Press, Beijing. [in Chinese]

Standards, 2009a. The Ministry of Environmental Protection. Water quality-Determination of cyanide-Volumetric and spectrophotometry method. The People's Republic of China Environmental Protection Industry Standards, HJ 484-2009, China Environmental Science Press, Beijing. [in Chinese]

Standards, 2009b. The Ministry of Environmental Protection. Water quality-Determination of ammonium nitrogen-Nessler's reagent spectrophotometry. The People's Republic of China Environmental Protection Industry Standards, HJ 535-2009, China Environmental Science Press, Beijing. [in Chinese]

Standards, 2010. The Ministry of Environmental Protection. Solid waste-Extraction procedure for leaching toxicity-Horizontal vibration method. The State Standard of the People's Republic of China, HJ-557-2010, China Environmental Science Press, Beijing. [in Chinese]

Standards, 2017. The Ministry of Environmental Protection. Water quality-Determination of chromium (VI) - Flow injection analysis (FIA) and diphenylcarbazide spectrometric method. The People's Republic of China Environmental Protection Industry Standards, HJ 908-2017, China Environmental Science Press, Beijing. [in Chinese]

Standards, 2017. General Administration of the People's Republic of China for Quality Supervision and Inspection and Quarantine. Fly ash used for cement and concrete. The State Standard of the People's Republic of China, GB/T 1596-2017, Standards Press of China, Beijing. [in Chinese]

Sun, D., Yang, L., Liu, N., Jiang, W., Jiang, X., Li, J., Yang, Z., Song, Z., 2020. Sulfur resource recovery based on electrolytic manganese residue calcination and manganese oxide ore desulfurization for the clean production of electrolytic manganese. Chinese J Chem Eng. 28, 864-870. doi.org/10.1016/j.cjche.2019.11.013

Tironi, A., Trezza, M.A., Scian, A.N., Irassar, E.F., 2013. Assessment of pozzolanic activity of different calcined clays. Cement Concrete Comp. 37, 319-327. doi.org/10.1016/j.cemconcomp.2013.01.002

Wang, D., Wang, Q., Xue, J., 2020. Reuse of hazardous electrolytic manganese residue: Detailed leaching characterization and novel application as a cementitious material. Resour Conserv Recy. 154, 104645. doi.org/10.1016/j.resconrec.2019.104645

Wang, J., Peng, B., Chai, L., Zhang, Q., Liu, Q., 2013. Preparation of electrolytic manganese residue–ground granulated blast furnace slag cement. Powder Technol. 241, 12-18. doi.org/10.1016/j.powtec.2013.03.003

Wang, N., Fang, Z., Peng, S., Cheng, D., Du, B., Zhou, C., 2016. Recovery of soluble manganese from electrolyte manganese residue using a combination of ammonia and CO_2. Hydrometallurgy. 164, 288-294. doi.org/10.1016/j.hydromet.2016.06.019

Wang, Y., Gao, S., Liu, X., Tang, B., Mukiza, E., Zhang, N., 2019. Preparation of non-sintered permeable bricks using electrolytic manganese residue: Environmental and NH_3-N recovery benefits. J Hazard Mater. 378, 120768. doi.org/10.1016/j.jhazmat.2019.120768

Wu, F., Li, X., Zhong, H., Wang, S., 2016. Utilization of electrolytic manganese residues in production of porous ceramics. Int. J. Appl. Ceram. Technol. 13(3), 511-521. doi.org/10.1111/ijac.12502

Xie, H., Li, S., Guo, Z., Xu, Z., 2021. Extraction of lead from electrolytic manganese anode mud by microwave coupled ultrasound technology. J Hazard Mater. 407, 124622. doi.org/10.1016/j.jhazmat.2020.124622

Xu, F., Jiang, L., Dan, Z., Gao, X., Duan, N., Han, G., 2014. Water balance analysis and wastewater recycling investigation in electrolytic manganese industry of China - A case study. Hydrometallurgy 149, 12-22. doi.org/10.1016/j.hydromet.2014.05.002

Xu, L. J., Wang, X. M., Chen, H. C., Liu, C. L., 2011. Mn forms and environmental impact of electrolytic manganese residue. Adv Mater Res. 183-185, 570-574. doi.org/10.4028/www.scientific.net/AMR.183-185.570

Xu, Y., Liu, X., Zhang, Y., Tang, B., Mukiza, E., 2019. Investigation on sulfate activation of electrolytic manganese residue on early activity of blast furnace slag in cement-based cementitious material. Constr Build Mater. 229, 116831. doi.org/10.1016/j.conbuildmat.2019.116831

Yang, C., Lv, X., Tian, X., Wang, Y., Komarneni, S., 2014. An investigation on the use of electrolytic manganese residue as filler in sulfur concrete. Constr Build Mater. 73, 305-310. doi.org/10.1016/j.conbuildmat.2014.09.046

Zhang, R., Ma, X., Shen, X., Zhai, Y., Zhang, T., Ji, C., Hong, J., 2020a. Life cycle assessment of electrolytic manganese metal production. J Clean Prod. 253, 119951. doi.org/10.1016/j.jclepro.2019.119951

Zhang, Y., Liu, X., Xu, Y., Tang, B., Wang, Y., 2020b. Preparation of road base material by utilizing electrolytic manganese residue based on Si-Al structure: Mechanical properties and Mn^{2+} stabilization/solidification characterization. J Hazard Mater. 390, 122188. doi.org/10.1016/j.jhazmat.2020.122188

Zhang, Y., Liu, X., Xu, Y., Tang, B., Wang, Y., Mukiza, E., 2019a. Synergic effects of electrolytic manganese residue-red mud-carbide slag on the road base strength and durability properties. Constr Build Mater. 220, 364-374. doi.org/10.1016/j.conbuildmat.2019.06.009

Zhang, Y., Liu, X., Xu, Y., Tang, B., Wang, Y., Mukiza, E., 2019b. Preparation and characterization of cement treated road base material utilizing electrolytic manganese residue. J Clean Prod. 232, 980-992. doi.org/10.1016/j.jclepro.2019.05.352

Zhou, C., Du, B., Wang, N., Chen, Z., 2014. Preparation and strength property of autoclaved bricks from electrolytic manganese residue. J Clean Prod. 84, 707-714. doi.org/10.1016/j.jclepro.2014.01.052

Zhou, Y., 2021. Reusing electrolytic manganese residue as an activator: The effect of calcination on its mineralogy and activity. Constr Build Mater. 294, 123533. doi.org/10.1016/j.conbuildmat.2021.123533

Application of electrolytic manganese residues in cement products through pozzolanic activity motivation and calcination

Fan Wang[1], Guangcheng Long[2,1], Min Bai[1], Jilin Wang[1], John L. Zhou[1,2], Xiang Zhou[1]

[1] School of Civil Engineering, Central South University, 68 South Shaoshan Road, Changsha, Hunan 410075, China

[2] Centre for Green Technology, School of Civil and Environmental Engineering, University of Technology Sydney, Sydney, NSW 2007, Australia

Supporting Information

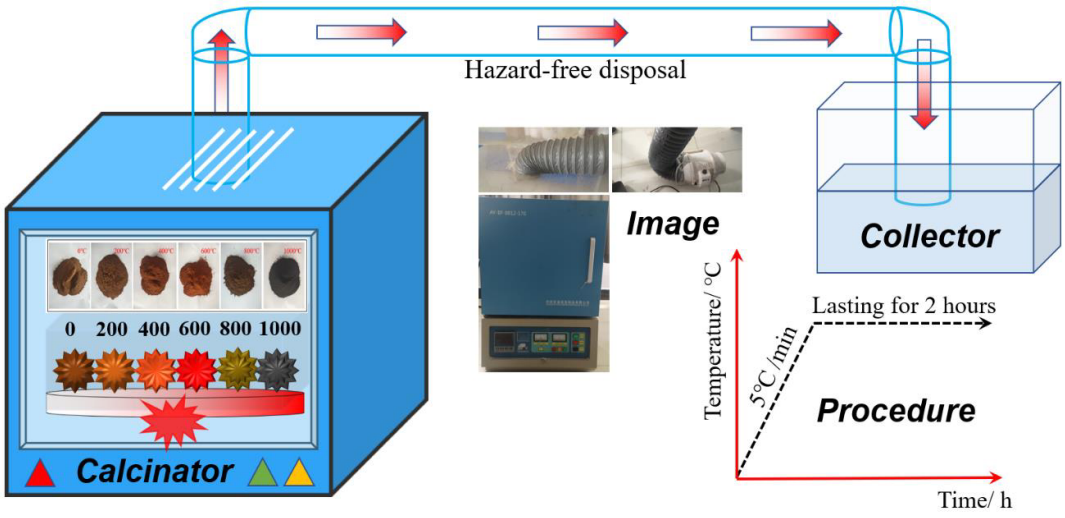

Fig. S1. Calcination, collection and pretreatment system.

[2] Corresponding author: longguangcheng@csu.edu.cn (G. Long)

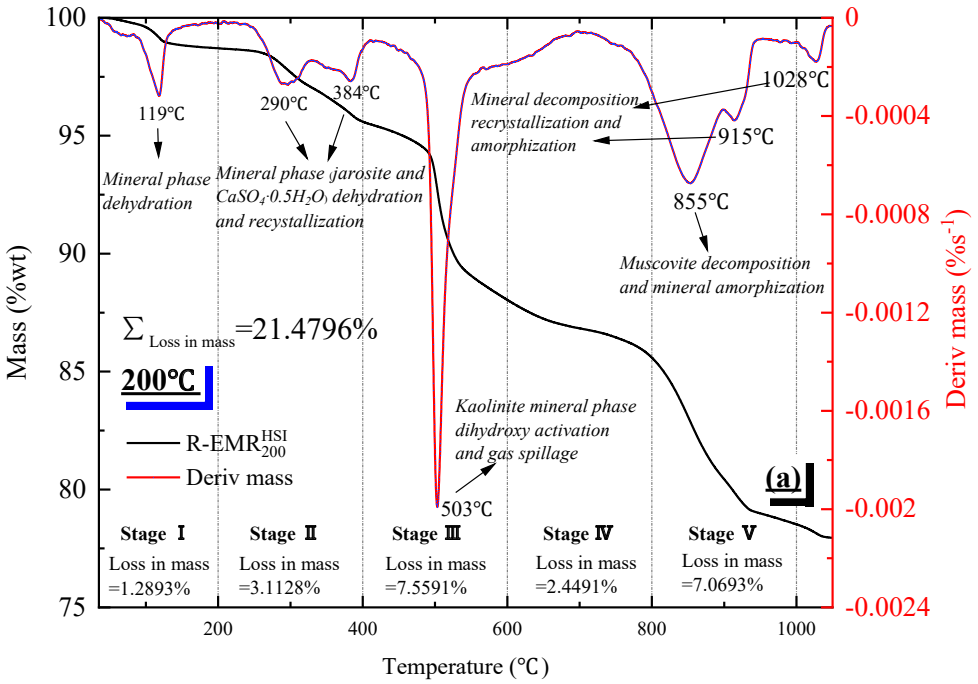
100
95
90
85
80
75
Mass (%wt)
0
-0.0004
-0.0008
-0.0012
-0.0016
-0.002
-0.0024
Deriv mass (%s-1)
200
400
600
800
1000
Temperature (℃)
119℃
290℃
384℃
503℃
855℃
915℃
1028℃
Mineral phase dehydration
Mineral phase (jarosite and CaSO4·0.5H2O) dehydration and recystallization
Mineral decomposition recrystallization and amorphization
Muscovite decomposition and mineral amorphization
Kaolinite mineral phase dihydroxy activation and gas spillage
∑Loss in mass=21.4796%
200℃
R-EMR200HSI
Deriv mass
(a)
Stage Ⅰ
Loss in mass =1.2893%
Stage Ⅱ
Loss in mass =3.1128%
Stage Ⅲ
Loss in mass =7.5591%
Stage Ⅳ
Loss in mass =2.4491%
Stage Ⅴ
Loss in mass =7.0693%

849

850

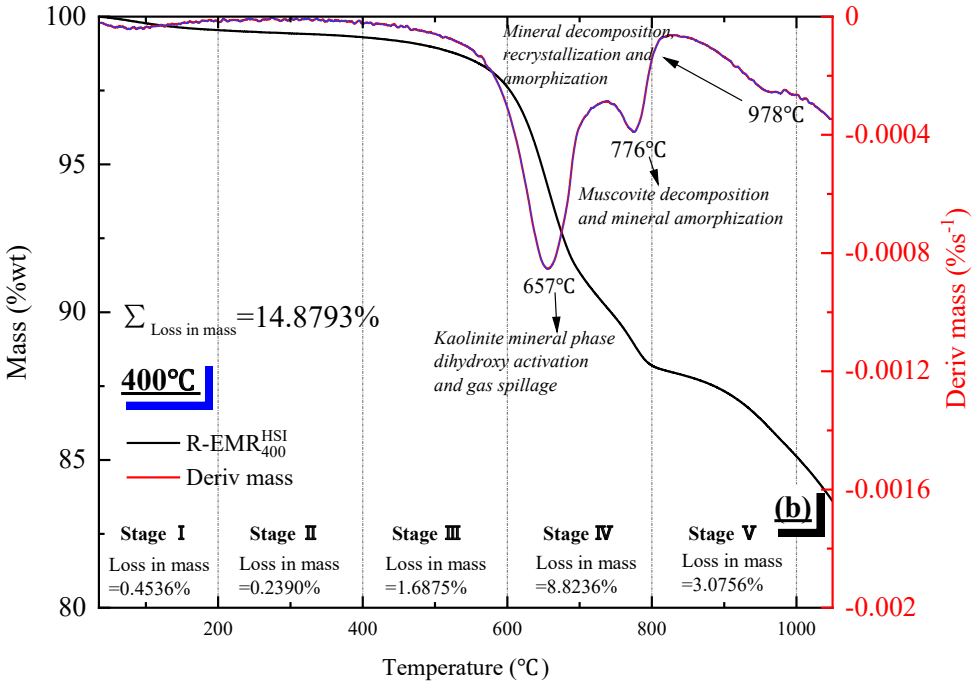
100
95
90
85
80
Mass (%wt)
0
-0.0004
-0.0008
-0.0012
-0.0016
-0.002
Deriv mass (%s-1)
200
400
600
800
1000
Temperature (℃)
657℃
776℃
978℃
Mineral decomposition recrystallization and amorphization
Muscovite decomposition and mineral amorphization
Kaolinite mineral phase dihydroxy activation and gas spillage
∑Loss in mass=14.8793%
400℃
R-EMR400HSI
Deriv mass
(b)
Stage Ⅰ
Loss in mass =0.4536%
Stage Ⅱ
Loss in mass =0.2390%
Stage Ⅲ
Loss in mass =1.6875%
Stage Ⅳ
Loss in mass =8.8236%
Stage Ⅴ
Loss in mass =3.0756%

851

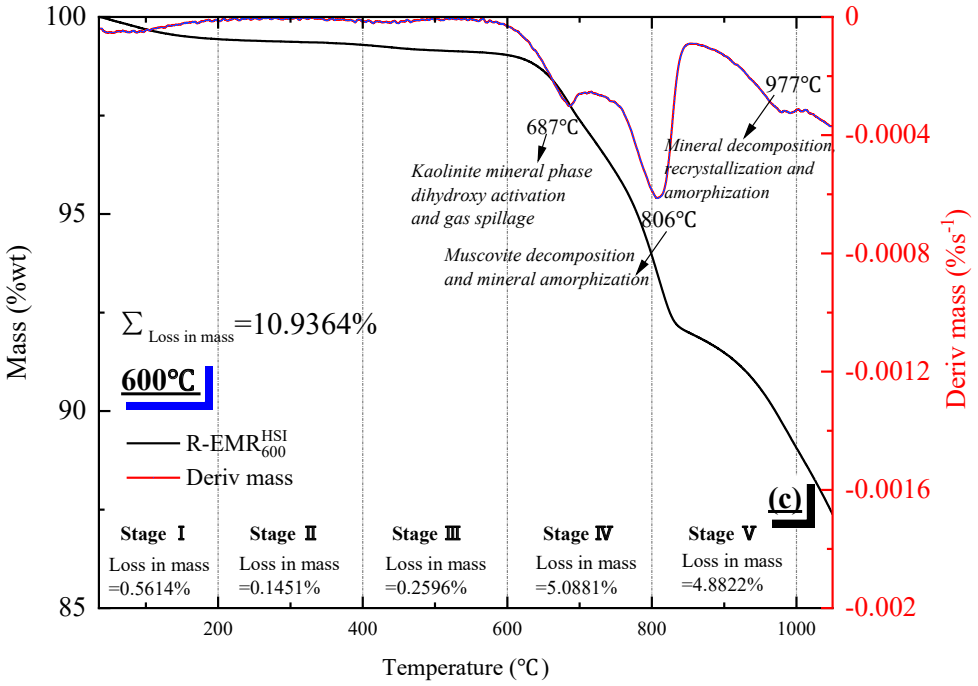
100
95
90
85
0
-0.0004
-0.0008
-0.0012
-0.0016
-0.002
200
400
600
800
1000
Mass (%wt)
Deriv mass (%s^{-1})
Temperature (℃)
687℃
977℃
806℃
Kaolinite mineral phase dihydroxy activation and gas spillage
Mineral decomposition, recrystallization and amorphization
Muscovite decomposition and mineral amorphization
$\sum_{\text{Loss in mass}}$=10.9364%
600℃
R-EMR$^{HSI}_{600}$
Deriv mass
(c)
Stage Ⅰ Loss in mass =0.5614%
Stage Ⅱ Loss in mass =0.1451%
Stage Ⅲ Loss in mass =0.2596%
Stage Ⅳ Loss in mass =5.0881%
Stage Ⅴ Loss in mass =4.8822%

852

853

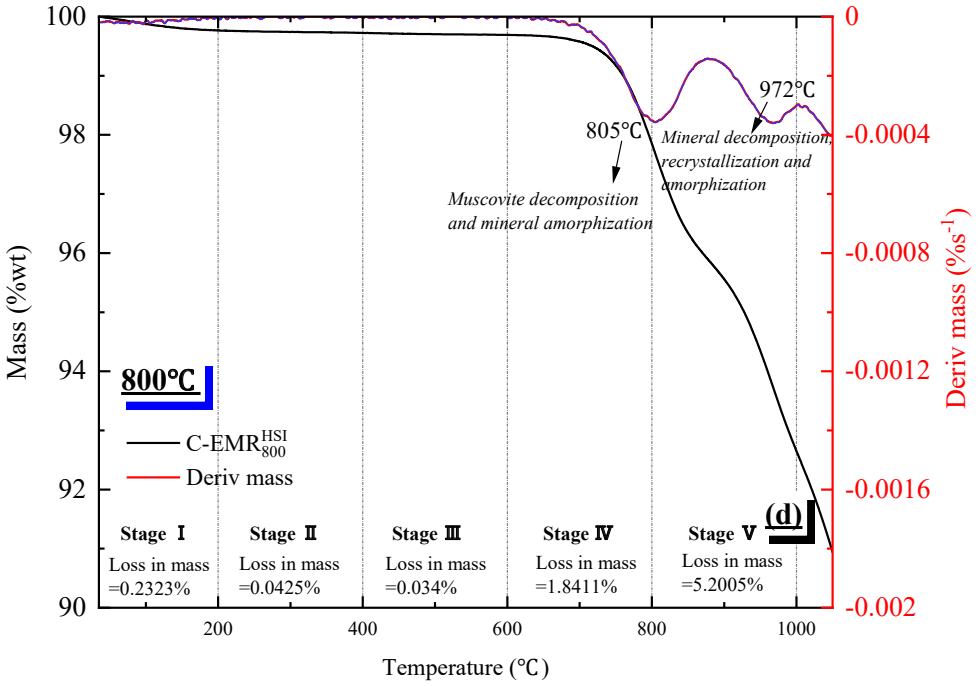
100
98
96
94
92
90
0
-0.0004
-0.0008
-0.0012
-0.0016
-0.002
200
400
600
800
1000
Mass (%wt)
Deriv mass (%s^{-1})
Temperature (℃)
805℃
972℃
Muscovite decomposition and mineral amorphization
Mineral decomposition, recrystallization and amorphization
800℃
C-EMR$^{HSI}_{800}$
Deriv mass
(d)
Stage Ⅰ Loss in mass =0.2323%
Stage Ⅱ Loss in mass =0.0425%
Stage Ⅲ Loss in mass =0.034%
Stage Ⅳ Loss in mass =1.8411%
Stage Ⅴ Loss in mass =5.2005%

854

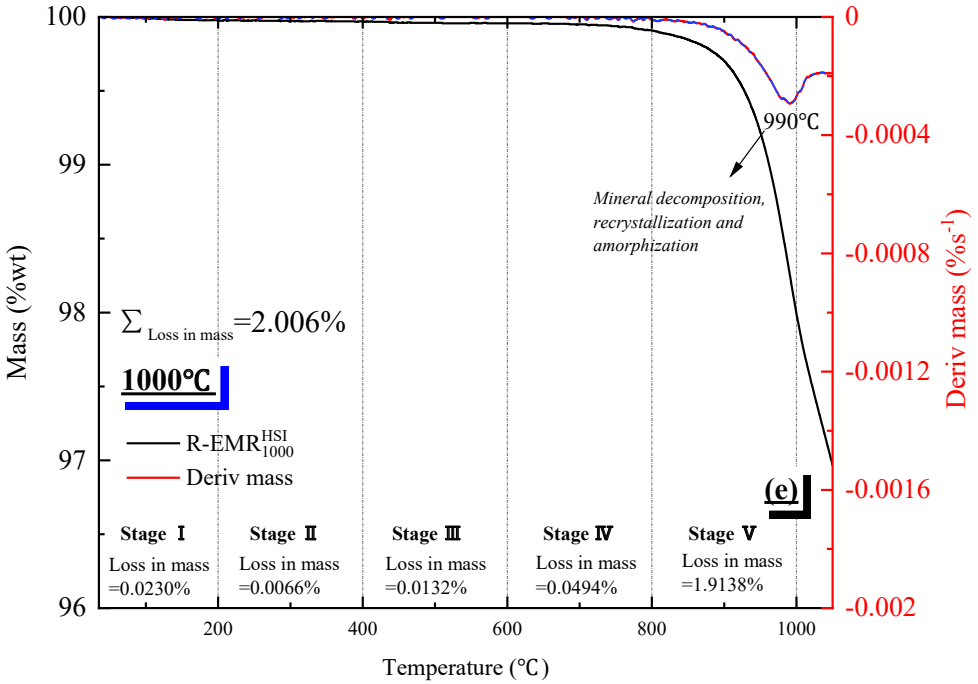

855

856 **Fig. S2.** TG-DTG results of the calcined samples after experiencing the setting calcination

857 temperature treatment (a) 200℃, (b) 400℃, (c) 600℃, (d) 800℃, and (e) 1000℃.

858

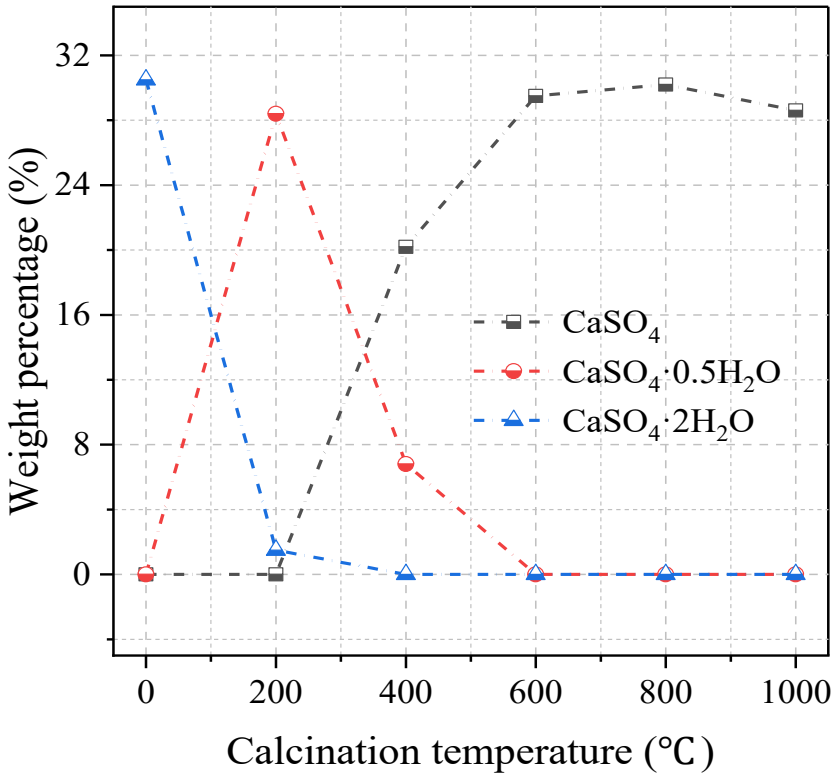

859

860 **Fig.S3.** Quantitative results of gypsum phases at different calcination temperatures

Table S1 Setting time and soundness of EMR-blended mortar

Sample	Cement	M-REMR^{HSI}	M-CEMR$^{HSI}_{200}$	M-CEMR$^{HSI}_{400}$	M-CEMR$^{HSI}_{600}$	M-CEMR$^{HSI}_{800}$	M-CEMR$^{HSI}_{1000}$
ST (min)	315	330	355	410	390	360	335
Soundness	Q	Q	Q	UQ	UQ	Q	Q

Note: ST stands for final setting time. Q and UQ present qualified and unqualified, respectively.